SEARCH FOR THE SIGNATURES OF MASS-EXCHANGE EPISODES IN MASSIVE BINARIES

Françoise Raucq

Dissertation présentée en vue de l'obtention du grade de

Docteur en Sciences

Supervisor: Pr. Gregor Rauw

Co-supervisor: Dr. Laurent Mahy

Astrophysics, Geophysics and Oceanography Department
Space sciences, Technologies and Astrophysics Research unit
University of Liège, Liège, Belgium

August 2017

Supervisors - Pr. Gregor Rauw
Dr. Laurent Mahy

Jury - Pr. Marc-Antoine Dupret as President
Pr. Gregor Rauw
Dr. Laurent Mahy
Dr. Ronny Blomme
Dr. Jean-Claude Bouret
Dr. Éric Gosset
Pr. Norbert Langer

Cover:
The emission nebula NGC 6188 and the young stellar open cluster NGC 6193, in the Ara OB1 association

Acknowledgments

Observing the sky is a passion of mine for as long as I can remember, and I have always dreamed, as a child, to become an astrophysicist. I would like to thank my supervisor, Pr. Gregor Rauw, for having given to me the opportunity to accomplish this dream through these four years of PhD thesis in the "Groupe d'AstroPhysique des Hautes Énergies". I also thank him for his help all over these years, for his great support and his huge contribution to my papers and this thesis manuscript. I thank my co-supervisor, Dr. Laurent Mahy, for his availability for my (numerous) questions and his precious help, in particular concerning the CMFGEN code. I also thank Dr. Fabrice Martins and Dr. Anthony Hervé for their help in the very first steps of my work with this very complex code. I am also grateful to Éric Gosset for his contribution to my work on the very unusual object LSS 3074.

I thank Pr. Marc-Antoine Dupret for accepting to be President of the Jury, and Pr. Gregor Rauw, Dr. Laurent Mahy, Dr. Ronny Blomme, Dr. Jean-Claude Bouret, Dr. Éric Gosset and Pr. Norbert Langer for accepting to be members of the jury.

Special thanks to my colleagues and friends Enmanuelle, for her friendship and support all over our studies and as far as the other side of the world, and Judith and Clémentine, for the great moments spent around a well deserved cup of tea. I also thank my teammate in the GAPHE, Constantin, for being available for any (sometimes stupid) question at any time over this thesis work.

Finally, I am very gratefull to my mother, Claudine, and father, Philippe, for being there at any time, for rising me up and helping me to become who I am, and for encouraging me to follow my dreams, and even to plant the seeds of these dreams, through numerous nights observing the sky. Thank you also to my brothers, Simon and Pierre-Yves, and sister, Zoé, for listening to my stories, even when they did not understand half of what I said.

And last but not least, I would like to express my deep gratitude and all my love to my husband, Sylvain, who was there for me every single day, with a great patience, particularly in the most difficult moments of the past years.

Abstract

Massive stars are known for their crucial role in our Universe, through their extreme stellar parameters, leading to a strong impact on their environment. However, there remain numbers of unanswered questions concerning the exact processes of their formation, their stability or the processes driving their strong stellar winds. In the context of this thesis work, we adress one of the most interesting of their peculiarities: their tendency to be part of binary of higher multiplicity systems. Whilst this multiplicity does help to solve some open issues by allowing us to study some of the fundamental properties of the stars, such as their minimum masses and radii as well as their stellar luminosities, it can also lead to interactions between the components of a system, which affect the subsequent evolution of the stars and give rise to additional open questions on the processes in place in such systems. Among the possible interactions taking place within close binary systems is the possibility of a transfer of mass and kinetic momentum through a Roche lobe overflow. This process has a huge impact on the subsequent evolution of both components and many aspects of this phenomenon are not well understood yet.

The present work is devoted to the search for the signatures of such past mass-exchange episodes in a sample of four short-period massive multiple systems: HD 149404, LSS 3074, HD 17505 and HD 206267. We determined a new orbital solution for three of them. We then used phase-resolved spectroscopy to perform the spectral disentangling of the optical spectra of the components. The spectral disentangling is a mathematical tool which allows to separate the contributions of both components to the observed spectra of a system. We then analysed the reconstructed spectra with the CMFGEN atmosphere code to determine stellar parameters, such as the effective temperatures and surface gravities, and to constrain the surface chemical composition of each component.

The first two parts of this dissertation are dedicated to the scientific background and the description of the numerical tools and methods used in this work. The third part presents our studies of the selected massive systems. We confirmed that the hypothesis of a past Roche lobe overflow episode is most plausible to explain the observed properties of the components of HD 149404. Photometric data permitted us to confirm that LSS 3074 is in an overcontact configuration, and a combined analysis with spectroscopy showed that the system has lost a significant fraction of its mass to its surroundings. We proposed several possible evolutionary pathways involving a Roche lobe overflow process to explain the current parameters of its components. We found no evidence of past mass-transfer episodes in the spectra of HD 17505 and showed that the current properties of its components can be explained by single star evolutionary models including rotational mixing. We found clues of binary interactions in the spectra of HD 206267, but suggested that the system did not experience a complete Roche lobe overflow episode at this stage of its evolution.

Résumé

Les étoiles massives sont connues pour leur rôle fondamental dans l'Univers, au travers de leurs paramètres stellaires extrêmes, qui leur confèrent un très grand impact sur leur environnement. Il reste toutefois de nombreuses questions sans réponse quant aux processus exacts qui donnent lieu à leur formation, à leur stabilité ou encore aux processus liés à leurs vents stellaires forts. Dans le cadre de ce travail de thèse de doctorat, nous nous intéressons en particulier à l'une de leurs spécificités : leur tendance à faire partie de systèmes binaires ou de plus grande multiplicité. Si cette multiplicité est très utile car elle permet d'étudier certaines propriétés fondamentales des étoiles, telles que les masses minimales, les rayons et les luminosités, elle peut aussi mener à des interactions entre les composantes d'un système, ce qui va affecter l'évolution ultérieure des étoiles et mener à des interrogations supplémentaires sur les processus présents dans de tels systèmes. Parmi les interactions possibles dans les systèmes binaires massifs à courte période, nous nous intéressons à la possibilité d'un transfert de matière et de moment cinétique au travers d'un dépassement de lobe de Roche. Ce processus a un impact très important sur l'évolution ultérieure de chacune des composantes et beaucoup d'aspects de ce phénomène ne sont pas encore très bien compris à l'heure actuelle.

Le présent travail est basé sur la recherche de la signature spectrale d'un tel épisode d'échange de matière dans un échantillon de quatre systèmes multiples massifs à courte période : HD 149404, LSS 3074, HD 17505 et HD 206267. Nous avons déterminé une nouvelle solution orbitale pour trois de ces systèmes. Nous avons ensuite exploité des données spectroscopiques dans le domaine visible et utilisé un outil mathématique construit pour séparer la contribution de chaque composante d'un système aux spectres observés de celui-ci. Nous avons ensuite analysé les spectres ainsi reconstruits au moyen du code de modélisation atmosphérique CMFGEN, afin de déterminer les paramètres stellaires de chacune des composantes, tels que les températures effectives et gravités de surface, ainsi que la composition chimique de surface de ces étoiles.

Les deux premiers chapitres de cette dissertation sont dédiés à l'état de

l'art et à une description des outils et méthodes mathématiques que nous avons exploités au troisième chapitre de ce travail, qui décrit notre étude des systèmes sélectionnés. Nous avons ainsi confirmé que l'hypothèse d'un épisode de dépassement de lobe de Roche antérieur aux observations est la plus plausible pour expliquer les propriétés observées des composantes de HD 149404. Dans le cas de LSS 3074, des données photométriques nous ont permis de confirmer que ce système est dans une configuration dite d'"over-contact", et une analyse combinée des données photométriques et spectroscopiques a montré que le système a transféré une partie significative de sa masse au milieu environnant. Nous avons proposé plusieurs scénarios d'évolution incluant un processus de dépassement de lobe de Roche pour expliquer les paramètres actuels de ses composantes. Nous n'avons en revanche trouvé aucune preuve d'épisode de transfert de matière antérieur dans les spectres de HD 17505 et nous avons montré que les propriétés observées de ses composantes peuvent être expliquées par les modèles d'évolution d'étoiles isolées incluant un mélange rotationnel. Finalement, nous avont trouvé des indices d'interaction binaires dans les spectres de HD 206267, mais avons suggéré que ce système n'a pas connu de dépassement de lobe de Roche complet dans son état actuel d'évolution.

Contents

Chapter 1

Introduction

Despite their rarity, massive stars (stars with masses $\geq 8 - 10$ M$_\odot$), and their evolved descendants the Wolf-Rayet (WR) stars, are a key ingredient in our Universe. Indeed, they display extreme parameters, among which their high effective temperatures (T$_{eff}$ $\geq$ 20 000K) and high luminosities (10^5-10^6 L$_\odot$). These two properties make them the main source of UV and ionizing radiation of the Universe. Moreover, these properties also result into huge radiation-driven stellar winds with large terminal velocities (1000-3000 km s^{-1}) and mass-loss rates (10^{-7}-10^{-5} M$_\odot$ yr^{-1}). These winds have a huge influence onto the environment of the stars, by compressing the surrounding gas and thus triggering the formation of a new generation of stars. Moreover, massive stars have a relatively short lifetime (a few million years), and they have another huge impact on their surroundings upon their death as supernovae. The mechanical powers in galaxies due to supernova explosions and to the winds of O and WR stars are of comparable importance. Besides, both their strong winds and their impressive deaths play a key role in the chemical evolution of their host galaxies, through an enrichment of the interstellar medium (ISM) in heavy elements resulting from nucleosynthesis, mostly produced during the last stages of the evolution of the stars.

This thesis work is mainly concerned with another aspect of massive stars: their tendency to be part of binary systems. Recent studies have suggested that most of the massive stars are part of binary or higher multiplicity systems (Sana et al. 2012). This multiplicity allows us to observationally determine some fundamental parameters of the components, such as the stellar masses, radii and luminosities, but it can also lead to interactions between these components, provided the orbital separation is small. These interactions can highly complexify the subsequent evolution of the stars, in a way that is not completely understood yet. We can observe the results of the binary interactions in various features within the spectra of the stars (chemical abundances, rotational velocities, ...), which will serve as diagnostics of past or present interaction processes.

Despite considerable progress in our understanding of the physics of massive stars during the last decades, many questions still remain unanswered, both regarding their evolution and their fundamental properties. The particular case of massive binaries is even more complicated, due to the complexity of the interactions that the components will undergo. In-depth studies of these interactions are thus very important to improve our general understanding of massive stars and their evolution.

In this introductory chapter, we will give an overview of the life of massive stars and the different categories of binary systems we encountered during this thesis work. We will also introduce a few possible interactions within these systems. Finally, we specifically introduce the present work on observational signatures of the particular case of mass-exchange episodes in a sample of massive binaries.

1.1 Structure and evolution of massive stars

It is nowadays admitted that low-mass star formation begins when dense parts of molecular clouds within the ISM collapse because of a sudden gravitational instability. This instability can be either spontaneous, or induced by external forces, such as a nearby supernova or the strong stellar winds of one or several massive stars.

However, although considerable theoretical progresses have been made during the last few years in our understanding of massive stars formation, this topic remains one of the nowadays most crucial astrophysical issues (Bonnell & Smith 2011, Bonnell et al. 2011). One of the main reasons behind these difficulties to understand the earliest stages of their formation is that few massive stars have been seen forming, because of high dust extinction of their light during the earliest phases of their life, the short duration of this evolutionary stage and the rarity of these objects. However, it is broadly admitted that massive stars form within a few 10^5 years.

In order to form massive stars, the initial giant molecular cloud must have a H_2 column density of 10^{23} to 10^{24} cm^{-2} (Zinnecker & Yorke 2007). When such a cloud collapses, it can either produce an OB cluster or an OB association of massive stars. A cluster is a dense population of stars gravitationally bound to each other (e.g. NGC 6231, see Sana et al. 2006). An association is a population of stars spread out over the extent of the initial molecular cloud and not densely packed, with distances between the stars of several parsecs[1] (e.g. Ara OB1 association, see Herbst & Havlen 1977). Because of their short lifetime, massive stars are expected to be observed at or near to their birth location, and most of them are indeed found in young open clusters or OB associations. However, it is also possible to observe O stars outside these regions. Most of these outsiders are thought to be runaways, ejected from their birth cluster or association because of close encounters and tidal interactions or after a supernova kick in a binary system. Only 4% of Population I O-type stars cannot be linked to clusters and associations (de Wit et al. 2005), and may have formed in isolation. There is thus a small percentage of massive stars that may form isolated, but most of these objects are found relatively close to each other, which complicates the understanding of their formation process because of mutual interactions.

Protostars are gaseous objects in hydrostatic equilibrium, that increase their mass by accretion of neighboring gas. For low-mass stars, the material is accreted through a disk and the final mass is reached when the accretion stops. The protostars then continue their collapse and spend a long time in a contracting phase called the pre main-sequence phase. When the temperature in the core is sufficiently high, nuclear reactions set in, burning the hydrogen into helium in the core, and the outward pressure of the resulting radiation stops the collapse. The stars then enter their main-sequence phase, where they will spend the most significant part of their life.

For high-mass stars, the H-burning in the core ignites before these stars have reached their final mass, and the accretion of material must then continue afterward. A problem arose in the past because the observed accretion rate for low-mass stars is too low to form stars of several tens of $M_\odot$ within a few 10^5 years, i.e. within less than a significant fraction of the main-sequence lifetime of massive stars. However, Norberg & Maeder (2000) discuss the possible existence of higher accretion rates: higher temperature and density conditions and turbulence of the gas in molecular clouds (Mckee & Tan 2003) that usually give birth to massive stars might result in much higher accretion rates than considered previously. A second problem arose because a relatively massive protostar would have a luminosity sufficient to generate a radiation pressure high enough to decrease significantly or even halt the accretion. Nevertheless, this barrier has been recently overcome by assuming an anisotropic radiation field. According to these new models, most massive stars can form via disk accretion because a massive accretion disk yields a strong aniso-

---

[1] 1 parsec = $3.08568025 \times 10^{13}$ km.

tropy in the radiation field, releasing most of the radiation pressure in a direction perpendicular to the disk accretion flow (Kuiper et al. 2011 and references therein). Once a nearly Keplerian disk has formed around a massive protostar, further accretion is only possible if some angular momentum is removed from the disk (through the formation of jets, outflows or disk winds) or efficiently transported to the outer disk radii. Kuiper et al. (2011) have shown that self-gravitating instabilities are a major driver of angular momentum transport to the outer disk radii via the development of gravitational torques.

A second formation scenario was also proposed in dense stellar environments, like the cores of clusters, where massive stars could form by coalescence of lower-mass protostars formed by the accretion scenario (Bonnell et al. 1998, Bonnell & Bate 2005). However, this scenario requires a relatively high stellar density and a relatively high number of merger events within a short time-scale. It can thus only occur in the most massive and densest clusters, thereby excluding it as the first cause of the massive star formation.

It is thus nowadays admitted that the formation of massive stars is most likely a scaled-up version of the formation of low-mass stars, with a higher accretion rate (Zinnecker & Yorke 2007). This theoretical picture is supported by a number of recent observations of circumstellar disks surrounding high-mass protostars (see e.g. Chini et al. 2011, Chen et al. 2013, Johnston et al. 2015).

For single stars up to solar masses, the combustion of H into He occurs via the proton-proton chain reaction (Bethe & Critchfield 1938). On the other hand, for heavier stars the CNO cycle dominates (Bethe 1939, Caughlan 1965; see Table 1.1). When the hydrogen is exhausted, this nuclear reaction stops. If the star is less massive than 40 $M_\odot$, the core then begins to contract, and the envelope expands. The star becomes a red giant, and starts burning H in a layer above the inert core of He. If the star is more massive, it will enter a Luminous Blue Variable (LBV) phase after the main sequence. During this relatively short phase ($\sim 10^4$ years), the mass-loss rate of the star will be extremely high, of the order of 10^{-3} $M_\odot$ yr^{-1}, and will mainly occur through short time-scale eruptions rather than through steady winds (Langer 1999, van Marle et al. 2007). Moreover, if the star is more massive than 25 $M_\odot$, it will become a WR star after its red giant or LBV phase (Conti 1976). These stars are highly luminous and display very powerful winds (10^{-5}-10^{-4} $M_\odot$ yr^{-1}). These winds will progressively eject the outer H-rich layers of the stellar envelope, thereby revealing layers that are enriched with the products of former nucleosynthesis processes at the surface. The spectra of these stars display broad emission lines: associated with ions of He and N during what

Table 1.1: The CNO cycle of hydrogen burning in massive stars. The minimum temperature in the core needed for this cycle to dominate the nuclear processes is $\sim 2 \times 10^7$K.

^{12}C	+	^{1}H	→	^{13}N	+	γ		
		^{13}N	→	^{13}C	+	e^+	+	ν
^{13}C	+	^{1}H	→	^{14}N	+	γ		
^{14}N	+	^{1}H	→	^{15}O	+	γ		
		^{15}O	→	^{15}N	+	e^+	+	ν
^{15}N	+	^{1}H	→	^{12}C	+	^{4}He		
and in 0.04% of the cases:								
^{15}N	+	^{1}H	→	^{16}O	+	γ		
^{16}O	+	^{1}H	→	^{17}F	+	γ		
		^{17}F	→	^{17}O	+	e^+	+	ν
^{17}O	+	^{1}H	→	^{14}N	+	^{4}He		

is called the WN sequence, and due to ions of He, C and O during the WC sequence. For single stars, the appearance and lifetime of these stages depend on the initial mass of the star, the mass-loss rate and its evolution during the life of the star, the initial chemical composition and the rotational velocity (Meynet et al. 2008).

When the temperature in the core reaches 10^8 K, new nuclear reactions begin, burning He into C. Once the He is consumed in the core, a He-burning layer above the inert C core will appear, until the temperature in the core reaches $\sim 6 \times 10^8$ K and the C begins to burn into O. This stage is only possible for stars of initial masses higher than 9 $M_\odot$. Similar stages will then follow for the combustion of O into Ne, Ne into Mg, Mg into Si and finally Si into Fe for temperatures in the core exceeding $\sim 3 \times 10^9$ K and initial masses higher than 11 $M_\odot$. Each step is shorter than the previous one, and the evolution thus accelerates progressively. At the end of their life, massive stars display an “onion skin” structure, with an inert iron core and successive shells of burning elements (see Fig. 1.1).

The inert Fe core continues to contract all over this stage, and its density increases rapidly. When the core temperature reaches $\sim 5 \times 10^9$ K, protons and energetic electrons will combine to form neutrons and neutrinos, which will lead to the creation of an extremely dense neutron core. The layers of the stars, that will slowly continue to collapse, will then bounce back on this “stony heart” and be ejected. The energy liberated by these shocks reignites the nuclear fusion in the envelope.

The neutrinos, on the other hand, are trapped a few tens of a second in the neutron core, then burst out and catch up with the shock wave,

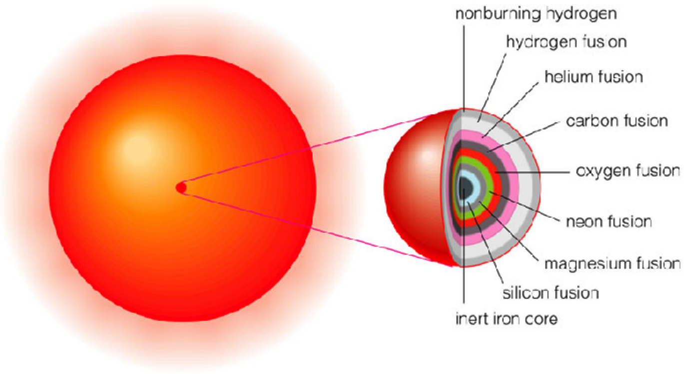

Figure 1.1: The onion-skin structure of the core of a massive star at the end of its life (Credits: Pearson Education, Addison Wesley, 2004).

making the envelope explode in a supernova and expand into space. The chemical elements beyond Fe are only produced during this supernova (SN) phase: Zn, Au, Pb,... The supernova explosions are categorized according to the chemical composition of the exploding star: if there is still some H in the envelope, it is called a type II SN, and if not it is a type Ib or Ic SN, for the explosion of WN and WC stars respectively, that have already ejected their H layers through stellar winds. If the remaining core has a mass between 1.4 and $\sim 2-3$ $M_\odot$, it becomes what is called a pulsar, i.e. a neutron star with a high rotational velocity and a strong magnetic field. If the mass of the core is higher, the collapse continues and eventually forms a stellar-mass black hole.

1.2 Binary systems

A binary or multiple system is composed of two or several stars held together by gravitation, orbiting their common centre of mass. Observations of massive stars over the last decades have suggested that a large fraction of these objects are part of such systems (Sana et al. 2012 and references therein), and among them appear a large number of close binaries, often formed by two relatively similar components (i.e. displaying a mass-ratio smaller than a factor of a few). Moreover, the observed fraction of multiple systems could be biased because of the intrinsic difficulties inherent to the observation of two relatively different components (displaying a large mass-ratio or luminosity-ratio). However, this would imply that the binary fraction is even higher than the one we actually observe. Still, the number of observed massive binaries displaying similar components remains significant, which suggests that the formation of massive stars is tightly related to the formation of massive multiple systems. All the systems we studied in this thesis work are multiple systems: HD 149404 and LSS 3074 are binary systems, and HD 17505 and HD 206267 are thought to be at least triple systems.

There are three main theoretical scenarios discussed in the literature to explain the formation process of multiple systems. The first one is based on the fragmentation process, which occurs when a molecular cloud outside equilibrium breaks up in several parts. Under some conditions (Bonnell 2001), each part of the cloud can gravitationally collapse, giving birth to several stars.

The second formation scenario is based on disk processes. When a cloud contracts into a core of a protostar, it can generate an accretion disk around this core. If this disk becomes gravitationally unstable, it can fragment, which in turn leads to the formation of one or more companions for the main star (Adams et al. 1989, Bonnell & Bate 1994). These different protostars then continue to accrete matter from their parental cloud. This formation process would lead to the formation of systems with typical separation similar to the size of the disk, i.e. several tens of Astronomical Units (AU[2]), and with companions displaying masses much lower than the mass of the main star. This scenario is thus not sufficient to explain the formation of close binaries with components of similar masses.

The third category of formation process is the encounter and tidal capture process. The protostars form as single stars and encounter tidal interaction when they pass close to each other, leaving both objects gravitationally bound (Bonnell et al. 1998). However, as in the case of the coalescence scenario for single massive stars formation, this scenario requires a high stellar density and thus can only work in the densest clusters.

Binary systems are observed in various ways: some of them are detectable by eye or with the help of a telescope (the visual binaries), but most of the binary or higher multiplicity systems are too far away from Earth or have too small a separation to be angularly resolved, and we thus need alternative observational techniques to study them, depending on the characteristics of a given system. Among these binary systems, we can cite the spectroscopic and eclipsing binaries.

---

[2] 1 AU = 149 597 870 700 m.

1.2.1 Spectroscopic binaries

A spectroscopic binary is a binary system that displays periodic variations of the wavelengths of its spectral lines. These variations come from the relative motion of the components in our line-of-sight: if the orbital plane is not perpendicular to the line-of-sight, both components will alternately move towards us or away from us during their orbital motion. These motions induce a wavelength shift, related to the Doppler effect: the spectral lines of the approaching component appear blue-shifted, while the lines of the receding component are red-shifted. For a given line, the difference between the observed wavelength (λ) and the wavelength measured at rest in the laboratory (λ_0) is directly related to the radial velocity (V_r, i.e. the velocity projected along the line-of-sight towards the observer) of the observed star:

$$\frac{\Delta\lambda}{\lambda_0} = \frac{\lambda-\lambda_0}{\lambda_0} = \frac{V_r}{c}$$

where c is the speed of light. Hence measuring the wavelength as a function of time allows us to determine the radial velocities.

We usually distinguish two main categories among the spectroscopic binaries:

- The SB1 systems, for which the spectrum of only one component is directly visible. The absence of a second component in the spectrum may have different causes. First, the second component may be a star too faint compared to the visible one. Second, the invisible component could be a compact object (white dwarf, neutron star or black hole) that has no spectral features in the observed wavelength domain. Finally, the third possibility is that the observed object is not a binary system and that the observed periodic variations of the radial velocity have another origin, such as pulsations in a single star.

- The SB2 systems, for which we can measure the radial velocity curves of both components of the binary system.

We can also add a third class of spectroscopic objects consisting of the multiple systems, composed of more than two stars gravitationally bound and orbiting around their common centre of mass. For some of these systems, companions of the central binary system may add their light to the spectrum, thereby "polluting" the central binary spectrum and adding difficulties in the study of this central object, as we will see in Sect. 3.4 and 3.5.

Measuring the Doppler shift of the lines within the spectrum of a SB1 system as a function of its orbital phase gives the radial velocity curve of the brightest component (referred to as the primary). The analysis of this curve permits to determine the mass function of the system:

$$f(m) = \frac{m_2^3 \sin^3 i}{(m_1+m_2)^2} = \frac{K_1^3}{2\pi G} P(1-e^2)^{3/2}$$

where m_1 and m_2 are the masses of the primary and secondary components respectively, i is the orbital inclination of the system, K_1 is the amplitude of the radial velocity curve of the primary, G is the gravitational constant ($6.673 \times 10^{-11} m^3 kg^{-1} s^{-2}$), P is the orbital period and e is the eccentricity of the orbit.

This function is the only available information on the masses in such systems, and is not sufficient to determine the minimum masses ($m_1 \sin^3 i$ and $m_2 \sin^3 i$) of each component.

On the other hand, for SB2 systems, the radial velocity curves of both components are available, making it possible to determine the mass ratio of the system $q = \frac{m_1}{m_2} = \frac{K_2}{K_1}$. Together with the mass function, this ratio permits to determine the minimum masses of the components. The shape of the radial velocity curve can also give us some information on the shape of the orbit. Indeed, if the orbit is circular, the curve will be a sine function. On the other hand, if we are dealing with an eccentric system, the curve will be distorted. It is thus particularly important to sample the whole orbital cycle sufficiently well in order to determine accurately the physical parameters of the system.

In SB2 systems, the main unknown then remains the orbital inclination i of the system. However, if this inclination is close enough to 90° or if the components are sufficiently close to each other, the stars can eclipse each other during the orbital cycle, temporarily decreasing the total observed brightness. Such systems are called eclipsing binaries. The analysis of the light-curve of these systems provides useful information, such as the missing orbital inclination.

1.2.2 Eclipsing binaries

As mentioned in the previous section, the light-curves of eclipsing binaries display periodic decreases over the orbital cycle. These decreases are caused by the passage of one component in front of the other, as seen from the observer's point of view. Therefore, the flux coming from the partly "hidden" star is partly blocked, decreasing the total flux emitted by the system in our direction. The time of what is called the primary eclipse (respectively the secondary eclipse) is the time when the more (respectively less) luminous component is eclipsed by the less (respectively more) luminous one. The closer to 90° the inclination is, the more likely eclipses are. The orbital period of the system can be determined by measuring the time elapsed between two primary eclipses.

The Fig. 1.2 displays a theoretical light-curve of an idealized eclipsing binary, with perfectly spherical stars of uniform brightness on a perfectly circular orbit with an orbital inclination of 90°. In practice, the inclination is often lower than 90°, the orbit may not be circular and the components not perfectly spherically symmetric, which will alter the shape of the eclipses. However, from this idealized light-curve, we can express two simple relations between the radii of the stars (R_1 and R_2 for the most and less luminous stars respectively, also called the primary and secondary stars) and their orbital separation (a):

$$\tfrac{t_4-t_1}{P} = \tfrac{\arcsin\left(\frac{R_1+R_2}{a}\right)}{\pi} \text{ and } \tfrac{t_3-t_2}{P} = \tfrac{\arcsin\left(\frac{R_1-R_2}{a}\right)}{\pi} \, .$$

The shape of the light-curve mostly depends on the relative brightness and size of the stars, and on the orbital inclination. The inclination will affect the depth of the eclipses (the closer to 90° i is, the deeper the eclipses are), while the radii and luminosities will also affect the general shape of the curve, in addition to their effect on the depth. In close eclipsing binaries (periods of a few days), the separation between the stars is small, not much larger than the sum of the radii, and the orbit is often circular. In such cases, the time between two consecutive eclipses is almost equal, i.e. half of the orbital period. In addition to the genuine eclipses, another type of photometric variations can also occur because of the tidal interactions that deform the stars within close binary systems, giving them a rather drop-like shape, with the extremities facing each other. In such cases, the geometrical surface of the stars as seen from the observer changes during the orbital cycle, which makes the total observed light undergo what is called ellipsoidal variations. These variations can either be the only observed variations of the light-curve if the inclination of the system is low, or be superposed on the eclipses in the case of an eclipsing binary. They are generally of lower amplitude than the variations due to eclipses, but are also useful to constrain the inclination of the system.

Some numerical codes, such as NIGHTFALL, can be used to fit a theoretical light-curve to the observations in order to derive the best corresponding parameters of the system. However, such codes need some input parameters in order to constrain the best solution. Since several model parameters have similar effects on the light curve, there exists a

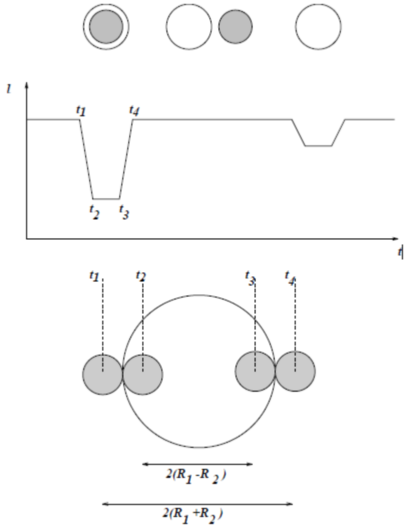

Figure 1.2: The upper panel displays the theoretical light-curve of an idealized eclipsing binary and the corresponding position of both stars as seen by the observer. The white circle represents the primary, while the grey one represents the secondary. The lower panel shows the relative positions of both stars during the primary eclipse: the occultation of the primary by the secondary begins at t_1, is maximal between t_2 and t_3, and ends at t_4. These key times of the eclipse are shown on the light-curve of the upper panel. (Credits: Gregor Rauw, in his lectures *Variable Stars*, 2013.)

degeneracy and, as a result, the solution may not be unique. It is thus better to study the systems also through other methods, such as spectroscopy, in parallel to photometry. However, few systems have an inclination close enough to 90° to display such photometric variations. Nevertheless, the study of eclipsing spectroscopic binaries is currently the only reliable method to determine the absolute masses of the stars, and is thus an essential tool to improve our understanding of stellar evolution[3].

---

[3] Another technique that has recently started to deliver promising results is the joint analysis of spectroscopic and interferometric observations for wide binary systems (e.g. Le Bouquin et al. 2017).

1.3 Interactions in massive binary systems

In the previous section we introduced the main categories of binary systems, how to observe them and how to interpret the variations we observe in their spectra or light-curves. These variations are only due to our particular observer status, and are not due to genuine interactions between the components. However, Sana et al. (2012) showed that the majority of massive stars are part of close binaries and will eventually interact with their companion during stellar lifetimes, and one third of the systems will interact while both stars are still on the main sequence. Such interactions may strongly influence the subsequent evolution of the components in such systems. We will here introduce four types of interactions that are relevant in the context of this thesis work : the collision between the stellar winds of both components, the Roche lobe overflow (RLOF) mechanism, the influence of binarity on the rotational mixing within the stellar atmospheres and the common-envelope evolution. We will also briefly discuss the possible characteristics of post-interaction binary products.

1.3.1 Wind-wind interactions

When two massive stars are part of a binary system, their stellar winds interact with each other, especially in close binaries. That is what is called colliding-wind binaries. This interaction can be either a collision between the two stellar winds, or in some cases the collision between one of the winds and the surface of the companion. Either ways, it breaks the spherical symmetry of the wind, and leaves some signatures throughout the electromagnetic spectrum of the system.

The wind interaction region is limited by two hydrodynamical shocks, each facing one of the components. If the winds have similar terminal velocities and densities, the surface of contact discontinuity between the shocks is theoretically a plane midway between both stars (Fig. 1.3(a)). If the winds are significantly different, the momentum fluxes will be different, and the contact discontinuity will no longer be a plane, but rather a curved surface with the concave side facing the star with the less energetic wind (Fig. 1.3(b)). The region between the shocks is called the wind interaction zone. The interaction of two stellar winds is however a complex hydrodynamical phenomenon, that can undergo large instabilities affecting the shape of the interaction zone (Stevens et al. 1992). Moreover, in the specific case of close massive binaries, the Coriolis force due to the orbital motion of the stars also has a strong impact on the shape of the shocks and the interaction zone (e.g. Pittard & Parkin 2010).

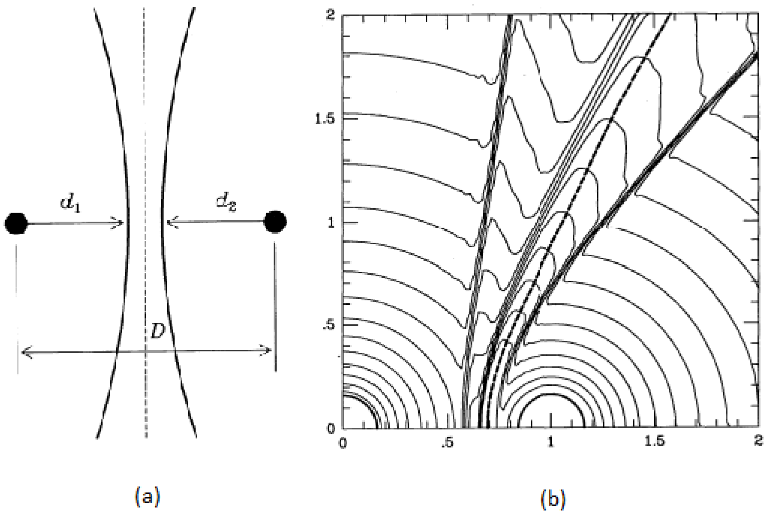

Figure 1.3: The (a) panel displays a schematic diagram of colliding stellar winds of identical strengths. The dashed line represents the contact discontinuity, at equal distance from both stars. The solid lines represent the two hydrodynamical shocks (Stevens et al. 1992). The (b) panel displays a hydrodynamic simulation of two stellar winds with different momentum fluxes (Stevens et al. 1992). The primary star is located at the origin of the axes, and the secondary star on the x-axis at x= 1. The dashed line is the surface of momentum balance (see Stevens et al. 1992 for more details) and the converging density contour lines in between the two wind shocks indicate the contact discontinuity. (Credits: Stevens et al. 1992).

Since the strong winds of WR and O stars display supersonic velocities (terminal velocities of 1000-3000 km s^{-1}), the main signature of the shock-heated plasma in the collision zone between these winds is expected to occur in the X-ray domain, with the associated emission displaying significant phase-locked variability, as a consequence of the changing wind opacity along the line of sight towards the interaction zone, or as a result of changing orbital separation in the case of eccentric binaries (Cazorla et al. 2014, see Rauw & Nazé 2016 for a review). However, we can see quite a few discrepancies with observations: some systems display either significantly stronger or lower emission in the X-ray domain than expected by the models, or lack the phase-locked variations in their emissions (see e.g. Rauw & Nazé 2016).

Other signatures of the interaction zone can also be observed in other wavelength domains, such as phase-locked profile variations of some optical and UV lines of massive binaries, as we will see later in this work. For example, the Hα and He II λ 4686 lines can display extra emission as a function of the orbital phase, as shown in Fig. 4 of Raucq et al. (2017), Sect. 3.3 of the present work. In some cases, the interaction zone can also create features in the radio or infrared domains, but these specific cases go beyond the field of this thesis and will not be further discussed here.

1.3.2 Roche lobe overflow mechanism

If we consider two stars on circular orbits around their common centre of mass, both stars being in synchronous rotation (i.e. the rotation periods equal their orbital period), then each stellar surface will adopt the shape of an equipotential of the Roche potential. The Roche potential accounts for the gravitational field of both stars (assumed to act as point-like masses) and for the effect of the centrifugal force in a frame of reference rotating with the orbital motion of the stars. Other equipotential surfaces will be found around these first two, approximately spherical and concentric with the nearest star. They become ellipsoidal when the distance to the nearest star increases, until forming what is called the Roche lobe of the system, which is the very first equipotential that contains both the primary and secondary stars. This is shown in Fig. 1.4. The Roche lobe of a given star is defined as the region of space in which the orbiting material is gravitationally bound to that very star. It displays a tear-drop shape, with the apex of the tear-drop pointing towards the other star. The point of contact between the two tear-drops is the L1 Lagrange point. This is the first point of relative equilibrium of the system. There are four other Lagrange equilibrium points: L2, L3, L4 and L5, as shown in Fig. 1.4. For the discussion of binary systems, the most important Lagrangian points are L1, L2 and L3.

At the beginning of their life, both stars within a binary system evolve essentially like single stars. If one of the components (usually the more massive one) expands beyond its Roche lobe, the material outside of the lobe will not be bound to the star anymore and may either leave the system, or fall towards the companion, through the L1 point. This is called a Roche Lobe OverFlow (RLOF) process. If the mass gainer is close to filling its own Roche lobe, the matter directly hits the stellar surface. Otherwise, it will form an accretion disk around the gainer star. The Roche lobe thus sets a physical limit to the expansion of a star in a close binary system, on the contrary of the single star case, in which the star can expand during its evolution to very large radii. A binary system is said detached, semi-detached or in contact when no star, one

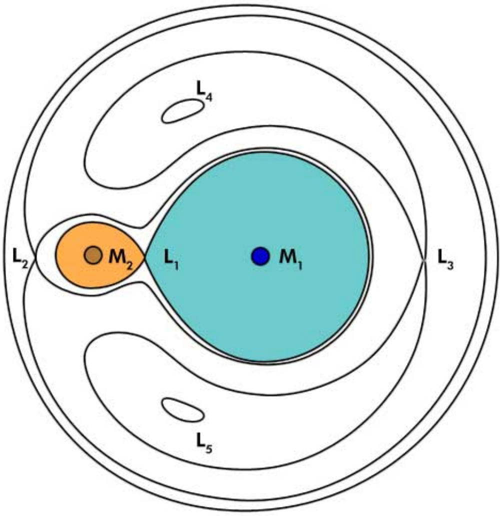

Figure 1.4: Illustration of the Roche potential in a binary system composed of two stars of masses M_1 and M_2. The points L_i represent the five Lagrangian points of equilibrium.

star or both stars fill up their Roche lobes, respectively. If both stars expand beyond their Roche lobes, the system is said in over-contact, and no matter can be accreted by the companion anymore.

The RLOF episodes are classified into three different categories, depending on the evolutionary stage of the concerned star when the process occurs (Kippenhahn & Weigert 1967; Vanbeveren et al. 1998):

- Case A: The primary star is still burning hydrogen in its core when encountering a RLOF episode. This situation usually takes place in very close systems, with orbital periods of $2-4$ days. This category of mass-transfer episode is generally rather slow, and may last several Myr. Mass transfer typically occurs via direct impact onto the surface of the secondary. This phase usually ends when the secondary star has accreted enough material to fill its Roche lobe and the two stars come into contact and may merge (for very short periods, P<2 days) or when the primary star leaves the main sequence (for periods P $\sim 2-4$ days), triggering a new mass transfer phase (Case AB).
- Case B: The primary is in a H burning shell phase and has not yet

begun to burn helium in its core. It occurs for periods ranging from 4 days to 1000 days. Mass accretion in these systems occurs typically via an accretion disk. The mass transfer rate is higher for wider systems, in which the donor is more evolved when the RLOF episode begins (De Mink et al. 2013). On the other hand, these authors have also shown that tighter systems evolve more conservatively, resulting in more massive secondaries in comparison to wider systems. Surprisingly, in their simulations, the remaining main-sequence lifetime of the secondary seems roughly independent of the amount of accreted mass or the orbital period, as a consequence of two counteracting effects. Indeed, if higher stellar mass due to efficient accretion implies shorter evolutionary timescales, i.e. a reduction of the remaining lifetime, the mass accretion also results in mixing of fresh hydrogen into the central regions, extending the remaining lifetime. Most systems with extreme mass ratios encountering a case B RLOF episode are expected to enter a phase of common envelope evolution soon after the onset of mass transfer (see Sect. 1.3.4). The tighter systems are expected to result in a merger, with a post-main-sequence star product, either a blue or red supergiant. In wider systems, the binding energy of the envelope of the primary is smaller and the momentum and energy in the orbit are larger, and the envelope can be ejected.

- Case C: When the orbital period is larger than 1000 days, the RLOF takes place when the primary has exhausted the He in its core. When the primary star loses mass, we assume it reacts by expanding, resulting in very high mass transfer rates. As the Roche lobe typically shrinks, this leads to a common envelope phase (De Mink et al. 2013).

Note that the period ranges quoted here are only rough indications and depend on the mass of the donor star and on the metallicity of the system. For stars with initial masses larger than 40 $M_{\odot}$, the mass decrease is mainly due to the strong stellar wind during the LBV phase, reducing the importance of the RLOF as a mass-losing process (Vanbeveren et al. 1998).

The mass transfer during a RLOF episode is far from being an anecdotic process: it has a huge role in the subsequent evolution of the components. Indeed, it changes the relative masses, luminosities and effective temperatures of both stars, thus changing their spectral types. It also strongly affects the surface chemical abundances, since the primary loses the H-rich layers of its atmosphere, revealing the deeper layers affected by the CNO cycle. The CNO abundances at the surface of the primary star are thus enhanced (Vanbeveren 1982). Moreover, if the secondary accretes during the RLOF episode, it may also receive CNO enhanced material from the primary, thus displaying slight overabundances in those elements at its surface (Vanbeveren & de Loore 1994). It will further receive angular momentum during the transfer, since the angular momentum of the whole system is conserved, which will speed-up its rotational velocity (Vanbeveren & de Loore 1994) and may induce enhanced rotational mixing which will affect the subsequent evolution of the secondary (see Sect. 1.3.3).

For massive binaries, the massive overcontact binary (MOB) evolution has also been proposed by Marchant et al. (2016) to be an alternative formation channel of double compact objects (white dwarfs (WD), neutron stars (NS) and black holes (BH)) binary systems. This scenario involves the chemically homogeneous evolution of rapidly rotating and very massive stars in tidally locked binaries, i.e. very close binary systems. Indeed, such very close and massive binaries are supposed to evolve into contact, with both binary components filling and even overfilling their Roche lobes. The evolution during the over-contact phase differs from a classical common-envelope phase (see Sect. 1.3.4) as co-rotation can, in principle, be maintained by the strong tidal forces as long as material does not overflow the L_2 point. This means that a spiral-in due to viscous drag can be avoided, resulting in a stable system evolving on a nuclear timescale. In this case, the stars remain fully mixed due to their tidally induced high spin.

Once both stars overflow past the outer Lagrangian point, L_2, Marchant et al. (2016) expect the system to merge rapidly, either due to mass loss from L_2 carrying a high specific angular momentum or due to a spiral-in due to the loss of co-rotation. However, these authors find that a large number of MOBs may swap mass several times but survive as a close binary until the stars collapse. These MOB systems can thus lead to the formation of double black holes binaries that will eventually merge within a Hubble time. The figure 1.5 illustrates the binary stellar evolution of a given system leading to the formation of such BH + BH binary.

The merger delay time, i.e. the time between the formation of the BH + BH binary and the eventual merger, is a strong function of metallicity, where the merger delay times (at a given BH mass) are systematically shorter for lower metallicity. Moreover, if the black holes receive kicks at birth, even higher-metallicity systems may merge very rapidly if the kick reduces the pericenter distance. One of the advantages of this scenario is that it can lead to the formation of much more massive double BH binaries compared to other evolutionary pathways. Marchant et al. (2016) were also able to reproduce observed local counterparts of various stages in the

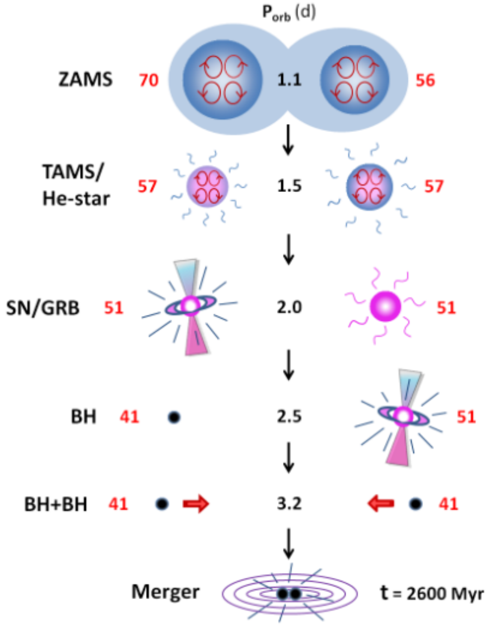

Figure 1.5: Illustration of the binary stellar evolution of a given $70\,M_\odot + 56\,M_\odot$ close binary system at a $Z_\odot/50$ metallicity (Marchant et al. 2016). The masses of the stars in solar masses are indicated with red numbers, and the orbital periods in days are given as black numbers. A phase of contact near the ZAMS causes mass exchange. Acronyms used in the figure. ZAMS: zero-age main sequence; TAMS: termination of hydrogen burning; He-star: helium star; SN: supernova; GRB: gamma-ray burst; BH: black hole. (Credits: Marchant et al. 2016).

MOB scenario, such as HD 5980, IC10 X-1 and NGC 300 X-1.

1.3.3 Rotational mixing

The rotation is thought to be a major factor in the evolution of massive stars, with huge consequences for their chemical compositions, ionizing fluxes and final fates (De Mink et al. 2009). Evolutionary models predict that rotation has major effects on the core hydrogren-burning phase (Maeder & Meynet 2000; Heger & Langer 2000; Hirschi et al. 2004; Yoon

& Langer 2005; Brott et al. 2011b; Potter et al. 2012; Ekström et al. 2012), and there is growing evidence that in a fraction of massive stars, the final collapse and explosion is governed by rapid rotation, giving rise to hyper-energetic supernovae and long-duration gamma-ray bursts (Yoon et al. 2006; Woosley & Heger 2006; Georgy et al. 2009). Models of rotating single stars can also successfully account for the surface enhancements of N and He observed in massive main-sequence stars, but recent observations have questioned the idea that rotational mixing is the main process responsible for the surface enhancements, and other theories suggest that stellar winds and binary interactions are probably at least partly responsible of such modifications of the surface abundances (De Mink et al. 2009).

The origin of the distribution of initial stellar masses and initial stellar rotation rates are not yet fully understood (e.g. Krumholz 2011; Rosen et al. 2012). For example, it is a key issue whether stars inherit their rotation rates from their parental molecular clouds, since the specific angular momentum of such clouds is several orders of magnitudes larger than what can be placed in a rotating star (e.g. Bodenheimer 1995). Several observational studies suggest initial median stellar rotation rates for massive stars between $0.20 \times v_{\rm crit}$ (Wolff et al. 2006) and $0.40 \times v_{\rm crit}$ (Huang et al. 2010).

Either way, whatever the origin of their birth rotation rates is, several processes may affect the rotation of massive stars during their life, causing deviations from the initial values:

- Modification of the stellar structure. During core hydrogen-burning, massive stars expand by about a factor of three. However, the corresponding spin-down of the surface layers is prevented by analogous contraction of the stellar core combined with an efficient transport of angular momentum from the core to the envelope (Ekström et al. 2008; Brott et al. 2011a), and the rotational velocity at the equator, $v_{\rm rot}$, increases slightly over the main-sequence evolution of the star, until it reaches a value close to the Keplerian rotation rate. In the absence of an efficient angular momentum loss mechanism, the star remains rotating close to this Keplerian limit, which drops as the star evolves and expands. The change in radius of more massive stars during the main sequence is larger, resulting in a more significant drop in the Keplerian velocity. As a result, the Keplerian rotational velocity at the end of the main sequence is around 400 $\rm km\,s^{-1}$ with only a weak dependence on the stellar mass. In the most luminous stars the effects of radiation pressure cannot be ignored and the Keplerian limit should be considered as an upper limit to the physical maximum.

- Stellar winds. Massive stars lose angular momentum due to their strong stellar winds (Langer 1998). This loss is stronger for stronger winds, and the spin-down by winds thus does play a significant role at higher mass and metallicity (Vink et al. 2001) and for more rapid rotation (Friend & Abbott 1986). However, major uncertainties remain on the mass-loss rates in massive stars, leading to uncertainties on the effect of stellar winds.
- Binary interaction. This is likely the most important channel of rotational changes for the population of massive stars. Stars in binary system may either lose or gain angular momentum through interaction with their companion. The spin rate of both components can be drastically affected by several effects.
    - Tides: In close binary systems, the tidal interactions tend to synchronize the rotation of the stars with the orbit. The system tends to evolve towards a state of minimum mechanical energy due to dissipative processes. This is an equilibrium state, where the orbit is circular, the spins of the stars are aligned and perpendicular to the orbital plane and the stars are in synchronous rotation with the orbital motion, such that $P_{\rm spin} = P_{\rm orb}$. How quickly this equilibrium state is approached depends on the efficiency of the processes responsible for the energy dissipation. This phenomenon is responsible for a gradual increase in rotational velocity for both stars, since they are kept in corotation with the orbit as they expand.
    - Mass transfer: During mass transfer episodes in close massive binaries, the matter lost from the primary star will carry a certain angular momentum, which may slow down the outer layers of the primary atmosphere. On the other hand, part of this matter and angular momentum can be transferred to the companion star, spining up the top layers of the secondary star, and angular momentum is then transfered further into the star due to rotationally induced mixing processes.
    - Merging of the two stars: De Mink et al. (2014) have shown that a significant fraction of close massive binaries will end their life as systems in a merging event (see Sect. 1.3.5), leading to the formation of bright, rapidly rotating stars or compact objects.

De Mink et al. (2013) estimated that, because of binary interactions, 20^{+5}_{-10}% of all massive main-sequence stars have projected rotational velocities in excess of 200 $\mathrm{km\,s^{-1}}$ compared to the original birth distribution, the main uncertainties being the mass transfer efficiency and the possible effect of magnetic braking, which may also have a spin-down effect. Most of the more rapid rotators, according to these authors, are products of a RLOF episode. A smaller number are merger products.

1.3.4 Common-envelope evolution

Common-envelope (CE) evolution is thought to play an important role in the formation of numerous close binaries composed of two compact objects. Indeed, as we have already discussed earlier, binary processes are needed to explain some observed properties of some systems, such as the current small orbital separation, often much smaller than the radii of the progenitors, of some objects. In such cases, the CE evolution is a good candidate, since it is accompanied by a drag-force, arising from the motion of the in-spiralling object through the envelope of its companion star, which leads to the dissipation of some orbital angular momentum and the deposition of orbital energy in the envelope. Hence, the global outcome of a CE phase is a reduced binary separation and ejected envelope, unless the stars composing the system merge. The in-spiral of the companion star can decrease the orbital separation by a factor of ~100 or more (Kruckow et al. 2016).

The main steps of CE evolution leading to a BH + BH system are presented in Fig. 1.6.

There is observational evidence of such orbital shrinkage in a number of known binary pulsars and WD pairs with an orbital period of a few hours or even less. The central question in the CE theory is whether a massive binary will survive a CE evolution or result in an early merger event without ever forming a double compact system. For example, in this theory, the systems always enter a CE phase after the high-mass X-ray binary (HMXB) stage, during which the secondary massive star becomes a red supergiant and captures its BH companion (Kruckow et al. 2016). Whether the donor star envelope is ejected successfully depends on the binding energy of the envelope, the available energy resources to expel it and the ejection mechanism.

The possible ejection of the envelope thus depends on the mass and radius of the donor star. Envelope ejection is facilitated for giant stars compared to less evolved stars, and, as long as the in-spiralling BH mass is high enough, they probably succeed in ejecting the envelopes of their host stars (Kruckow et al. 2016). However, if the in-spiralling object moves too far inward, there is no possibility of ejecting the envelope, and the system merges.

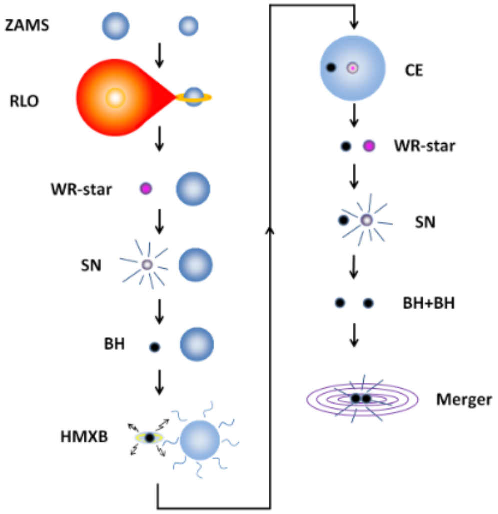

Figure 1.6: Illustration of the binary stellar evolution leading to a BH + BH system according to the standard CE scenario. Acronyms used in the figure. ZAMS: zero-age main sequence; RLO: Roche lobe overflow; WR-star: Wolf-Rayet star; SN: supernova; BH: black hole; HMXB: high-mass X-ray binary. (Credits: Tauris & van den Heuvel 2006).

In practice, CE evolution, in addition to producing double WD and double NS binaries, may in principle also produce massive double BH systems, with individual BH component masses of up to 60 $M_{\odot}$. Beyond these masses, a pair-instability supernova (SN) is expected to lead to complete disruption of the progenitor star, without leaving any compact remnant (Kruckow et al. 2016 and references therein).

1.3.5 Binary products

As we have shown in the previous sections, binarity has a huge impact on the evolution of the stars within such systems. Because a large fraction of massive stars are born as members of binary systems (Sana et al. 2012), populations of massive main-sequence stars are strongly affected by such disturbed evolution, and contain a non-negligible amount of mergers and binary products. Wellstein et al. (2001) find that the fraction of the parameter space where binaries may evolve while avoiding contact, which they found already small for the least massive systems considered, becomes even smaller for larger initial primary masses. Assuming constant star formation, de Mink et al. (2014) find that $8^{+9}_{-4}\%$ of a sample of early-type stars are the products of a merger resulting from a close binary system, and $30^{+10}_{-15}\%$ of massive main-sequence stars are the products of binary interactions.

These authors started their simulations with 70% binaries and 30% single massive stars at birth. For the case of continuous star formation, their simulations end up to the results shown in Fig. 1.7. The contribution of pre-interaction binaries in the current population goes down from 70% to 50%, 22% of the stars are referred as single stars, and more than a quarter of the stars have been severely affected by interactions with a companion. This group of post-interaction stars are composed of mergers (8%), semi-detached systems (i.e. systems currently undergoing mass transfer through RLOF; 3%) and stars that have previously gained mass from a (former) companion (17%). The latter group is composed by systems containing a main-sequence star accompanied by a helium star, a NS, a WD or a BH. Note that the low percentage of systems currently undergoing RLOF episodes is easily explainable by the short timescale of such events, typically a few thermal timescales at most, compared to the stellar lifetime. In their study of incidence, de Mink et al. (2014) did not take into account post-interaction double compact systems. They conclude that it is completely counter-productive to exclude detected binaries from a sample of early-type stars to reduce the contamination by binary products on population statistics, since binary products are typically not detected as such and will therefore represent a larger fraction of the sample than genuine single stars.

In addition to such main-sequence binary products, we have also seen in Sect. 1.3.2 and Sect. 1.3.4 that massive binary systems may also evolve into double compact systems, and particularly into BH + BH systems. What is important to note with such BH + BH systems is that, if they are close enough, they may rapidly merge, leading to potential sources of gravitational waves. Kruckow et al. (2016) have shown that the CE formation channel in a low metallicity environment for binary systems with initial masses of $\sim 50\ M_\odot$ may lead to the production of relatively massive systems like the progenitor of GW150914 and give birth to gravitational waves. Moreover, these authors have shown that the CE formation channel could also explain the progenitor of GW151226 regardless the metallicity of its environment.

Another interesting consequence of binary evolution could be the generation of a strong magnetic field via a dynamo operating because of differential rotation and convection during CE evolution that (nearly) leads

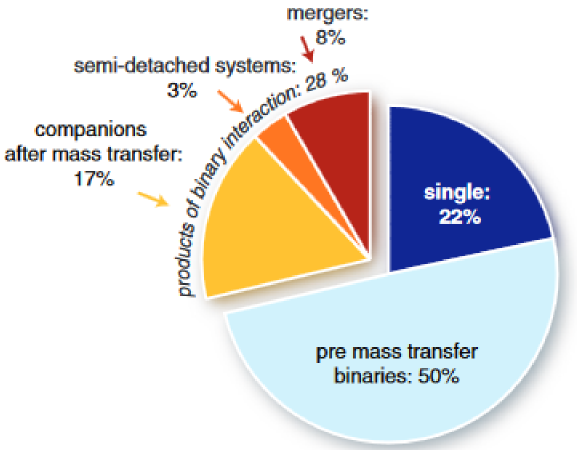

Figure 1.7: Incidence of stellar mergers and binary products in the standard simulation of De Mink et al. (2014) of a population of massive main-sequence stars, assuming continuous star formation and an initial binary fraction of 70% (Sana et al. 2012). Percentages are expressed in terms of the number of systems containing at least one main-sequence star. (Credits: De Mink et al. 2014).

to a merger (Tout et al. 2008, Schneider et al. 2016). Observationally, it has been found that about 7-10 % of main-sequence (MS) OBA stars host strong, large-scale magnetic fields (e.g. Donati & Landstreet 2009; Ferrario et al. 2015; Fossati et al. 2015), and a similar incidence is found in pre-MS Herbig Ae/Be stars (Wade et al. 2007; Alecian et al. 2013). Quite remarkably, the incidence of such kG magnetic fields seems to be significantly lower among close massive binary systems (2 %; Neiner & Alecian 2013; Alecian et al. 2015). There are three main scenarios that have been proposed to explain the origin of large-scale magnetic fields in early-type stars: (1) fossil fields inherited from the proto-stellar cloud, (2) a dynamo mechanism and (3) shear in the product of the merger of MS or pre-MS binaries. Schneider et al. (2016) argue that mergers offer a natural explanation for the restricted fraction of massive stars displaying a strong, large-scale magnetic field (as we have discussed earlier, de Mink et al. (2014) predict that about 8 % of all massive MS stars would be merger products), as well as for the very low incidence of strong magnetic MS stars in close binary systems.

An interesting and useful fact is that MS merger products will be rejuvenated (Schneider et al. 2016 and references therein), i.e. they will appear younger than other stars formed at the same time such as other cluster members and companions in multiple systems. This rejuvenation is due to mixing of fresh fuel into the cores of merger products and shorter lifetimes associated with more massive stars, and is of the order of the real age of the merger, i.e. of the order of the nuclear timescale of the star. The rejuvenation is the stronger the more evolved the progenitors, the lower the masses of binaries and the larger the mass ratios. On the other hand, merging pre-MS stars will not necessarily rejuvenate. They can lead to merger products that reach the ZAMS either earlier because of the decreased contraction timescale due to the increased mass, or later because of the additional orbital energy that has to be radiated away before the core heats up enough to start hydrogen burning. In any case, the delay is of the order of the thermal timescale and therefore practically undetectable.

As a conclusion, we can say that binary products are probably rather common in a massive star population, and not always easily distinguishable from single stars. However, there are a number of hints that can help to identify individual binary products, even if not all binary products are expected to show all these characteristics and none of the characteristics uniquely signifies binary interaction.

- Surface abundances anomalies may be found in binary products, indicating enhanced mixing, loss of the outer layers of the stellar atmosphere or accretion of enriched gas.

- Peculiar rotation rates (see Sect. 1.3.3).

- If binary interaction occured recently, there may be signs of shedded material in the circumstellar medium, either an ejection nebula or a circum-stellar disk. The typical lifetime of such a nebula is expected to be $\sim 10^4$ years (Langer 2012).

- Several studies (e.g. Tout et al. 2008; Ferrario et al. 2009; Schneider et al. 2016) suggest that the merging of two stars may lead to the generation of a strong magnetic field.

- The supernova explosion of the primary may cause the system to break up, leading to the creation of “runaway” or “walk-away” secondary stars.

- Binary products are not expected to have a main-sequence companion not showing any unusual properties.

- If the former companion which has become a compact object is still present, the system may show UV or X-ray excess when the compact object accretes material from its companion.
- Within their birth clusters, the binary products may be over-luminous and possibly appear younger than the age of the cluster.

1.4 The present work

In the previous sections, we have seen the importance of massive stars in the Universe, and the huge influence of the multiplicity on the evolution of such stars. It is thus of the utmost importance to accurately constrain the multiplicity and the fundamental parameters of individual components in order to better understand the evolution processes in a given binary system, and thus improve our understanding of these key ingredients of the Universe.

In this context, this thesis consists in the in-depth study of four multiple systems, using high-quality observations. For each object, we have used a disentangling procedure to separate the contributions of each component to the observed spectra of the system. In this way, we were able to determine the individual parameters of each component as if the stars were single. We have then determined the spectral types of each component, and the brightness ratio of the system. This preparatory analysis permitted us to determine the rotational and macroturbulence velocities, and the fundamental properties of each star.

The two main numerical tools used in this study, the disentangling procedure and the CMFGEN model atmosphere code, are presented in the next chapter.

The third chapter is then dedicated to the individual study of each system: HD 149404, LSS 3074, HD 17505 and HD 206267.

Finally, in the last chapter, we recall the main results that we obtained, present the conclusions of this work, and propose some perspectives of future work that could be done to complement this study and further improve our knowledge and understanding of massive binary stars.

Chapter 2

Numerical tools and methods

2.1 Spectral disentangling

2.1.1 Method

As we have seen in the previous chapter, the study of individual components of a binary system is important to better understand the underlying physics of the system. In order to recover the separate contribution of both components to the observed binary spectrum, we applied a spectral disentangling method. This way, we were able to study the fundamental parameters of each star as if it were single.

For this purpose, we used our disentangling routine (Rauw 2007), which is based on the Iterative Doppler differencing technique developed by González & Levato (2006). This method was previously used by, e.g., Linder et al. (2008), and improved by Mahy et al. (2012) to introduce a third contribution in the spectra, either a third component of the system or the ISM contribution.

The technique is based on an iterative process that allows to calculate both the spectra of the components and their radial velocities, in a spectroscopic binary system. The technique operates on the normalized spectra of the binary system. It uses alternately the spectrum of one component to calculate the spectrum of the other one. The spectra are expressed in a logarithmic scale, i.e. as a function of $x = ln\,\lambda$ instead of λ. Since the radial velocities in normal binary systems are quite small compared to the speed of light, this permits to express the Doppler shift in the following uniform way

$$\begin{aligned}
\ln\lambda &= \ln\left[\lambda_0\left(1+\frac{v}{c}\right)\right] \\
&= \ln\lambda_0 + \ln\left(1+\frac{v}{c}\right) \\
&\simeq \ln\lambda_0 + \frac{v}{c} \\
\Rightarrow x &\simeq x_0 + \frac{v}{c}
\end{aligned}$$

For the typical values of radial velocities in binary systems, the Doppler effect hence results in a simple linear shift of the wavelength scale.

The first step is to remove the interstellar contribution to the observed spectra, by setting the flux in the wavelength regions where they appear to unity, in order to keep only the contributions of the components of the system. The observed spectrum can thus be expressed as:

$$S(x) = A\left(x - \tfrac{v_A(\phi)}{c}\right) + B\left(x - \tfrac{v_B(\phi)}{c}\right)$$

with $A(x)$ and $B(x)$ the spectra of the primary and the secondary stars, respectively, in the heliocentric frame of reference, and $v_A(\phi)$ and $v_B(\phi)$ their respective radial velocities at the given orbital phase ϕ.

In order to recover the individual spectra of each component, we use an iterative process:

1. For each observation i, we subtract the current best estimate of the spectrum of component B, shifted by the radial velocities of the secondary component at the corresponding phase, from the observed spectra.

2. The residual spectra are cross-correlated with a mask to obtain improved estimates of the radial velocities of the primary component for each observation. The residual spectra are then shifted into the primary's frame of reference and combined into a weighted mean to yield our new best approximation of star A's spectrum.

3. We calculate the current best approximation of the spectrum of the secondary, B, similarly to step 1, but reverting the roles of A and B of step 1.

4. We refine the radial velocities of the secondary component, similarly to step 2.

In order to begin this iterative process, a first approximation of the radial velocities is thus needed, then refined during the calculations. It is also possible to fix the radial velocities to the values obtained from known orbital solution of the system for the entire calculation. We chose this solution for this thesis work, in order to avoid the appearance of problems that can arise in the RV determination (steps 2 and 4) when the lines of both components are not easily seen on the spectra. Another input needed to start this iterative process is a first approximation of the spectrum of one of the components. A flat spectrum is usually used for the component B as a starting point for the iterations. The spectrum A thus contains all spectral features of the observed spectra at the beginning of the process.

The final spectra of the primary and secondary stars can thus be expressed as follows:

$$A(x) = \frac{1}{n}\sum_{i=1}^{n}\left[S_i\left(x + \frac{v_A(\phi_i)}{c}\right) - B\left(x + \frac{v_A(\phi_i)}{c} - \frac{v_B(\phi_i)}{c}\right)\right]$$

and

$$B(x) = \frac{1}{n}\sum_{i=1}^{n}\left[S_i\left(x + \frac{v_B(\phi_i)}{c}\right) - A\left(x + \frac{v_B(\phi_i)}{c} - \frac{v_A(\phi_i)}{c}\right)\right]$$

where n is the number of observations and $v_A(\phi_i)$ and $v_B(\phi_i)$ are the radial velocities of the primary and secondary stars, respectively, at phase ϕ_i. These expressions represent averages of the observed spectra from which the secondary (resp. the primary) spectrum shifted by the appropriate velocity has been subtracted (González & Levato 2006). In each iteration, the residuals of the secondary lines still present in the A spectrum are reduced approximately by a factor $1/n$. The convergence and the quality of the reconstructed spectra of the primary and secondary components thus directly depend on the number of observed spectra. The quality of the input data has also a strong influence on the quality of the output spectra, especially for the weakest component, as we will further discuss in Sect. 2.1.2 and Sect. 3.3.

A generalisation of this method has been performed by Mahy et al. (2012) in order to introduce a third component to the spectra, either a third stellar companion or the interstellar lines. The observed spectra can thus be expressed by

$$S(x) = A\left(x - \frac{v_A(\phi)}{c}\right) + B\left(x - \frac{v_B(\phi)}{c}\right) + C\left(x - \frac{v_C(\phi)}{c}\right).$$

This technique is similar to that for a binary system: the third component is first approximated by a flat spectrum, then we successively calculate the mean spectra of two components, shifted by their respective radial velocities, and subtract them from the observed spectra in order to compute the mean spectrum of the remaining component. At each iteration, we create temporary residual spectra from the observed spectra from which the contributions of two components have been subtracted and we apply a cross-correlation technique on these templates to refine the determination of the radial velocities of the third object. For each iteration, this process is applied to each component of the system.

At the end of the process, the mean spectra of each component can be expressed by

$$A(x) = \frac{1}{n}\sum_{i=1}^{n}\left[S_i\left(x + \frac{v_A(\phi_i)}{c}\right) - B\left(x + \frac{v_A(\phi_i)}{c} - \frac{v_B(\phi_i)}{c}\right) - C\left(x + \frac{v_A(\phi_i)}{c} - \frac{v_C(\phi_i)}{c}\right)\right]$$

$$B(x) = \frac{1}{n}\sum_{i=1}^{n}\left[S_i\left(x + \frac{v_B(\phi_i)}{c}\right) - C\left(x + \frac{v_B(\phi_i)}{c} - \frac{v_C(\phi_i)}{c}\right) - A\left(x + \frac{v_B(\phi_i)}{c} - \frac{v_A(\phi_i)}{c}\right)\right]$$

and

$$C(x) = \frac{1}{n}\sum_{i=1}^{n}\left[S_i\left(x + \frac{v_C(\phi_i)}{c}\right) - A\left(x + \frac{v_C(\phi_i)}{c} - \frac{v_A(\phi_i)}{c}\right) - B\left(x + \frac{v_C(\phi_i)}{c} - \frac{v_B(\phi_i)}{c}\right)\right]$$

similarly to the case of a binary system.

2.1.2 Limitations

Unfortunately, as for any disentangling method, the technique that we described in the previous section also has its limitations (González & Levato 2006).

First of all, the quality of the results strongly depends on the RV range covered by the observations. Moreover, the heavily blended spectra are more difficult to disentangle than less blended ones. It is thus very important to cover a significant fraction of the orbital cycle observationally, especially around the quadrature phases, where the lines associated to the two components are least blended. This will cause us some problems in the specific case of the triple systems studied in this thesis work, as we will further develop in Sect. 3.4 and Sect. 3.5. And, as we have mentioned earlier, the convergence of the algorithm is also dependent on the number of observations, that should thus be sufficiently high.

Secondly, small residual errors in the normalization of the input spectra can lead to oscillations of the continuum in the resulting separated spectra on wavelength scales of several dozen Å.

Moreover, the different spatial frequencies in the spectra are not recovered with the same precision: broad spectral features are not recovered as accurately as narrow ones. In practice, features wider than a few times the RV amplitude are barely recovered.

Concerning the calculation of the RVs, the most serious problem arises when the amplitude of the RV curve is comparable to the width of the spectral lines in the observed spectra. In practice, good convergence of RVs is obtained when the maximum RV difference between the components is at least the same order as the FWHM of the spectral lines.

Finally, in the specific case of interacting-wind binaries, some emission lines present in the observations may be partly due to the wind-wind interaction zone. This will make it difficult to recover properly the spectra, since the flux of the lines formed in the wind interaction zone will be erroneously assigned to the two components.

2.2 CMFGEN

2.2.1 The code

To constrain the fundamental parameters of the stars within the studied systems, we used the model atmosphere code CMFGEN (Hillier & Miller 1998). This is a radiative transfer code designed to solve the radiative transfer and statistical equilibrium equations in the co-moving frame in plane-parallel or spherical geometry for the cases of Wolf-Rayet and O-type stars, Luminous Blue Variables and supernovae. To facilitate the iterative simultaneous solution of these equations, a partial linearization method is used.

The CMFGEN code produces non-LTE[1] line-blanketed models that include the effects of stellar winds. Indeed, these three characteristics are essential for the modelling of massive hot stars. First, on the contrary of cooler stars, the LTE approximation is not appropriate for early-type stars, since the radiation field is sufficiently strong so that the radiative processes dominate over the collisional processes. In addition, the strong stellar winds of O and WR stars induce a strongly extended and permanently expanding stellar atmosphere. For those stars, the radiative transfer thus cannot be treated with the plane-parallel approximation: the spherical geometry of the atmospheres must be taken into account within the equations, together with the expanding motion. Finally, to determine reliable stellar parameters, it is essential to include the effect of blanketing due to the numerous overlapping lines of many chemical species, and particularly the heavy elements. Indeed, this blanketing acts as a "screen" which blocks the radiation, back-scattering the photons towards the in-

---

[1] LTE = Local Thermodynamic Equilibrium.

ner part of the atmosphere, thus increasing the local temperature and the degree of ionization of this region. This back-warming effect implies that for a given spectral classification the line-blanketed model requires a lower effective temperature to reach the same ionization. In addition, this screen also has the effect of reducing the ionization in the outer layers of the stellar atmosphere.

However, the inclusion of line-blanketing in the models makes the number of statistical equilibrium equations quite large. To reduce this number, and improve the accuracy of the models, Hillier & Miller (1998) introduced the idea of super levels, first proposed by Anderson (1989). In their approach, the levels of similar excitation energies and properties are grouped together and treated as a unique level in the statistical equilibrium equations. Within a given group, they assume identical departure coefficients, and only the population of the super level needs to be explicitly solved in order to fully specify the populations of the independent levels. This approach allows a lot of flexibility, since the number of super levels and their links to real atomic levels are easily modified, and it is thus easily possible to test the accuracy associated with various super-level assignments. Moreover, it permits to recover exactly the LTE conditions in the deeper layers.

The hydrodynamical structure (density, velocity) is given as an input to the code, the velocity structure being constructed from a combination of an inner structure and a β velocity law in the outer parts of the atmosphere. The radiative equilibrium is assumed in order to determine the temperature structure from the equation of energy conservation throughout the atmosphere. When the level populations have converged, the radiative force is calculated and a new approximation of the inner structure is computed and connected to the same β velocity law. The radiative field and level populations are then re-computed until the full convergence of the model is achieved. We usually performed three of these hydrodynamical iterations at the beginning of our modelling, resulting in a self-consistent hydrodynamical structure. The density structure is obtained from the mass conservation equation.

CMFGEN also needs numerous input data to compute a given model:

1. The stellar parameters: The effective temperature (T_{eff}), surface gravity ($\log g$), the luminosity (L), the radius (R), the mass (M), and the chemical abundances. In our computations, we included the following elements: H, He, C, N, O, Ne, Si, S, Ar, Ca, Fe, and Ni.

2. The wind parameters: The mass-loss rate ($\dot{M}$), the terminal velocity (v_∞), and the clumping factors (f_1 and f_2).

3. Some "environment" parameters, such as the input velocity structure, the extension of the atmosphere, the number of depth points, the chemical species and ionization stages, the levels/superlevels for each element.

The emergent spectrum is then computed using the code CMF_FLUX (Busche & Hillier 2005), in which is included a depth-dependent microturbulent velocity, varying from 10-20 km s^{-1} in the deeper layers to 10% of the terminal velocity of a given model in the upper wind. This spectrum is convolved with the appropriate rotational and macroturbulent velocities, and compared to the observations of a given star. This comparison permits to iteratively constrain the fundamental parameters of this star.

2.2.2 Main diagnostics for the modelling

In the present thesis work, we mainly analysed optical spectra of the studied stars, and we will thus focus on optical diagnostics for the stellar parameters in the present section. However, it is important to note that there are also numerous diagnostic features in the UV and IR regions of a spectrum. For a more complete review of the UV, optical and near-IR diagnostics of massive stars, see Martins (2011).

For our study of O-type stars, we relied on the following indicators to fit the observed spectra and constrain the fundamental stellar properties:

- Rotational velocity: The $v \sin i$ were obtained by applying a Fourier transform method (Simón-Díaz & Herrero 2007; Gray 2008) to the profiles of reference lines. The main lines we used are He I $\lambda\lambda$ 4026, 4922, 5016, O III λ 5592, and C IV λ 5812. We selected these lines because they are well isolated in the spectra and are therefore expected to be free of blends. Metallic lines, such as O III λ 5592, should be used as main indicators. When available, the following lines can also be used: C IV λ 5802 or He I λ 4713. The best estimate of the projected rotational velocity is obtained from the position of the first “zero” of the Fourier transform. The synthetic spectra computed by CMFGEN are convolved by a rotational profile corresponding to our value of $v \sin i$. For the specific case of LSS 3074 (see Sect. 3.3), the poor quality of the recovered spectra made it impossible to use these reference lines, and we had to use less ideal lines for the determination of the projected rotational velocities of the components: He I λ 4471, He II $\lambda\lambda$ 4200, 4542, 6118 and N III λ 6075 lines for the primary star of the system, and He II λ 5412 and Si IV λ 4089 lines for the secondary star.

- Macroturbulent velocity: The macroturbulence is defined as a non-thermal motion in the stellar atmosphere for which the size of the turbulent cells is greater than the mean free-path of the photons. This turbulence has for main effect to add a broadening component to the spectral lines. A first approximation of this velocity can be obtained by using the auxiliary program MACTURB of the stellar spectral synthesis program SPECTRUM v2.76 developed by Gray (2010), which is based on the radial-tangential anisotropic macroturbulent broadening formulation of Gray (2008). The main diagnostic lines for the determination of the macroturbulence velocity are O III λ 5592 and He I λ 4713 but we can also use the wings of stronger lines, such as He I $\lambda\lambda$ 4026, 4471, 5016, and He II λ 4542. Typical uncertainties on these velocities are $\sim$10 km s^{-1}.

- Effective temperature: The effective temperature is usually constrained by comparing the lines of ions of the same element but of different ionization states. The classical diagnostic is the ratio between the He I λ 4471 and He II λ 4542 lines, but complementary lines of helium can also be used, such as He I $\lambda\lambda$ 4026, 4389, 4713, 5876, and He II $\lambda\lambda$ 4200 and 5412. The temperatures derived with CMFGEN from a comparison with optical spectra have typical uncertainties of 500 to 2000 K, depending on the quality of the observations and on the effective temperature itself.

- Surface gravity: The $\log g$ is generally constrained from the widths of the Balmer lines. However, Hα is usually not used for constraining this parameter, since this particular line is highly influenced by numerous stellar wind parameters. Moreover, as we have seen in Sect. 2.1.2, the wings of broad lines are not as accurately recovered by the disentangling as narrower features. We have thus constrained the surface gravities, together with the stellar luminosities, by comparing the spectroscopic mass ratio to the dynamical mass ratio obtained in the orbital solutions of our systems, as fully explained in Raucq et al. (2016), Sect. 3.2 of the present work. The typical uncertainties that we obtained on the $\log g$ are 0.15-0.20 dex.

- Mass-loss rate: In the optical domain, the main diagnostic lines to constrain the mass-loss rate are Hα and He II λ 4686 (Puls et al. 1996). The strengths of H$_\gamma$ and H$_\delta$ can also be taken as secondary indicators, and are less sensitive to other wind parameters. We thus mainly worked with the latter secondary diagnostics. However, they can be affected by emission from the wind-wind collision zone in close massive binaries, and in those cases the obtained value of the mass-loss rate can only be considered as an upper limit.

- Terminal velocity: The terminal velocity v_∞ is the velocity reached by the stellar winds at a very large distance from the star. The main diagnostics on this parameters are in the UV field, making its determination with optical spectra rather difficult. The only hint for a first approximation of this parameters in the optical field is through the strength of the Hα line. For a given mass-loss rate, a larger terminal velocity will reduce the wind density and hence lower the emission in this line. However, since the Hα line is also strongly affected by other wind parameters, and by possible emission in the wind-wind interaction zone in close massive binaries, the determined v_∞ is rather uncertain and can only be considered as a lower limit.

- Clumping: Previous studies have shown that the winds of O stars are not homogeneous (see, e.g., Eversberg et al. 1998 for observational evidence and Bouret et al. 2005 for hints from atmosphere modelling). The clumping formalism used in our CMFGEN models is

  $$f(r) = f_1 + (1{-}f_1)e^{(-\frac{V(r)}{f_2})}$$

  with a clumping filling factor f_1 , a clumping velocity factor f_2 and $V(r)$ the velocity of the wind. The clumping filling factor represents the maximum clumping at the top of the atmosphere and the clumping velocity is a parameter indicating the position in the velocity field where the wind starts to be significantly clumped. The function $f\,(r)$ thus represents the volume filling factor of the wind by the clumps, assuming an empty interclump medium. These two clumping factors can be slightly adjusted through the strength and the shape of Hα and Hβ lines.

Finally, once the fundamental properties of the stars have been established, we can investigate the CNO abundances within their atmosphere, through the strengths of associated lines. We ran several models changing only these abundances, and then performed a χ^2 analysis to determine the ones giving the best fit to selected lines, and the associated uncertainties. For each element, we normalized the χ^2 function by its minimum $\chi^{\mathbf{2}}{}_{min}$. As a 1-$\sigma$ uncertainty on the abundances, we then considered abundances up to a normalized χ^2 of 2.0, i.e. an approximation for 1 over $\chi^{\mathbf{2}}{}_{\mathrm{min}}$, as suggested by Martins et al. (2015). We selected the diagnostic lines among the following lists, depending on the quality of the spectra and on the spectral type:

- Carbon abundance: C III λλ 4068-70, 4156, 4163, 4187 and 5826. One to five lines were used, except in the specific case of LSS 3074, see Raucq al. (2017), in Sect. 3.3 of the present work.
- Nitrogen abundance: N II λλ 4004, 4379, and 5026, N III λλ 4511, 4515, 4518, 4525, 4530, and 4535. Four to seven lines were used.
- Oxygen abundance: O III λλ 5508 and 5592. The only system for which we did not use the two lines was the specific case of LSS 3074, see Raucq al. (2017), in Sect. 3.3 of the present work.

For cooler spectral types, Martins et al. (2015) propose numerous other lines to complement the study of surface abundances.

Chapter 3

Studied systems

3.1 Our sample of targets

We can find in the literature a significant number of (post-)RLOF massive binaries candidates. Indeed, previous studies have efficiently shown the existence of binary interactions in close massive binaries, such as Plaskett's star (Linder et al. 2008). Nazé et al. (2017; and references therein) also listed a sample of 15 (post-)interacting massive binaries candidates, presented in Table 3.1.

In the context of this work, we have selected two systems showing strong hints of binary interactions: HD 149404, that shows strongly variable emission lines suggesting the presence of colliding winds and displays a secondary star presented in the literature as being enriched in nitrogen; and LSS 3074, that has a very short orbital period, a strong phase-locked variability of the emission lines, and for which previous studies reported unusually low minimum masses, considering the supergiant spectral types, which suggests that the system experienced a mass loss at some point. Note that Nazé et al. (2017) did not find any evidence of a magnetic field in any of these two systems.

To complement our study, we selected two other short-period massive multiple systems, HD 17505 and HD 206267, poorly studied in the literature, and searched for similar hints of binary interactions in their spectra, that may suggest that they experienced RLOF episodes.

Table 3.1: List of (post-)RLOF candidates proposed by Nazé et al. (2017).

HD ID	Other name	Spectral types	$P_{\rm orb}$ (days)	Hints of interaction	References
HD 1337	AO Cas	O9.7III + O9.5V	3.5	SD; PA	Stickland 1997; Linder et al. 2008
HD 25638	SZ Cam	O9.5V-9IV + B0-0.5V	2.7	PA	Lorenz et al. 1998; Harries et al. 1998 ; Tamajo et al. 2012; Gorda 2015, and references therein
HD 35652	IU Aur	O9.5V + B0.5IV-V	1.8	PA	Harries et al. 1998; Özdemir et al. 2003, and references therein
HD 35921	LY Aur	O9III + O9.5III	4.0	SD/OC; PA	Li & Leung 1985; Drechsel et al. 1989; Stickland et al. 1994; Mayer et al. 2013; Zhao et al. 2014, and references therein
HD 57060	29 CMa	O8.5I + O9.7V	4.4	SD/OC; PA; WW	Bagnuolo et al. 1994; Stickland 1997; Linder et al. 2008; Antokhina et al. 2011
HD 100213	TU Mus	O7.5V + O9.5V	1.4	C; PA	Linder et al. 2007; Qian et al. 2007; Penny et al. 2008, and references therein

The symbol "SD" stands for semi-detached configuration, while "C" and "OC" stand for contact and overcontact configurations. "PA" is used to point out the presence of anomalies in the stellar properties (either masses, radii, temperatures, luminosities and surface gravities) compared to the evolutionary models for single stars, and "AA" stands for surface abundances anomalies in at least one stellar atmosphere. Finally, we use the symbol "WW" to highlight the presence of a probable wind-wind collision zone in the systems.

Table 3.1: List of (post-)RLOF candidates proposed by Nazé et al. (2017). (continued)

HD ID	Other name	Spectral types	$P_{\rm orb}$ (days)	Hints of interaction	References
HD 106871	AB Cru	O8V + B0.5	3.4	SD; PA; AA	Lorenz et al. 1994
HD 115071		O9.5V + B0.2III	2.7	SD; PA	Penny et al. 2002, and references therein
HD 149404		O7.5If + ON9.7I	9.8	WW; AA; asynchronous rotation	Rauw et al. 2001; Thaller et al. 2001; Raucq et al. 2016
HD 152248		O7.5III(f) + O7III(f)	5.8	WW; C; PA	Sana et al. 2001, 2004; Mayer et al. 2008
HD 190967		O9.5V + B1I-II	6.5	SD; PA	Harries et al. 1997; Kumsiashvili et al. 2005
HD 209481	LZ Cep	O9III + ON9.7V	3.1	both stars almost fill their Roche lobes; AA; PA; slight asynchronicity	Harries et al. 1998; Mahy et al. 2011; Palate et al. 2013
HD 228854	V382 Cyg	O7.3V + O7.7V	1.9	SD/OC; PA	Harries et al. 1997; Degirmenci et al. 1999; Mayer et al. 2002; Qian et al. 2007; Yaşarsoy & Yakut 2013, and references therein
	LSS 3074	O5.5If + O6.5-7If	2.2	WW; low minimum masses	Niemela et al. 1992; Haefner et al. 1994; Raucq et al. 2017
	XZ Cep	O9.5V + B1III	5.1	SD; PA	Harries et al. 1997

3.2 HD 149404

HD 149404 is a detached, non eclipsing O-star binary situated in the Ara OB1 association, at a distance of 1.3 ± 0.1 kpc (Herbst & Havlen 1977). Rauw et al. (2001) have revised the orbital solution of this system and found an orbital period of 9.81 days and a circular orbit, with a probable inclination of 21°. This system displays two interesting hints of past or present binary interaction. Indeed, the spectrum of HD 149404 shows variable He II λ 4686 and Hα emission lines that are likely indicative of a wind-wind interaction (Rauw et al. 2001, Thaller et al. 2001, Nazé et al. 2002). Moreover, the secondary component of HD 149404 is found in the literature as being an ON star, suggesting a significant nitrogen enrichment of its atmosphere. These properties, together with the short orbital period of the system, make it a good candidate for our study of possible post-mass transfer objects.

Our investigation of HD 149404 is based on 17 échelle spectra previously used by Rauw et al. (2001). Five of these spectra were collected in May 1999 with the FEROS spectrograph mounted on the ESO 1.5 m telescope, and the remaining twelve spectra were collected in February 2000 with the Coralie spectrograph mounted on the 1.2 m Euler Swiss telescope located at La Silla (Chile).

We applied the disentangling technique described in Sect. 2.1 on these optical spectra to separate the contribution of both primary and secondary stars. The obtained reconstructed spectra then permitted us to determine accurately the spectral types of the components, revealing a system composed by an O7.5If primary and an ON9.7 secondary star. Since the disentangling method does not yield the brightness ratio of the components, we determined it by comparing the equivalent widths of a set of diagnostic lines for both stars to the mean equivalent widths of the same lines in synthetic spectra of stars of the same spectral type, and obtained a brightness ratio of $l_1/l_2 = 0.70 \pm 0.12$. We determined the projected rotational velocities of the stars by means of a Fourier Transform Method applied on selected isolated lines of the reconstructed spectra and obtained $v \sin i$ of 93 ± 8 and 63 ± 8 km s^{-1} for the primary and secondary respectively. The macroturbulence velocities were then estimated to be 70 and 80 km s^{-1} respectively.

We then fitted the individual reconstructed spectra with the CMFGEN atmosphere code (see Sect. 2.2) to constrain the stellar parameters of each star. This way, we obtained that the primary has a T_{eff} of 34 000 K and a $\log g$ of 3.55, and the secondary displays a T_{eff} of 28 000 K and a $\log g$ of 3.05.

To complement our study in the optical domain and check whether the CMFGEN models are also able to correctly reproduce the wind features, we investigated the UV field with a sample of 25 short-wavelength, high-resolution (SWP) *IUE* spectra of HD 149404 from the *IUE* archives. These spectra were described by Stickland & Koch (1996). The parts of the UV spectra that feature strong and broad wind lines cannot be properly recovered by the disentangling code (see Sect. 2.1.2). To circumvent this problem, we re-combined the synthetic CMFGEN UV spectra of the primary and secondary taking into account the radial velocity shifts at the time of the observations, for several orbital phases. We found good agreement between the obtained synthetic binary spectra and the observations.

This spectroscopic study of the binary system HD 149404 permitted us to highlight two hints of previous binary interaction. First, we confirmed the strong overabundance in nitrogen in the secondary atmosphere ($[\mathrm{N/C}]{\sim}150\,[\mathrm{N/C}]_{\odot}$), and a slight nitrogen overabundance in the primary atmosphere ($[\mathrm{N/C}]{\sim}5\,[\mathrm{N/C}]_{\odot}$). Second, we inferred an asynchronous rotation of the two stars, the primary displaying a rotational period of 3.77 ± 0.32 days and the secondary a period of 7.46 ± 0.95 days.

We conclude that the hypothesis of a past case A RLOF interaction in the system HD 149404 is the most plausible one to explain the current chemical surface abundances and rotational asynchronicity of the components, despite the fact that some of the observed properties challenge the current case A binary evolutionary models.

The full analysis of the HD 149404 binary system is published in Raucq et al. (2016, see paper hereafter).

A&A 588, A10 (2016)
DOI: 10.1051/0004-6361/201527543

Astronomy
&
Astrophysics

Observational signatures of past mass-exchange episodes in massive binaries: The case of HD 149 404[⋆,⋆⋆]

F. Raucq[1], G. Rauw[1], E. Gosset[1,⋆⋆⋆], Y. Nazé[1,⋆⋆⋆⋆], L. Mahy[1,†], A. Hervé[2], and F. Martins[3]

[1] Department of Astrophysics, Geophysics and Oceanography, Liège University, Quartier Agora, Allée du 6 Août 19c, Bat. B5c, 4000 Liège, Belgium
e-mail: `fraucq@doct.ulg.ac.be`
[2] Astronomical Institute of the Czech Academy of Sciences, Fričova 298, 251 65 Ondřejov, Czech Republic
[3] LUPM, Montpellier University 2, CNRS, place Eugène Bataillon, 34095 Montpellier, France

Received 12 October 2015 / Accepted 14 January 2016

ABSTRACT

Context. Mass and momentum exchanges in close massive binaries play an important role in their evolution, and produce several observational signatures such as asynchronous rotation and altered chemical compositions, that remain after the stars detach again.

Aims. We investigated these effects for the detached massive O-star binary HD 149 404 (O7.5 If + ON9.7 I, $P = 9.81$ days), which is thought to have experienced a past episode of case A Roche-lobe overflow (RLOF).

Methods. Using phase-resolved spectroscopy, we performed the disentangling of the optical spectra of the two stars. The reconstructed primary and secondary spectra were then analysed with the CMFGEN model atmosphere code to determine stellar parameters, such as the effective temperatures and surface gravities, and to constrain the chemical composition of the components. We complemented the optical study with the study of IUE spectra, which we compare to the synthetic binary spectra. The properties of the stars were compared to evolutionary models.

Results. We confirmed a strong overabundance in nitrogen ($[N/C] \sim 150\,[N/C]_\odot$) for the secondary and a slight nitrogen overabundance ($[N/C] \sim 5\,[N/C]_\odot$) for the primary star. Comparing the two stars, we found evidence for asynchronous rotation, with a rotational period ratio of 0.50 ± 0.11.

Conclusions. The hypothesis of a past case A RLOF interaction in HD 149 404 is most plausible to explain its chemical abundances and rotational asynchronicity. Some of the observed properties, such as the abundance pattern, are clearly a challenge for current case A binary evolution models, however.

Key words. stars: early-type – stars: fundamental parameters – binaries: spectroscopic – stars: individual: HD 149 404 – stars: massive

1. Introduction

As shown in recent studies (e.g. Sana et al. 2012), a large portion of massive stars belongs to binary or higher multiplicity systems. Whilst this multiplicity permits observationally determining the minimum masses of the stars through their orbital motion, it also leads to complications. For instance, the binarity of massive stars can result in interactions between their stellar winds that produce observational signatures throughout the electromagnetic spectrum (e.g. Rauw 2013). Moreover, during the lifetime of a massive binary, the binarity influences the evolution of the stars in various ways (e.g. Langer 2012). These evolutionary effects range from tidally induced rotational mixing (e.g. de Mink et al. 2009) over exchange of matter and angular momentum through a Roche lobe overflow (RLOF) interaction (e.g. Podsiadlowski et al. 1992; de Loore & Vanbeveren 1994; Wellstein et al. 2001; Hurley et al. 2002) to the merging of both stars (e.g. Podsiadlowski et al. 1992; Wellstein et al. 2001). In RLOF interactions, three different situations are distinguished: case A, for which the RLOF episode occurs when the mass-donor is on the core-hydrogen burning main-sequence; case B, when the star is in the hydrogen-shell burning phase; and case C, for which the star is in the helium-shell burning phase (Kippenhahn & Weigert 1967; Vanbeveren et al. 1998). These binary interactions significantly affect the physical properties of the components and their subsequent evolution. Despite considerable progresses in theoretical models, there remain a number of open questions such as the actual efficiency of accretion (e.g. Wellstein et al. 2001; de Mink et al. 2007; Dray & Tout 2007). To better understand this phenomenon, we need in-depth studies of systems undergoing or having undergone mass exchange.

In this context, HD 149 404 is an interesting target. It is a detached, non-eclipsing O-star binary, member of the Ara OB1 association, located at a distance of 1.3 ± 0.1 kpc (Herbst & Havlen 1977). The orbital parameters were revised by Rauw et al. (2001). These authors found an orbital period of 9.81 days and a circular orbit. They also estimated an orbital inclination of 21° by comparing "typical" masses of supergiants with similar spectral types to those of both components. The spectrum of HD 149 404 displays variable emission lines (He $\lambda\,4686$, Hα) that are likely indicative of a wind-wind interaction (Rauw et al. 2001; Thaller et al. 2001; Nazé et al. 2002). One of its components was assigned an ON spectral type, which suggests a significant nitrogen enrichment of its atmosphere.

In this study, we determine the fundamental parameters of the stars of this system through several analysis techniques. The data used in our study are presented in Sect. 2. In Sect. 3

[⋆] Based on observations collected at the European Southern Observatory (La Silla, Chile) and with the International Ultraviolet Explorer.

[⋆⋆] The reduced spectra are only available at the CDS via anonymous ftp to `cdsarc.u-strasbg.fr` (`130.79.128.5`) or via `http://cdsarc.u-strasbg.fr/viz-bin/qcat?J/A+A/588/A10`

[⋆⋆⋆] Senior Research Associate F.R.S-FNRS.

[⋆⋆⋆⋆] Research Associate F.R.S-FNRS.

[†] Postdoctoral Researcher F.R.S-FNRS.

we present the preparatory treatment of our data, which included disentangling the spectra of the binary system to reconstruct individual spectra of the binary components, which are needed for the subsequent spectral analysis. The spectral analyses were made with the non-LTE model atmosphere code CMFGEN and are presented in Sect. 4. In Sect. 5 we discuss the evolutionary state of HD 149 404 and compare it with similar systems.

2. Observational data

The optical spectra analysed here are the échelle spectra used by Rauw et al. (2001) in their study of the orbital solution and wind interactions of HD 149 404. These data were collected in May 1999 and February 2000 with the FEROS and Coralie spectrographs mounted on the ESO 1.5 m telescope and 1.2 m Euler Swiss telescope at La Silla, respectively. The FEROS and Coralie spectrographs have resolving powers of 48 000 and 50 000 and cover the wavelength ranges 3650–9200 Å and 3875–6800 Å, respectively. Further details on the instrumentation and the data reduction are given by Rauw et al. (2001). Because of some problems with the extraction of the FEROS data of May 2000, the normalization of the latter was more uncertain, and we therefore excluded these data from the disentengling procedure, and thus from the further analysis.

To complement our optical data, we also retrieved 25 short-wavelength, high-resolution (SWP) IUE spectra of HD 149 404 from the IUE archives. These spectra were previously described by Stickland & Koch (1996).

Table 1 yields the journal of observations along with the orbital phases computed according to the ephemerides of Rauw et al. (2001, their He λ 4471 orbital solution). The optical spectra provide a good sampling of the orbital cycle, which is important for the disentangling in Sect. 3.

Table 1. Journal of the optical (*top*) and UV (*bottom*) spectra.

Optical spectroscopy		
HJD-2 450 000	Inst.	ϕ
1299.796	FEROS	0.24
1300.788	FEROS	0.34
1301.792	FEROS	0.45
1302.783	FEROS	0.55
1304.792	FEROS	0.75
1578.866	Coralie	0.68
1579.879	Coralie	0.78
1580.872	Coralie	0.88
1581.864	Coralie	0.98
1582.869	Coralie	0.09
1583.877	Coralie	0.19
1584.857	Coralie	0.29
1585.845	Coralie	0.39
1586.870	Coralie	0.49
1587.861	Coralie	0.59
1588.886	Coralie	0.70
1590.886	Coralie	0.90

IUE SWP spectroscopy			
JD-2 440 000	ϕ	JD-2 440 000	ϕ
3718.044	0.76	4450.176	0.35
3724.588	0.42	4460.090	0.36
3776.869	0.75	9564.333	0.42
3776.921	0.76	9565.329	0.52
3776.966	0.76	9817.595	0.23
3793.028	0.40	9818.630	0.33
3798.965	0.00	9840.402	0.55
3926.010	0.95	9910.425	0.68
4001.156	0.60	9911.396	0.78
4001.203	0.61	9912.400	0.88
4120.089	0.72	9913.396	0.99
4129.216	0.65	9915.391	0.19
4412.327	0.50		

3. Preparatory analysis

3.1. Spectral disentangling

The previous determination of the orbital solution of the system performed by Rauw et al. (2001) allowed us to recover the individual spectra of both components by separating the normalized spectra of the binary system. For this purpose, we used our disentangling routine (Rauw 2007), which is based on the method of González & Levato (2006) and was previously used by Linder et al. (2008) and improved by Mahy et al. (2012). The basic idea behind this technique is that the most natural way to handle spectra for radial velocity measurements is to express them as a function of $x = \ln \lambda$ instead of as a function of λ. In this way, the Doppler shift for a line of rest wavelength λ_0 can be expressed as

$$\begin{aligned} \ln \lambda &= \ln \left[\lambda_0 \left(1 + \frac{v}{c} \right) \right] \\ &= \ln \lambda_0 + \ln \left(1 + \frac{v}{c} \right) \\ &\simeq \ln \lambda_0 + \frac{v}{c} \\ \Rightarrow x &\simeq x_0 + \frac{v}{c}\cdot \end{aligned}$$

Let $A(x)$ and $B(x)$ be the spectra of the primary and secondary in the heliocentric frame of reference. In the absence of line profile variability and eclipses, the spectrum observed at any phase ϕ can be written as

$$S(x) = A\left(x - \frac{v_\mathrm{A}(\phi)}{c}\right) + B\left(x - \frac{v_\mathrm{B}(\phi)}{c}\right),$$

where $v_\mathrm{A}(\phi)$ and $v_\mathrm{B}(\phi)$ are the radial velocities of stars A and B at orbital phase ϕ.

For a total of n observed spectra, the spectrum of the primary can be computed as the average of the observed spectra from which the secondary spectrum shifted by the appropriate radial velocity (RV) has been subtracted (González & Levato 2006) :

$$A(x) = \frac{1}{n} \sum_{i=1}^{n} \left[S_i \left(x + \frac{v_\mathrm{A}(\phi_i)}{c} \right) - B \left(x - \frac{v_\mathrm{B}(\phi_i)}{c} + \frac{v_\mathrm{A}(\phi_i)}{c} \right) \right]\cdot$$

And similarly for the secondary:

$$B(x) = \frac{1}{n} \sum_{i=1}^{n} \left[S_i \left(x + \frac{v_\mathrm{B}(\phi_i)}{c} \right) - A \left(x - \frac{v_\mathrm{A}(\phi_i)}{c} + \frac{v_\mathrm{B}(\phi_i)}{c} \right) \right].$$

Starting from an initial approximation for $B(x)$ (a flat spectrum), $v_\mathrm{A}(\phi_i)$ and $v_\mathrm{B}(\phi_i)$, we then iteratively determined the primary and secondary spectra and their radial velocities (see González & Levato 2006). For the separations we performed here, we fixed the radial velocities of the binary components to those corresponding to the orbital solution of Rauw et al. (2001).

As for any disentangling method, this technique also has its limitations (González & Levato 2006). A reasonable observational sampling of the orbital cycle is needed because the quality of the results depends on the radial velocity (RV) ranges covered by these observations. Another important limitation is that broad spectral features are not recovered with the same accuracy as narrow ones. This is the case for the wings of the Balmer

Table 2. Brightness ratio determination from the dilution of prominent lines.

Line	Equivalent width (Å)						l_1/l_2
	Observations		Synthetic spectra		Conti (1973, 1974)		
	Primary	Secondary	O7.5	O9.7	O7.5	O9.5	
He I λ 4026	0.19	0.34	0.72	0.74	0.65	0.80	0.57
Si IV λ 4089	0.12	0.34	0.32	0.56	0.25	0.53	0.61
Si IV λ 4116	0.06	0.24	0.11	0.29	0.12	0.37	0.66
He II λ 4200	0.11	0.08	0.47	0.21	0.42	0.23	0.61
Hγ	0.45	0.50	1.77	1.74	1.88	2.09	0.88
He I λ 4471	0.17	0.37	0.55	0.69	0.71	0.97	0.58
He II λ 4542	0.17	0.07	0.53	0.21	0.64	0.25	0.96

Notes. The measured EWs are compared with values for the same lines in synthetic spectra of the same spectral type and in the compilation of measurements from the literature. The last column yields the brightness ratio for each line considered, using the synthetic spectra EWs.

lines, but it also holds for the UV features that arise in the stellar winds, such as P-Cygni profiles. For instance, for the IUE spectra of HD 149 404, the Si IV λ 1393-1403 and N IV λ 1718 P-Cygni lines are very broad and barely vary during the orbital cycle. It was therefore impossible to properly separate the primary and secondary contributions for these lines. In practice, features that are wider than a few times the RV amplitude are barely recovered. Moreover, small residual errors in the normalization of the input spectra can lead to oscillations of the continuum in the resulting separated spectra on wavelength scales of several dozen Å. Finally, spectral disentangling works on continuum-normalized spectra and does not yield the brightness ratio of the stars, which must be determined by other techniques (see below).

Finally, in the specific case of HD 149404, several emission lines (Hα and He II λ 4686, for example) do not seem to arise in the atmosphere of either component, but are formed at least partly in the wind-wind interaction zone (Rauw et al. 2001; Thaller et al. 2001; Nazé et al. 2002). As a result, the disentangling code is unable to meaningfully reconstruct these lines in the spectra of the components. We need to keep this in mind when analysing the reconstructed spectra.

3.2. Spectral types

Based on the reconstructed individual line spectra of the primary and secondary components, we determined the spectral types of the stars by measuring the equivalent width ratio of the spectral lines He I λ 4471 and He II λ 4542 on the one hand, and Si IV λ 4088 and He I λ 4143, on the other hand. We applied Conti's quantitative classification criteria for O-type stars (Conti & Alschuler 1971; Conti & Frost 1977; see also van der Hucht 1996) for both spectral types and luminosity classes to determine that the primary star is an O7.5 If star, while the secondary is an ON9.7 I[1]. Since our classification is based on the separated spectra, it is less sensitive to a possible phase-dependence of the line strengths and should thus be more robust than a classification based on spectra that are only collected near quadrature phase, as done by Rauw et al. (2001). However, in this particular case, we find an excellent agreement with the classification (O7.5 I(f) + ON9.7 I) proposed by these authors.

3.3. Brightness ratio

Spectral disentangling yields the strength of the lines in the primary and secondary stars relative to the combined continuum, but does not allow establishing the relative strengths of the continua. To further analyse the separated spectra, we therefore need to first establish the brightness ratio of the stars.

To estimate the optical brightness ratio of the components of HD 149404, we measured the equivalent widths of a number of spectral lines on the separated spectra of the primary and secondary, but referring to the combined continuum of the two stars. The results are listed in Table 2 along with the mean equivalent widths of the same lines in synthetic spectra of stars of the same spectral type, computed with the non-LTE model atmosphere code CMFGEN (Hillier & Miller 1998), which we describe in Sect. 4.2. For comparison, we also list the mean equivalent widths of the same lines in spectra of stars of the same spectral type as evaluated from the measurements of Conti (1973, 1974) and Conti & Alschuler (1971).

The brightness ratio of the two stars can then be evaluated from

$$\frac{l_1}{l_2} = \left(\frac{EW_1}{EW_2}\right)_{\rm obs} \left(\frac{EW_{O9.7}}{EW_{O7.5}}\right)_{\rm mean}.$$

By combining our measurements with those from synthetic spectra, we derive an optical brightness ratio of 0.70 ± 0.12 in this way, which is slightly lower than the value found by Rauw et al. (2001), who inferred 0.90 ± 0.16. As a consistency check, we also determined the brightness ratio by comparison with Conti's measurements and obtained 0.79 ± 0.13. The difference between the results obtained based on synthetic spectra versus Conti's measurements arises at least partially because Conti (1973, 1974) did not take into account the spectral type O9.7, but instead considered an O9.5 spectral type, consisting of both classes of stars currently known as O9.5 and O9.7.

Reed (2003) reported a mean V magnitude of 5.48 ± 0.02 and $B - V$ colour of 0.39 ± 0.02 for the system. Since the intrinsic $(B-V)_0$ of an O7.5 or O9.5 star is −0.26 (Martins & Plez 2006), the extinction A_V can be calculated as being 2.02 ± 0.06, assuming $R_V = 3.1$. Assuming the 1.3 ± 0.1 kpc distance (Wolk et al. 2008), we infer an absolute $M_V = -7.11 \pm 0.07$ for the binary. A brightness ratio of $l_1/l_2 = 0.70 \pm 0.12$ then yields individual absolute magnitudes of $M_V^P = -6.15 \pm 0.13$ and $M_V^S = -6.53 \pm 0.10$.

The separated continuum-normalized primary and secondary optical spectra are shown and analysed in Fig. 1, in Sect. 4.4.

---

[1] In the literature on interacting binaries, the terminologies "primary" and "secondary" usually designate the initially more massive star and less massive star, respectively. However, in accordance with previous studies of the HD 149 404 system, in the present paper the terms "primary" and "secondary" star refer to the currently more massive and less massive component, respectively.

Table 3. Projected rotational velocities ($v \sin i$ in km s^{-1}) of the components of HD 149 404.

Line	Primary	Secondary
He I λ4026	97	75
He I λ4922	94	64
He I λ5016	105	58
O III λ5592	87	55
C IV λ5812	82	–
Mean value	93 ± 8	63 ± 8

4. Spectral analysis

4.1. Rotational velocities and macroturbulence

After applying a Fourier transform method (Simón-Díaz & Herrero 2007; Gray 2008) to the profiles of the He I $\lambda\lambda$4026, 4922, 5016, O III λ5592, and C IV λ 5812 lines of the separated spectra, we determined the projected rotational velocities $v \sin i$ of the stars of the system. We selected these lines because they are very well isolated in the spectra and are therefore expected to be free of blends. The results are presented in Table 3. The mean $v \sin i$ of the primary star is (93 ± 8) km s^{-1}, while that of the secondary is (63 ± 8) km s^{-1}.

Macroturbulence is defined as a non-thermal motion in the stellar atmosphere in which the size of the turbulent cell is greater than the mean free-path of the photons. The main effect of the macroturbulence is an additional broadening of the spectral lines. This effect has received much attention over recent years (e.g. Simón-Díaz & Herrero 2014). A first approximation of the macroturbulence velocities is obtained by applying the radial-tangential anisotropic macroturbulent broadening formulation of Gray (2008) on the spectra after including rotational velocity broadening. We used the auxiliary program MACTURB of the stellar spectral synthesis program SPECTRUM v2.76 developed by Gray (2010). We applied this technique to the lines He I $\lambda\lambda$ 4026, 4471, and 5016, and He II λ 4542. In this way, we obtained macroturbulence velocities of 70 and 80 km s^{-1} for the primary and secondary stars, respectively. Although this is quite high, these numbers are consistent with measurements of Simón-Díaz & Herrero (2014) that were made on stars of similar spectral types.

Both rotational and macroturbulence velocities were applied on the synthetic spectra (see Sect. 4.2) before comparing the latter with the separated spectra.

4.2. CMFGEN code

To determine the fundamental properties of the components of HD 149 404, we used the non-LTE model atmosphere code CMFGEN (Hillier & Miller 1998). This code solves the equations of radiative transfer and statistical equilibrium in the co-moving frame for plane-parallel or spherical geometries for Wolf-Rayet stars, O stars, luminous blue variables, and supernovae. CMFGEN furthermore accounts for line blanketing and its effect on the energy distribution. The hydrodynamical structure of the stellar atmosphere is specified as an input to CMFGEN. For the stellar wind, a β law is used to describe the velocity law. In the resolution of the equations of statistical equilibrium, a super-level approach is adopted. The following chemical elements and their ions are included in the calculations: H, He, C, N, O, Ne, Mg, Al, Si, S, Ca, Fe, and Ni. The solution of the equations of statistical equilibrium is used to compute a new photospheric structure, which is then connected to the same β wind velocity law. The radiative transfer equations are solved based on the structure of the atmosphere, with a microturbulent velocity varying linearly with velocity from 10 km s^{-1} in the photosphere to $0.1 \times v_\infty$ at the outer boundary, and generated synthetic spectra are compared to the separated spectra.

As a first approximation, we assumed that gravity, stellar mass, radius, and luminosity are either assumed equal to typical values of stars of the same spectral type (Martins et al. 2005) or adopted from the study of Rauw et al. (2001). The mass-loss rates and β parameters were taken from Muijres et al. (2012) for the spectral types of both stars, whilst the wind terminal velocity was set equal to 2450 km s^{-1} (Howarth et al. 1997) for the two components.

The relevant parameters were then adjusted by an iterative process because each adjustment of a given parameter leads to some modifications in the value of others. This process and the results we obtained are presented in Sects. 4.3 and 4.4.

4.3. Method

The first step was to adjust the temperature in the stellar models. The temperatures were mostly determined through the relative strengths of the He I λ4471 and He II λ4542 lines (Martins 2011). The final values are 34 000 and 28 000 K for the primary and secondary stars. Both results agree reasonably well with the temperatures expected for supergiants of these spectral types (Martins et al. 2005).

Subsequently, the natural steps to follow would be adjusting the surface gravities, the mass-loss rate, and the clumping factor, but the binarity of the studied system causes some problems. Indeed, since the wings of broad lines are not properly restored by the disentangling, it is impossible to use the Balmer lines to constrain the surface gravity. And since the Hα and Hβ lines are in addition strongly affected by extra emission from the wind-wind interaction (Rauw et al. 2001; Thaller et al. 2001; Nazé et al. 2002), they cannot be used as diagnostics of the mass-loss rate and clumping factor. The mass-loss rates were therefore fixed to the values tabulated by Muijres et al. (2012) for stars of the same spectral type (see their Table 1, method A). The clumping formalism used in the CMFGEN model is

$$f(r) = f_1 + (1 - f_1)e^{(-\frac{V(r)}{f_2})}$$

with a filling factor f_1 of 0.1, a clumping velocity factor f_2 of 100 km s^{-1} , and $V(r)$ the velocity of the wind.

We used an iterative process to constrain the luminosities and surface gravities. The first estimate of $\log(g)$ was taken from Martins et al. (2005) following the spectral types of the stars. Combined with our determination of the effective temperatures, we then inferred the bolometric corrections (Lanz & Hubeny 2003). This in turn yielded the individual bolometric luminosities, using the absolute V magnitudes of the components derived in Sect. 3.3.

These bolometric luminosities and the effective temperatures were used to compute the ratio of the stellar radii $\frac{R_P}{R_S}$. Together with the assumed gravities, this ratio yields the spectroscopic mass ratio $\frac{M_P}{M_S}$, which was then compared to the dynamical mass ratio inferred from the orbital solution (Rauw et al. 2001). The difference in these mass ratios was used to produce a new estimate of the surface gravities, and this iterative process was repeated until the spectroscopic and dynamical mass ratios agreed with each other and the CMFGEN synthetic spectra produced for the new gravity values matched the observations as well as possible.

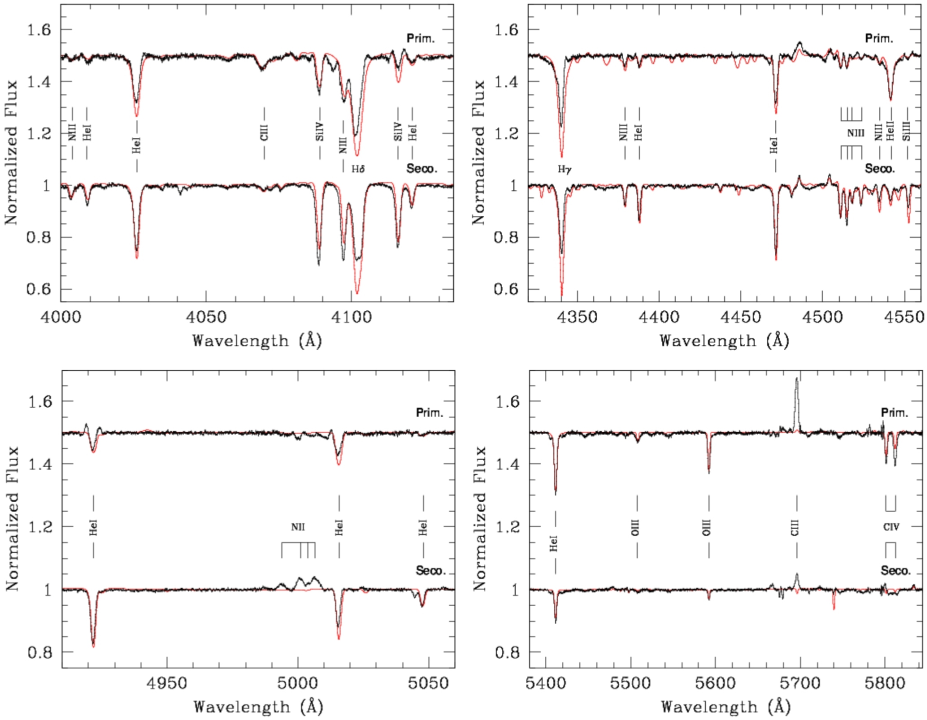

Fig. 1. Part of the normalized separated spectra of the primary (*top*, shifted upwards by 0.5 continuum units) and secondary stars (*bottom*), along with the best-fit CMFGEN model spectra (red).

After the fundamental stellar parameters were established or fixed, we investigated the CNO abundances through the strengths of the associated lines. We performed a normalized χ^2 analysis to determine the best fit to selected lines (Martins et al. 2015). The normalization consists in dividing the χ^2 by its value at minimum, $\chi^2_{\rm min}$. As a 1σ uncertainty on the abundances, we then considered abundances up to a χ^2 of 2.0, that is, an approximation for 1 over $\chi^2_{\rm min}$, as suggested by Martins et al. (2015). We used the C III $\lambda\lambda$4068-70, C II λ4267, C III λ5826, N III λ4004, N III $\lambda\lambda$4511-15-18-24, N II λ5026, O III λ5508, and O III λ5592 lines to adjust the C, N, and O abundances of the primary star. For the secondary star, the same lines were used for the N and O abundances, but the only line used for the C abundance was C III $\lambda\lambda$4068-70. Two methods were used to determine the χ^2 of each line. First, we compared the depth of the observed and synthetic line cores in the calculation. Second, we determined the mean χ^2 for every independent point of the full profile of each considered line. The two methods gave similar results. After testing the influence of the errors on projected rotational velocities on the determination of the surface abundances, we found that their effect was small compared to the 1σ uncertainties on the measured abundances as determined here above. We therefore neglected them.

4.4. Results

Figure 1 illustrates the best fit of the optical spectra of the primary and secondary stars obtained with CMFGEN. In Table 4 we present the stellar parameters determined compared to those derived by Rauw et al. (2001). In general, these two works agree well. Table 5 compares the chemical abundances of these best-fit models with solar abundances taken from Asplund et al. (2009).

Figure 1 shows that the He lines and the C III $\lambda\lambda$4068-70 lines are very well reproduced for both stars. The C III λ5696 line cannot be considered in the determination of the surface C abundance since its formation process depends on a number of fine details of atomic physics and of the modelling (Martins & Hillier 2012). Most of the N lines also are very well adjusted. The N II emission lines around 5000 Å in the primary spectrum may be due to emission in the interaction zone, as they are well present in the observed spectrum and not represented in the modelled spectrum. The case of oxygen is more problematic. Whilst O III λ5592 is well adjusted, several other O III lines are present in the synthetic CMFGEN spectra (e.g. O III $\lambda\lambda$ 4368, 4396, 4448, 4454, and 4458), but they are barely visible in the separated spectra. We checked that these lines are also absent from the original observed binary spectra. Their absence is thus by no means an artefact that is due to the treatment of our data.

Table 4. Stellar parameters of the primary and secondary stars as obtained with CMFGEN.

	This study		Rauw et al. (2001)	
	Prim.	Sec.	Prim.	Sec.
R ($R_\odot$)	19.3 ± 2.2	25.9 ± 3.4	24.3 ± 0.7	28.1 ± 0.7
M ($M_\odot$)	50.5 ± 20.1	31.9 ± 9.5	54.8 ± 4.6	33.0 ± 2.8
$T_{\rm eff}$ (10^4 K)	3.40 ± 0.15	2.80 ± 0.15	3.51 ± 0.1	3.05 ± 0.04
$\log\left(\frac{L}{L_\odot}\right)$	5.63 ± 0.05	5.58 ± 0.04	5.90 ± 0.08	5.78 ± 0.08
$\log g$ (cgs)	3.55 ± 0.15	3.05 ± 0.15		
β	1.03^f	1.08^f		
v_∞ (km s^{-1})	2450^f	2450^f		
$\dot{M}$ ($M_\odot$ yr^{-1})	$9.2 \times 10^{-7\,f}$	$3.3 \times 10^{-7\,f}$		
BC	−3.17	−2.67		

Notes. The best-fit CMFGEN model parameters are compared with the parameters obtained by Rauw et al. (2001) for an orbital inclination of 21°. The effective temperatures from Rauw et al. (2001) were derived through the effective temperature calibration of Chlebowski & Garmany (1991) and permitted, along with the determined luminosities, inferring the stellar radii. The quoted errors correspond to 1σ uncertainties. The symbol $^{(f)}$ in the table corresponds to values fixed from the literature (Howarth et al. 1997; Muijres et al. 2012). The bolometric corrections are taken from Lanz & Hubeny (2003), based on our best-fit $T_{\rm eff}$ and $\log g$.

Table 5. Chemical abundances of the components of HD 149 404.

	Primary	Secondary	Sun
He/H	0.1	0.1	0.089
C/H	$1.02^{+0.10}_{-0.11} \times 10^{-4}$	$1.89^{+0.47}_{-0.47} \times 10^{-5}$	2.69×10^{-4}
N/H	$1.32^{+0.20}_{-0.15} \times 10^{-4}$	$7.15^{+2.5}_{-1.8} \times 10^{-4}$	6.76×10^{-5}
O/H	$7.33^{+1.1}_{-1.1} \times 10^{-4}$	$7.85^{+1.8}_{-1.1} \times 10^{-5}$	4.90×10^{-4}

Notes. Abundances are given by number as obtained with CMFGEN. The solar abundances (Asplund et al. 2009) are quoted in the last column. The 1σ uncertainty on the abundances was set to abundances corresponding to a χ^2 of 2.0. As only one line was considered for the C abundance of the secondary, the corresponding calculated uncertainty was unrealistically low. A similar problem was encountered for the O abundance of the primary star, for which we only had two lines to work with and several absent lines over the spectrum, as specified in the second paragraph of this section. To circumvent these problems, we set the uncertainties for these two abundances to values close to those calculated for the other two elements of the corresponding star.

We stress two interesting results from our spectral analysis. First of all, we confirm the large overabundance of N in the secondary spectrum. Second, we infer an asynchronous rotation of the two stars. The radii determined with CMFGEN (Table 4), the mean projected rotational velocities (Table 1), and the inclination estimate from Rauw et al. (2001) yield the rotation periods of the primary and secondary stars: 3.77 ± 0.32 days and 7.46±0.95 days, respectively, or a period ratio of 0.50±0.11. We note that within the uncertainties on the inclination, the secondary rotational period is similar to the orbital period of the system (9.81 days).We return to these points in Sect. 5. Finally, we note that according to the radii determined here, none of the stars currently fills its Roche lobe. With the formula of Eggleton (1983), we estimate a Roche-lobe volume filling factor of 15% for the primary and 73% for the secondary.

As pointed out above, disentangling the IUE spectra of HD 149 404 was more problematic, especially for those parts of the UV spectra that feature strong and broad wind lines and/or are polluted by blends with numerous interstellar features. The left panel of Fig. 2 illustrates the comparison of the separated spectra and the synthetic spectra obtained with CMFGEN over a wavelength range that is relatively free of interstellar lines and mainly hosts photospheric lines. The agreement is clearly quite reasonable.

To check whether our CMFGEN models are also able to correctly reproduce the wind features, we re-combined the synthetic CMFGEN UV spectra of the primary and secondary taking into account the radial velocity shifts at the time of the observations. We did so for several orbital phases. The right panel of Fig. 2 illustrates the result for three selected IUE spectra (SWP03008, JD 2 443 798.965, SWP02755, JD 2 443 776.869, and SWP54350, JD 2 449 817.595), corresponding to conjunction phase 0.00 and quadrature phases 0.75 and 0.25. The synthetic spectrum clearly agrees well with the observation, except for a few narrow absorptions that are due to the interstellar medium, which are not taken into account in our model. This additionally supports our determination of the physical parameters of the system components. Moreover, the concordance between the synthetic and observed UV spectra suggests that the P-Cygni profiles form over parts of the stellar winds that are not significantly affected by the wind-wind interactions, the latter leading to a loss of spherical symmetry of the line formation region.

The fluxed CMFGEN spectra also allow us to estimate the brightness ratio (primary/secondary) in the UV. We find a value of 0.91[2].

Furthermore, we found relatively little variability of the P-Cygni profiles over the orbital period. Both observations (lack of strong variability and little effect of wind interaction on the line morphology) are likely due to the low orbital inclination ($i \sim 21°$) of the system. This inclination implies that the observed spectrum arises mostly at high stellar latitudes, where the wind-wind interaction zone has less influence on the wind structure.

5. Discussion and conclusion

5.1. Evolutionary status

As we have shown in the previous section, the spectra of the components of HD 149 404 display the signatures of some

---

[2] This result is at odds with the 0.7 mag difference (i.e. primary/secondary brightness ratio of 1.91) between the primary and secondary UV fluxes inferred by Howarth et al. (1997). This situation most likely stems from the differences in the spectral types adopted by Howarth et al. (1997), who classified the system as O8.5 I + O7 III, whilst we have derived O7.5 If + ON9.7 I. This difference in spectral types directly affects the strength of the cross-correlation peaks of the spectra of the two components with the template spectrum of τ Sco (B0.2 IV) and thus the correction on the magnitude difference inferred by Howarth et al. (1997).

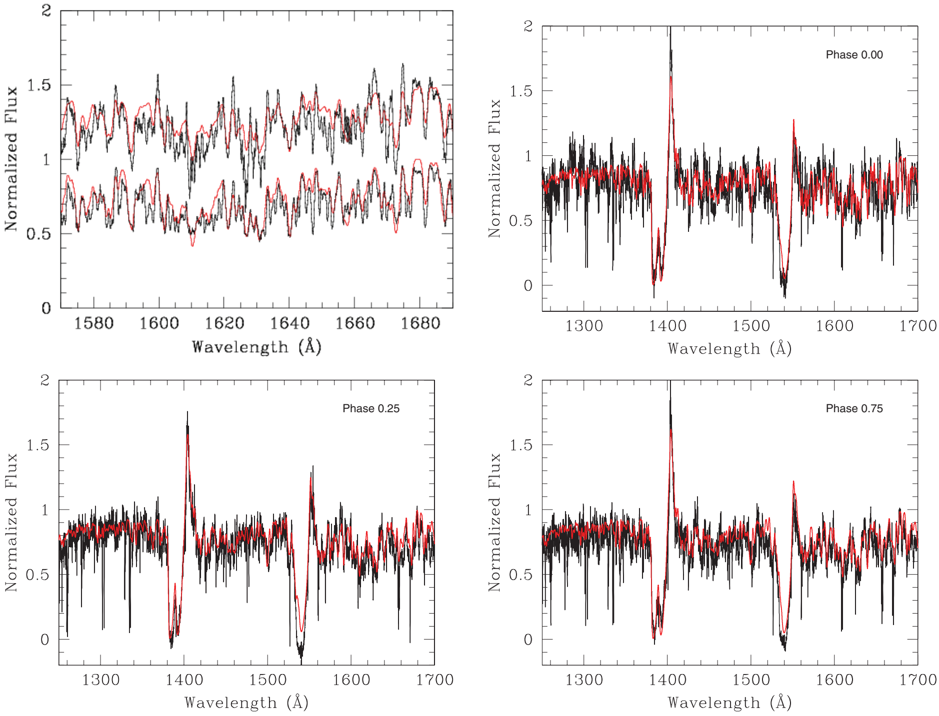

Fig. 2. *Upper left panel*: comparison between the separated IUE spectra (black) of the primary and secondary stars around the He λ 1640 line and the corresponding synthetic spectra (red). The primary spectrum is shifted upwards by 0.5 for clarity. *The other three panels* display a comparison between the SWP03008 (*upper right*), SWP54350 (*lower left*) and SWP02755 (*lower right*) IUE spectra taken at phases 0.0, 0.25 and 0.75 in black and the synthetic binary spectra obtained through combination of CMFGEN primary and secondary spectra at given phases in red.

enrichment by the products of stellar nucleosynthesis processes. These properties indicate a previous mass-exchange episode. Figure 3 compares our inferred N/C and N/O ratios with the predictions for the evolution of single massive stars (Ekström et al. 2012) either without rotation (left panel) or with a rotational velocity of 0.4 × $v_{\rm crit}$ (right panel). This figure clearly shows that for the spectroscopic masses of the primary and secondary stars these models cannot account for the observed CNO abundance patterns. For instance, in the case of models without rotation (left-hand panel of Fig. 3), no chemical enrichment is expected during the main-sequence evolution for stars with mass $<60\ M_\odot$. Only for the $M > 60\ M_\odot$ model is the loss of material through stellar wind sufficient to reveal the products of the CNO cycle at the surface before the end of the main-sequence evolution. Adopting instead the rotating models (right-hand panel of Fig. 3), the enrichment of the secondary can only be explained by single-star evolution if we assume at least a star with 60 $M_\odot$, whilst the spectroscopic mass is about a factor two lower. When the surface abundances of a single star of 60 $M_\odot$ initial mass reach the values observed for the secondary of HD 149 404, the current mass of the star is still about 50 $M_\odot$, that is, it is much higher than the mass determined for the secondary star.

The observed CNO abundance pattern is qualitatively much easier to interpret if the present-day secondary star was formerly the more massive component of the binary and transferred mass and angular momentum to the present-day primary in an RLOF episode. During this process, the outer envelope of the secondary was removed, revealing layers of material that were previously inside the convective hydrogen-burning core (Vanbeveren 1982, 2011).

We start by comparing our results with theoretical predictions from the literature. The expectation is that the more mass has been lost by the donor, the deeper the layers that are revealed at the surface and thus the higher the N/C ratio. The predicted CNO abundances for the mass loser after a case B mass-transfer episode are $[{\rm N/C}] = 100\ [{\rm N/C}]_\odot$ and $[{\rm N/O}] \geq 5\ [{\rm N/O}]_\odot$ (Vanbeveren 1982). This is indeed close to what we observe in our analysis. Moreover, the RLOF scenario is re-enforced by the values of the primary star abundances. Classical radiative equilibrium evolutionary models predict normal H and He abundances for the mass gainer of an RLOF episode, but an N abundance of two to three times solar (Vanbeveren & de Loore 1994), which agrees with our results.

There are some caveats here, however. First, the results of Vanbeveren (1982) apply to case B mass transfer, whereas HD 149 404 is more likely to have undergone a case A mass exchange (see below). Second, when the outer hydrogen-rich layers are removed, an enrichment of the stellar surface of the mass

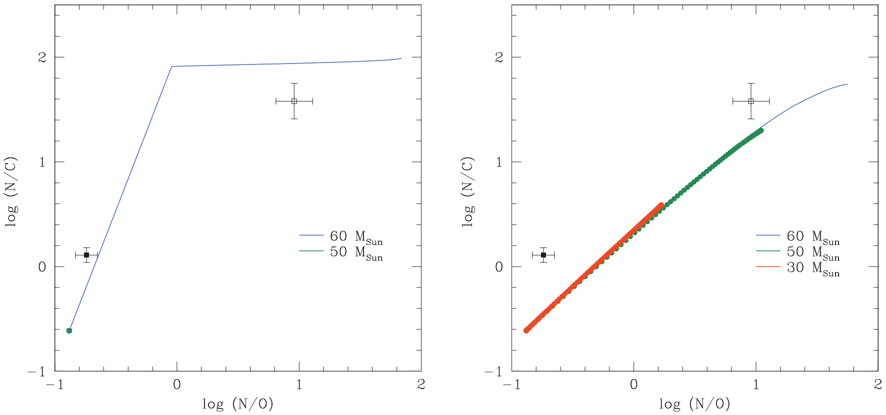

Fig. 3. Comparison of the N/C and N/O ratios determined from our spectral analyses with predictions from single-star evolutionary models of different masses (Ekström et al. 2012). The primary and secondary stars are shown by the open and filled square symbols, respectively. *The left panel* illustrates the results for core hydrogen-burning phase tracks without stellar rotation, whilst *the right panel* corresponds to the same tracks for stars rotating at $0.4 \times v_{\rm crit}$.

donor in helium is expected. Our spectral modelling was made with the He abundance set to solar, however, and there is no hint for our models requiring a He enhancement in any of the stars. Although the predicted relative change of helium surface abundance is usually much smaller than for N, this result is nonetheless surprising, especially in view of the large N overabundance of the secondary star.

To illustrate the helium enrichment that might be expected, we consider once more the single-star evolutionary tracks with rotation of Ekström et al. (2012). In these models, a nitrogen surface abundance similar to the one observed for the secondary is always accompanied by an increase of the surface helium abundance to values higher than $y = 0.35$ by mass. The fact that the spectrum of the secondary of HD 149 404 can be fit with a solar helium abundance ($y = 0.1$) suggests that the internal structure of the secondary before the onset of mass transfer must have been different from that expected from single-star evolutionary models. Moreover, the RLOF in HD 149 404 must have come to a (temporary) stop before the full hydrogen-rich envelope of the mass donor was removed. The latter conclusion is also supported by our finding that both stars are currently well inside their Roche lobes.

Given the present-day spectroscopic masses, the secondary must have lost at least 9.3 $M_\odot$ assuming a fully conservative mass transfer. Conservative RLOF will increase the period of the binary. If we assume a fully conservative mass transfer and apply the formula of Vanbeveren et al. (1998), we find that the orbital period would have increased by 17% at most, the shortest possible initial orbital period being 8.4 days for a mass exchange of 9.3 $M_\odot$. However, Petrovic et al. (2005) argued that in fast case A RLOF, only about 15–20% of the mass shed by the mass donor is indeed accreted by its companion. If the mass-transfer efficiency is that low, then the secondary must have lost a much larger amount of mass. Such a non-conservative mass transfer can result from the transfer of angular momentum. In fact, the mass gainer can be spun up to critical rotation and will then repel additional mass (and angular momentum), leading to a non-conservative mass transfer (e.g. Langer et al. 2003; Vanbeveren 2011; Langer 2012). In the previous section, we noted that the components of the system are apparently not in synchronous rotation. This asynchronicity therefore also suggests the existence of a past mass and angular momentum transfer episode, with a clear spin up of the primary star.

In Fig. 4 we present the positions of the primary and secondary stars in the Hertzsprung-Russell diagram (HRD) (upper panels) and in the $\log g$–$\log T_{\rm eff}$ diagram (lower panels), along with the evolutionary tracks from Ekström et al. (2012) for the core-hydrogen burning phase of single stars at solar metallicity, both for non-rotating (left panels) and rotating (right panels) stars. This figure again illustrates the failure of single-star evolutionary tracks to account for the properties of the components of HD 149 404. If we consider the models without rotational mixing, the position of the primary star in the HRD is relatively close to the track corresponding to its present-day spectroscopic mass. However, the secondary appears too luminous for its present-day mass compared to these evolutionary tracks. If we compare the stars to the 40% critical rotation case, we find that the primary's luminosity is below that expected for its present-day spectroscopic mass. Moreover, the secondary lies outside the range covered by tracks in the core-hydrogen burning phase. If we consider the non-rotating case, we see that in the $\log g$–$\log T_{\rm eff}$ diagram the primary star has a lower effective temperature and a higher surface gravity than expected for a 50 $M_\odot$ star, whilst the secondary star displays parameters corresponding to stars twice as massive as its present-day spectroscopic mass. For stars rotating at 40% of their critical velocity, we find that both stars would have initial masses of about 30 $M_\odot$. The primary dynamical mass is about a factor 2 higher, while for the secondary the agreement is good. Finally, in all cases (with and without rotation and for both diagrams), the two components of HD 149 404 are not located on the same isochrone, although they would be expected to have the same age[3].

In a mass-transfer episode, the location of both stars in the HRD after the RLOF strongly depends on the details of the process. For instance, spinning-up the mass gainer can lead to

---

[3] The age of the Ara OB1 association of which HD 149 404 is a member was estimated in the literature as ~3 Myr (Wolk et al. 2008).

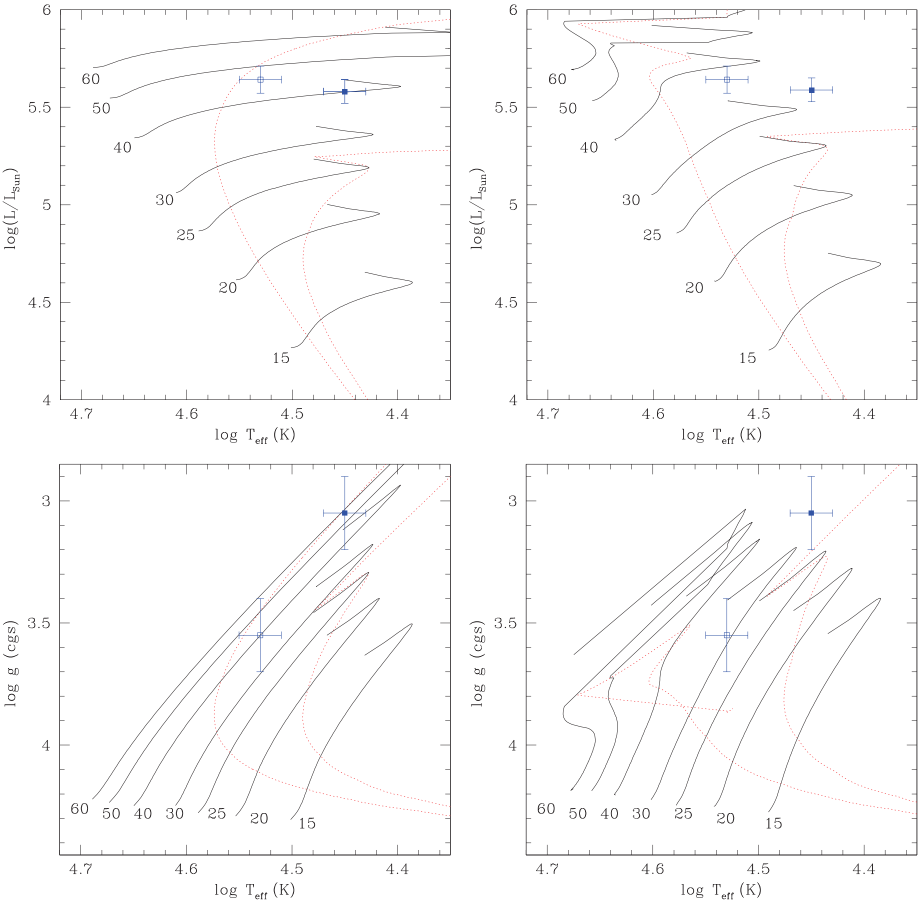

Fig. 4. Position of the primary (open square) and secondary (filled square) stars in the Hertzsprung-Russell diagram (*upper panels*) and the log g–log $T_{\rm eff}$ diagram (*lower panels*) along with evolutionary tracks for single massive stars at solar metallicity during the core-hydrogen burning phase (Ekström et al. 2012). In *the left panels*, the evolutionary tracks correspond to non-rotating stars, whilst *the right panels* yield the results for stars rotating at $0.4 \times v_{\rm crit}$. The dotted red lines correspond to isochrones of 3.2 and 6.3 million years for *the left panels* and of 4.0 and 8.0 million years for *the right panels*.

almost complete mixing of the latter. In this situation, models predict that He would be enhanced in the atmosphere of the mass gainer and that the latter would become bluer and overluminous for its mass (Vanbeveren & de Loore 1994). If there is no strong spin-up and the accretion occurs rather slowly and is accompanied by a fast diffusion process, then the location of the gainer in the HRD should be very close to that of a normal star of the same mass and chemical composition (Vanbeveren et al. 1998). The star is rejuvenated, however: it lies on an isochrone that corresponds to a younger age than its actual age. The location of the primary in the HRD suggests that in the present case the second scenario is likely to apply with a very moderate rejuvenation, if any, of the primary. This conclusion is supported by the lack of a strong He enrichment, but it is at odds with the highly non-synchronous rotation of the primary reported above.

5.2. Comparison with other post-RLOF systems

In this section, we briefly compare the properties of HD 149 404 with those of two other O-type binaries, Plaskett's Star and LZ Cephei, which are probably in a post-case A RLOF evolutionary stage and have been analysed in a way similar to the present work (Linder et al. 2008; Mahy et al. 2011).

Plaskett's Star (HD 47 129) is an O8 III/I + O7.5 III binary with an orbital period of 14.4 days, slightly longer than that of HD 149 404, and a mass ratio near unity. Two observational facts suggest that the initially more massive primary has undergone a case A RLOF episode in the past (Linder et al. 2008). First, the projected rotational velocity of the secondary star is remarkably high (mean value of 272.5 ± 35.0 km s^{-1}) compared to that of the primary (mean value of 65.7 ± 6.3 km s^{-1}). This strongly asynchronous rotation likely stems from a spin-up of the secondary star through a recent transfer of angular momentum from the primary star. Second, the primary star displays nitrogen overabundance ($N/N_\odot = 16.6 \pm 5.0$) and carbon depletion ($C/C_\odot = 0.2 \pm 0.1$), as is typical of an advanced evolutionary stage, whilst no such nitrogen enrichment is seen in the secondary spectrum[4]. Given the present-day configuration of HD 47 129, it seems that the transfer of angular momentum and the resulting spin-up of the mass gainer (the secondary in this case) might have prevented accretion of a larger portion of the primary's mass.

LZ Cephei (HD 209 481) is an O9 III + ON9.7 V binary with a short orbital period of 3.07 days (Kameswara Rao 1972) and a mass ratio (primary/secondary) of 2.53 (Mahy et al. 2011). Both components of LZ Cep almost fill their Roche lobe (Mahy et al. 2011; Palate et al. 2013). Mahy et al. (2011) found that the secondary displays a strong nitrogen enrichment (18 times solar), carbon and oxygen depletion (0.1 times solar), and a high helium content (4 times solar), suggesting a very advanced state of evolution. On the other hand, the primary displays only slightly altered surface abundances consistent with single-star evolution. This suggests that the mass transfer was strongly non-conservative. Mahy et al. (2011) noted a slight asynchronicity of the rotation periods of the order of 10–20%, but concluded that the system is probably on the verge of achieving synchronization. Comparison with single-star evolutionary tracks indicates a similar age discrepancy as we have found here for HD 149 404. The evolutionary masses ($25.3^{+6.2}_{-4.0}$ and $18.0^{+2.4}_{-2.5}$ $M_\odot$, for the primary and secondary respectively) are significantly higher than their dynamical masses (16.9 ± 1.0 and 6.7 ± 1.0 $M_\odot$ respectively, Mahy et al. 2011; Palate et al. 2013).

Although our sample is currently too limited to draw firm conclusions, the above comparison reveals several interesting results that are worth studying in more detail with a larger sample. First, we note that in all three systems, the components appear either over- or under-luminous when compared with single-star evolutionary tracks corresponding to their present-day masses. During its initial phases, case A mass transfer occurs on a thermal timescale leading to a very rapid mass exchange. However, the mass transfer subsequently slows down and occurs on a nuclear timescale instead. By the time the mass transfer ends, both stars would therefore be expected to be in thermal equilibrium again. Since all three systems under consideration are in a detached configuration, the stars should thus have settled onto their new post-RLOF evolutionary tracks. The discrepancy between the observed luminosities and those predicted by the single-star evolutionary tracks most likely stems from several effects, such as observational uncertainties, altered chemical compositions (and hence opacities of the stellar material), and a rotational velocity history that differs from that assumed in the single-star models.

Our comparison shows that the degree of asynchronicity in the three post-RLOF systems increases with orbital period (from LZ Cep, over HD 149 404 to HD 47 129). This is most probably due to the higher efficiency of the tidal forcing in shorter period systems, or it might be seen as evidence that momentum transfer has played a larger role in those systems that have a wider present-day orbital separation. This is expected since binary evolution models predict spin-up to be less efficient in closer systems because in such systems the accretion stream directly affects the mass gainer without forming an accretion disk (e.g. Langer 2012). The questions of synchronization and circularization in close binary systems with early-type stars, featuring radiative envelopes and convective cores, have been addressed by Zahn (1975) and Tassoul (1987). Zahn (1975) considered radiative damping of the dynamical tide in the outer layers of the stellar envelopes as the main mechanism for synchronization. The corresponding synchronization timescales strongly depend upon the tidal torque constant E_2 , which varies by several orders of magnitude during the main-sequence lifetime of the star (Zahn 1977). Siess et al. (2013) provided a parametrization of this parameter as a function of stellar mass and relative age of the star. Assuming that their formalism holds for the masses of the stars considered here and adopting an age of half the main-sequence age of the stars, we estimated the values of E_2. We then evaluated the synchronization times following Eq. (4.28) of Zahn (1975) by means of moments of inertia tabulated by Claret & Giménez (1992). The results are 5.6×10^5 and 1.4×10^4 years for the primary and secondary stars of HD 149 404, respectively, 4.4×10^6 and 27.6×10^6 years for the primary and secondary of Plaskett's star, and 2.8×10^4 and 2.5×10^4 years for the primary and secondary components of LZ Cephei. Tassoul (1987), on the other hand, proposed that the most effective mechanism for synchronization is provided by large-scale hydrodynamic motions in the interiors of the tidally distorted binary components. The resulting timescales are considerably shorter than those estimated following the formalism of Zahn (1975). We estimate synchronization timescales of 2.1×10^4 and 3.2×10^3 years for HD 149 404, 7.2×10^4 and 2.0×10^5 years for Plaskett's star, and 1.6×10^3 and 6×10^2 years for LZ Cep. Regardless of which of the two formalisms is most appropriate to describe the evolution of rotation in the systems considered here, we find that, except perhaps for Plaskett's Star, which has a longer synchronization timescale, the RLOF phase probably must have ended less than a few 10^4 years ago.

Another puzzling result is the fact that the post-RLOF mass-ratio deviates most from unity for the shortest period system (LZ Cep). Therefore, in this system, the RLOF must have been comparatively more efficient than in the longer period systems. As discussed above, the mass transfer in LZ Cep was most likely highly non-conservative. If the material lost by the system does not carry away angular momentum in addition to the intrinsic orbital angular momentum, such a non-conservative mass loss leads to a widening of the orbital separation a given by

$$\frac{\dot{a}}{a} = -\frac{\dot{M}}{M},$$

where $\dot{M} < 0$ is the mass-loss rate (Singh & Chaubey 1986; Tout & Hall 1991). Assuming a fully non-conservative mass loss, this would imply that the initial orbital period of LZ Cep must have been shorter than 1.5 days. The duration of the RLOF episode depends on the evolution of the Roche-lobe filling factor of the mass donor. The evolution of the size of the Roche lobe is set by the relative importance of the orbit expansion and the shrinking of the relative size of the mass donor's Roche lobe. In addition, the evolution of the radius of the mass donor needs to be accounted for (see Tout & Hall 1991). Since massive stars

---

[4] The apparent N underabundance of the secondary inferred by Linder et al. (2008) could be an artefact that is due to the relatively shallow nitrogen lines of the secondary being washed out by its fast rotation and the difficulties of properly normalizing echelle spectra with such broad and shallow features (see also Fig. 1 of Palate & Rauw 2014).

with radiative envelopes contract considerably on a dynamical timescale (Tout & Hall 1991) and in view of the current mass-ratio of LZ Cep (Mahy et al. 2011), it seems unlikely that a non-conservative RLOF could be the explanation for a more efficient mass loss. Alternatively, if the material lost by the system carried off additional angular momentum, then the result could be a shrinking of the orbit. In active, low-mass stars, such a situation could arise if the material lost by the donor corotates with the latter under the effect of a magnetic field out to a wide distance (Tout & Hall 1991). However, strong magnetic fields are fairly rare among single massive stars (~7%), and their incidence appears even lower among massive binaries (Neiner et al. 2015). Hence, this scenario also appears very unlikely in the case of LZ Cep.

Clearly, the above trends call for confirmation by studying a larger sample of post-case A RLOF massive binary systems. We are currently undertaking such studies, and the results will be presented in forthcoming publications.

5.3. Summary and conclusion

We analysed the fundamental properties of the binary system HD 149 404 by means of spectral disentangling and the CMFGEN atmosphere code. Our investigation of this object represents a significant improvement over previous studies because we have obtained the individual spectra of each component. This led to the determination of a number of stellar parameters that were used to constrain the evolutionary status of the system.

We established the existence of a large overabundance in N and a C and O depletion in the secondary star and also found a slight N enhancement in the primary's spectrum. We showed that these surface abundances cannot be explained by single-star evolutionary models. Furthermore, we inferred an asynchronous rotation of the two stars of the system. These two results indicate a previous mass and angular momentum-exchange phase through a Roche-lobe overflow episode. Given the present status of HD 149 404 as an O+O binary, this mass transfer probably was a case A RLOF. However, dedicated theoretical studies are needed to understand the details of the evolution of this system.

Acknowledgements. The Liège team acknowledges support from the Fonds de Recherche Scientifique (FRS/FNRS) including especially an FRS/FNRS Research Project (T.0100.15), as well as through an ARC grant for Concerted Research Actions financed by the French Community of Belgium (Wallonia-Brussels Federation), and an XMM PRODEX contract (Belspo). Anthony Hervé is supported by grant 14-02385S from GA ČR.

References

Asplund, M., Grevesse, N., Sauval, A. J., & Scott, P. 2009, ARA&A, 47, 481
Chlebowski, T., & Garmany, C. D. 1991, ApJ, 368, 241
Claret, A., & Giménez, A. 1992, A&AS, 96, 255
Conti, P. S. 1973, ApJ, 179, 161
Conti, P. S. 1974, ApJ, 187, 539
Conti, P. S., & Alschuler, W. R. 1971, ApJ, 170, 325
Conti, P. S., & Frost, S. A. 1977, ApJ, 212, 728
de Loore, C., & Vanbeveren, D. 1994, A&A, 292, 463
de Mink, S. E., Pols, O. R., & Hilditch, R. W. 2007, A&A, 467, 1181
de Mink, S. E., Cantiello, M., Langer, N., et al. 2009, A&A, 497, 243
Dray, L. M., & Tout, C. A. 2007, MNRAS, 376, 61
Eggleton, P. P. 1983, ApJ, 268, 368
Ekström, S., Georgy, C., Eggenberger, P., et al. 2012, A&A, 537, A146
González, J. F., & Levato, H. 2006, A&A, 448, 283
Gray, D. F. 2008, The Observation and Analysis of Stellar Photospheres, 3rd edn. (Cambridge University Press)
Gray, R. O. 2010, `http://www.appstate.edu/~grayro/spectrum/spectrum276/node38.html`
Herbst, W., & Havlen, R. J. 1977, A&AS, 30, 279
Hillier, D. J., & Miller, D. L. 1998, ApJ, 496, 407
Howarth, I. D., Siebert, K. W., Hussain, G. A. J., & Prinja, R. K. 1997, MNRAS, 284, 265
Hurley, J. R., Tout, C. A., & Pols, O. R. 2002, MNRAS, 329, 897
Kameswara Rao, N. 1972, PASP, 84, 563
Kippenhahn, R., & Weigert, A. 1967, Z. Astrophys., 66, 58
Lanz, T., & Hubeny, I. 2003, ApJS, 146, 417
Langer, N. 2012, ARA&A, 50, 107
Langer, N., Wellstein, S., & Petrovic, J. 2003, Proc. IAU Symp., 212, 275
Linder, N., Rauw, G., Martins, F., et al. 2008, A&A, 489, 713
Mahy, L., Martins, F., Machado, C., et al. 2011, A&A, 533, A9
Mahy, L., Gosset, E., Sana, H., et al. 2012, A&A, 540, A97
Martins, F. 2011, Bull. Soc. Roy. Sci. Liège, 80, 29
Martins, F., & Hillier, D. J. 2012, A&A, 545, A95
Martins, F., & Plez, B. 2006, A&A, 457, 637
Martins, F., Schaerer, D., & Hillier, D. J. 2005, A&A, 436, 1049
Martins, F., Hervé, A., Bouret, J.-C., et al. 2015, A&A, 575, A34
Muijres, L. E., Vink, J. S., de Koter, A., Müller, P. E., & Langer, N. 2012, A&A, 537, A37
Nazé, Y., Carrier, F., & Rauw, G. 2002, in Interacting Winds from Massive Stars, eds. A. F. J. Moffat, & N. St-Louis, ASP Conf. Proc., 260, 457
Neiner, C., Mathis, S., Alecian, E., et al. 2015, in Proc. IAU, 305, 61
Palate, M., & Rauw, G. 2014, A&A, 572, A16
Palate, M., Rauw, G., & Mahy, L. 2013, Central European Astrophysical Bulletin, 37, 311
Petrovic, J., Langer, N., & van der Hucht, K. A. 2005, A&A, 435, 1013
Podsiadlowski, P., Joss, P. C., & Hsu, J. J. L. 1992, ApJ, 391, 246
Rauw, G. 2007, DSc Thesis, University of Liège, Belgium
Rauw, G. 2013, in Setting a New Standard in the Analysis of Binary Stars, eds. K. Pavlovski, A. Tkachenko, & G. Torres, EAS Pub. Ser., 64, 59
Rauw, G., Nazé, Y., Carrier, F., et al. 2001, A&A, 368, 212
Reed, B. C. 2003, AJ, 125, 2531
Sana, H., de Mink, S. E., de Koter, A., et al. 2012, Science, 337, 444
Siess, L., Izzard, R. G., Davis, P. J., & Deschamps, R. 2013, A&A, 550, A100
Simón-Díaz, S., & Herrero, A. 2007, A&A, 468, 1063
Simón-Díaz, S., & Herrero, A. 2014, A&A, 562, A135
Singh, M., & Chaubey, U. S. 1986, Ap&SS, 124, 389
Stickland, D. J., & Koch, R. H. 1996, The Observatory, 116, 145
Tassoul, J.-L. 1987, ApJ, 322, 856
Thaller, M. L., Gies, D. R., Fullerton, A. W., Kaper, L., & Wiemker, R. 2001, ApJ, 554, 1070
Tout, C. A., & Hall, D. S. 1991, MNRAS, 253, 9
Vanbeveren, D. 1982, A&A, 105, 260
Vanbeveren, D. 2011, Bull. Soc. Roy. Sci. Liège, 80, 530
Vanbeveren, D., & de Loore, C. 1994, A&A, 290, 129
Vanbeveren, D., de Loore, C., Van Rensbergen, W. 1998, A&ARv, 9, 63
van der Hucht, K. A. 1996, in Wolf-Rayet stars in the framework of stellar evolution, Liège Int. Astrophys. Colloq., 33, eds. J.-M. Vreux, A. Detal, D. Fraipont-Caro, E. Gosset, & G. Rauw, 1
Wellstein, S., Langer, N., & Braun, H. 2001, A&A, 369, 939
Wolk, S. J., Comerón, F., & Bourke, T. 2008, Handbook of Star Forming Regions, Vol. II: The Southern Sky, ASP Monograph Publications, Vol. 5. ed. Bo Reipurth, 388
Zahn, J.-P. 1975, A&A, 41, 329
Zahn, J.-P. 1977, A&A, 57, 383

3.3 LSS 3074

LSS 3074 is a short-period O-star binary system, with an orbital period of 2.185 days, located behind the Coalsack region. We selected this system for our study due to this very short period, which makes it a good candidate for a past RLOF episode. Besides, the primary star of LSS 3074 is listed in the literature as being one of the few known O4f stars. These objects are rare since they are thought to represent a short-lived transition phase in the evolution of massive O-type stars before they become Wolf-Rayet stars. Obtaining a good orbital and photometric solution of this system and determining the fundamental properties of its components offer therefore a precious opportunity to better understand these rare transition objects. Moreover, previous studies of LSS 3074 have provided surprisingly low minimum masses for such early-type objects (8 and 9 $M_\odot$, Morrell & Niemela 1990, Niemela et al. 1992).

Our analysis of LSS 3074 is based on three EMMI spectra taken in March 2002 at the 3.5 m New Technology Telescope (NTT) at the European Southern Observatory (La Silla ESO), three Fiber-fed Extended Range Optical Spectrograph (FEROS) échelle spectra collected in April 2002 with the ESO 1.52 m telescope at La Silla and nine FEROS échelle spectra taken in May 2003 and May 2004 with the 2.2 m ESO/MPE telescope at La Silla. The system was also observed in photometry with the Yale 1 m telescope at the Cerro Tololo Interamerican Observatory between March and May 2001, using the Johnson system B, V, R, and I filters. Finally, *XMM-Newton* (Jansen et al. 2001) observed LSS 3074 twice. The first observation, taken in August 2001, is centered on the system itself, and the second observation, taken in January 2003, is centered on the low mass X-ray binary XB 1323-619, located at 6.9 arcmin from LSS 3074. The corresponding X-ray images of the field are shown in Fig. 3.1.

Based on a number of well deblended lines in the optical spectra of LSS 3074, we computed an orbital solution of the system, assuming a circular orbit. We determined the orbital period by combining a Fourier analysis of the radial velocity curves and the photometric time series, and we obtained $P_{\rm orb} = 2.1852 \pm 0.0006$ days. Our orbital solution also leads to low minimum masses ($m \sin^3 i = 8.0 \pm 0.5$ and 9.3 ± 0.7 $M_\odot$ for the primary and secondary respectively), similar to those determined by Niemela et al. (1992).

This orbital solution then permitted us to recover the individual spectra of both components, using the disentangling method presented in Sect. 2.1. We then determined the spectral types of O5.5 If for the primary and of O6.5-7 If for the secondary from the reconstructed individual spectra. By comparing the equivalent widths of a number of spectral lines in the

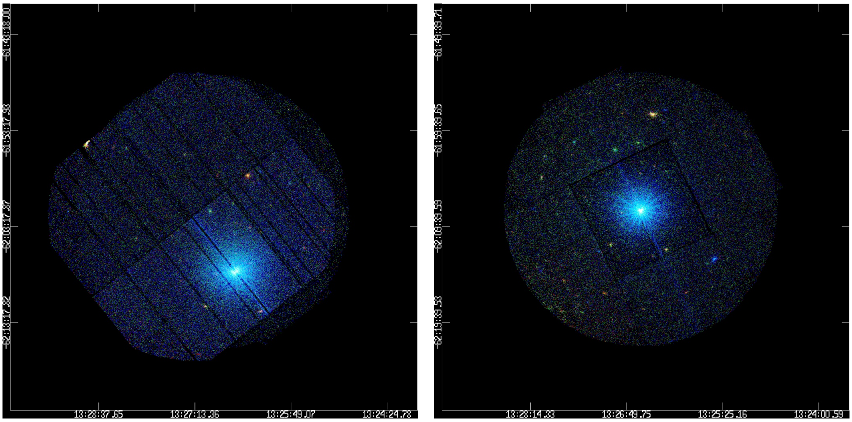

Figure 3.1: X-ray images of LSS 3074 and its surroundings. The left panel displays the first observation, centered on the system itself. The right panel shows the second observation, centered on the very bright X-ray binary XB 1323-619.

primary and secondary spectra with the mean equivalent widths of the same lines in synthetic spectra of stars with similar spectral types, we inferred a spectroscopic brightness ratio of $l_1/l_2 = 2.50 \pm 0.43$. Using a Fourier transform method on selected lines, we found that the primary and secondary display projected rotational velocities of 110 ± 13 km s^{-1} and 127 ± 6 km s^{-1} respectively. We also estimated their macroturbulence velocities to be 20 and 50 km s^{-1} respectively.

To determine the fundamental properties of both components of LSS 3074, we fitted the reconstructed spectra of the primary and secondary stars with the CMFGEN atmosphere code presented in Sect. 2.2, and obtained that they display $T_{\rm eff}$ of 39 900 K and 34 100 K, and $\log g$ of 3.82 and 3.83 respectively.

To improve our understanding of the geometry of the system, we performed an analysis of its photometric light curves. We concluded that LSS 3074 is very likely in overcontact configuration, with a filling factor of 1.008 for both stars and an orbital inclination of 54.5°. However, the corresponding brightness ratio is predicted to be 1.09, which is at odds with our spectroscopic brightness ratio of 2.5. Moreover, the hottest star appears to be in front during the deepest minimum, which leads to difficulties to fit this minimum.

From the spectroscopic analysis, we can stress two very interesting results. First, we confirmed the very low masses and radii found in a previous study by Morrell & Niemela (1990), which is unusual for stars with such spectral types. Second, we found a strong overabundance in N and a strong depletion in C and O in both primary and secondary stars. In addition, the primary star also displays a strong He enrichment in its atmosphere. We proposed several evolutionary pathways through a RLOF process to explain both the low masses and the chemical abundances of both components of LSS 3074. Moreover, we confirmed that the system is apparently in an overcontact configuration and has lost a significant fraction of its mass to its surroundings. We suggested that some of the discrepancies between the spectroscopic and photometric properties of the system may come from a strong radiation pressure of the primary.

The complete analysis of the LSS 3074 binary system is published in Raucq et al. (2017, see paper hereafter).

A&A 601, A133 (2017)
DOI: 10.1051/0004-6361/201630330

Astronomy & Astrophysics

Observational signatures of past mass-exchange episodes in massive binaries: the case of LSS 3074[⋆],[⋆⋆]

F. Raucq[1], E. Gosset[1], G. Rauw[1], J. Manfroid[1], L. Mahy[1], N. Mennekens[2], and D. Vanbeveren[2]

[1] Space sciences, Technologies and Astrophysics Research (STAR) Institute, Liège University, Quartier Agora, Allée du 6 Août 19c, Bât. B5c, 4000 Liège, Belgium
e-mail: `fraucq@doct.ulg.ac.be`
[2] Astronomy and Astrophysics Group, Vrije Universiteit Brussel, Pleinlaan 2, 1050 Brussels, Belgium

Received 22 December 2016 / Accepted 13 February 2017

ABSTRACT

Context. The role of mass and momentum exchanges in close massive binaries is very important in the subsequent evolution of the components. Such exchanges produce several observational signatures such as asynchronous rotation and altered chemical compositions, that remain after the stars detach again.
Aims. We investigated these effects for the close O-star binary LSS 3074 (O4 f + O6-7:(f):), which is a good candidate for a past Roche lobe overflow (RLOF) episode because of its very short orbital period, $P = 2.185$ days, and the luminosity classes of both components.
Methods. We determined a new orbital solution for the system. We studied the photometric light curves to determine the inclination of the orbit and Roche lobe filling factors of both stars. Using phase-resolved spectroscopy, we performed the disentangling of the optical spectra of the two stars. We then analysed the reconstructed primary and secondary spectra with the CMFGEN model atmosphere code to determine stellar parameters, such as the effective temperatures and surface gravities, and to constrain the chemical composition of the components.
Results. We confirm the apparent low stellar masses and radii reported in previous studies. We also find a strong overabundance in nitrogen and a strong carbon and oxygen depletion in both primary and secondary atmospheres, together with a strong enrichment in helium of the primary star.
Conclusions. We propose several possible evolutionary pathways through a RLOF process to explain the current parameters of the system. We confirm that the system is apparently in overcontact configuration and has lost a significant portion of its mass to its surroundings. We suggest that some of the discrepancies between the spectroscopic and photometric properties of LSS 3074 could stem from the impact of a strong radiation pressure of the primary.

Key words. stars: early-type – stars: fundamental parameters – stars: massive – stars: individual: LSS 3074 – binaries: eclipsing – binaries: spectroscopic

1. Introduction

Some recent studies have shown that a high percentage of massive stars belong to binary or higher multiplicity systems (e.g. Mason et al. 1998; Sana et al. 2012, 2014; Sota et al. 2014). This multiplicity enables us to observationally determine the minimum masses of the stars through their orbital motion, but it also influences the evolution of the stars in various ways (e.g. Langer 2012). These evolutionary effects range from tidally induced rotational mixing (e.g. de Mink et al. 2009), over exchange of matter and angular momentum through a Roche lobe overflow (RLOF) interaction (e.g. Podsiadlowski et al. 1992; de Loore & Vanbeveren 1994; Wellstein et al. 2001; Hurley et al. 2002), to the merging of both stars (e.g. Podsiadlowski et al. 1992; Wellstein et al. 2001). In RLOF interactions, one distinguishes three different situations: case A, if the RLOF episode occurs when the mass donor is on the core hydrogen-burning main sequence; case B, when the star is in the hydrogen shell burning phase; and case C, when the star is in the helium shell burning phase (Kippenhahn & Weigert 1967, Vanbeveren et al. 1998). Such binary interactions significantly affect the physical properties of the components and their subsequent evolution. Despite considerable progresses in theoretical models, a number of open issues, such as the actual efficiency of accretion, remain (e.g. Wellstein et al. 2001; de Mink et al. 2007; Dray & Tout 2007). To better understand this phenomenon, in-depth studies of systems undergoing or having undergone mass exchange are needed.

In this context, the short-period spectroscopic binary LSS 3074 (also identified as V889 Cen and ALS 3074), classified as O4f$^+$ + O6-7:(f): (Morrell & Niemela 1990), with $P_{\rm orb} = 2.185$ days, is an extremely interesting target. This system

---

[⋆] Based on observations collected at the European Southern Observatory (La Silla, Chile) and the Cerro Tololo Inter-American Observatory (Chile). CTIO is a division of the National Optical Astronomy Observatory (NOAO). NOAO is operated by the Association of Universities for Research in Astronomy (AURA), Inc., under cooperative agreement with the National Science Foundation (USA). Also based on observations collected with XMM-Newton, an ESA science mission with instruments and contributions directly funded by ESA member states and the USA (NASA).

[⋆⋆] Tables A.1–A.3 are only available at the CDS via anonymous ftp to `cdsarc.u-strasbg.fr` (`130.79.128.5`) or via `http://cdsarc.u-strasbg.fr/viz-bin/qcat?J/A+A/601/A133` is located behind the Coalsack region. The distance of this region was evaluated as 188 ± 4 pc (Seidensticker 1989; and Seidensticker & Schmidt-Kaler 1989). LSS 3074 harbours one of the very few known O4f stars. These objects are rare since they probably represent a short-lived transition phase in the evolution of massive O-type stars before they become Wolf-Rayet stars. In addition, the very short orbital period of this system makes it a good candidate for a past RLOF episode. Obtaining a good orbital and photometric solution for this system and determining the fundamental properties of its components are therefore of the utmost importance to better understand these transition objects.

A first preliminary orbital solution of LSS 3074 was presented by Morrell & Niemela (1990). The low $m \sin^3 i$ values inferred from this orbital solution (8 and 9 $M_\odot$) are rather surprising for such early-type objects. Niemela et al. (1992) provided an improved orbital solution and they discussed the phase-locked polarization variability of this system. Fitting a model to these variations, they inferred an inclination of $i = 75°$, yielding very low absolute masses of 10–11 $M_\odot$ and 11–12 $M_\odot$ for the O4f$^+$ and the O6-7 component, respectively. Niemela et al. cautioned however that tidal deformations could introduce additional polarization, biasing the inclination towards 90°. Optical light variations of LSS 3074 were first reported by Haefner et al. (1994), although these authors did not achieve a phase coverage of the light curve allowing them to clearly distinguish ellipsoidal variations from photometric eclipses. Haefner et al. suggested an inclination of 50–55°, yielding again rather low masses of 17–21 $M_\odot$ for both components.

In the present study, we discuss our determination of the orbital solution of this system and of the fundamental parameters of its components through several analysis techniques. Some very preliminary results were given in Gosset et al. (2005). The data used in our study are discussed in Sect. 2. In Sect. 3 and Sect. 4, we present the optical spectrum of LSS 3074 and our determination of its orbital solution. In Sect. 5, we perform a line profile variability study of several important lines of the optical spectrum of LSS 3074. In Sect. 6, we present the preparatory treatment of our data, including the disentangling of the observed spectra to reconstruct individual spectra of the binary components needed for the subsequent spectral analysis, and in Sect. 7, we analyse the light curve. The spectral analyses, carried out with the non-LTE model atmosphere code CMFGEN, are presented in Sect. 8. In Sect. 9, we conclude by a discussion concerning the evolutionary status of LSS 3074.

2. Observations and data reduction

2.1. Spectroscopy

Optical spectra of LSS 3074 were gathered with different instruments during several observing runs between 2002 and 2004 (see Table 1).

Three spectra were obtained with the EMMI instrument on the New Technology Telescope (NTT) at the European Southern Observatory (ESO) at La Silla during a three-day observing run in March 2002. The EMMI instrument was used in the échelle mode with grating #9 and grism #3, providing a resolving power of 7700. The data were reduced using the ECHELLE context of MIDAS, and 16 usable spectral orders, covering the wavelength domain from 4040 to 7000 Å, were extracted and normalized individually.

Twelve échelle spectra of LSS 3074 were taken with the Fiber-fed Extended Range Optical Spectrograph (FEROS; Kaufer et al. 1999). In April 2002, the spectrograph was attached to the ESO 1.52 m telescope at La Silla, while in May 2003 and May 2004, it was used at the 2.2 m ESO/MPE telescope at La Silla. The exposure times were 40–75 min. The detector was an EEV CCD with 2048 × 4096 pixels of 15 μm × 15 μm. We used an improved version of the FEROS context within the MIDAS package provided by ESO to reduce the data (Sana et al. 2006a).

2.2. Photometry

During March-April-May 2001, LSS 3074 was observed in photometry with the Yale 1 m telescope at the Cerro Tololo Interamerican Observatory. The telescope was operated in service mode (project A01A0098, PI E. Gosset) by the YALO consortium. The telescope was equipped with the imaging camera ANDICAM.

Beyond some shortening due to bad weather conditions, the run was initially split into two periods: from HJD 2 451 992 (2001-03-24) to HJD 2 452 003 (2001-04-04) and from HJD 2 452 023 (2001-04-24) to HJD 2 452 037 (2001-05-08). It was designed to optimize the Fourier spectral window for period determination with the least observing effort, while reaching a frequency resolution corresponding to a total duration of about 50 days without being hampered by the aliasing due to the central gap. In order to reduce the effect of the one-day aliasing in the photometric data, we tried to observe the star three times per night roughly at 3 h before meridian, at meridian and at 3 h after it.

The ANDICAM camera was equipped with a Loral CCD of 2048 by 2048 15 μm pixels. The projection of a pixel on the sky corresponds to 0.30″ allowing a convenient sampling. The whole field was thus covering a 10′ by 10′ square on the sky. The CCD was read out with two amplifiers. At the time of the observations it was characterized by a 11 e$^-$/pixel readout noise; the gain was set to 3.6 e$^-$ per ADU. Half of the CCD presented a variable noise pattern but the amplitude was sufficiently small not to be a concern. Moreover, LSS 3074 was systematically centred on the best half of the CCD.

The various measurements were performed using the Johnson system B, V, R, and I filters. Each measurement consisted of exposures of 2×10 s in B, 2×3 s in V, 1×1 s in R, and 2×1 s in I. For each night, a minimum of five dome flat fields in each filter and of 20 bias frames were acquired. A few Stetson standard fields (PG0918, PG1047, PG1323, PG1633, and SA107) were observed on three good nights (May 4, 5, and 8) to calibrate the above-mentioned photometric observations.

We reduced the raw data in the standard way (bias subtraction, division by a combined flat field, etc.) independently for the two halves of the CCD. The list of objects were built and the relevant instrumental magnitudes were extracted via DAOPHOT (Stetson 1987) under IRAF with both an aperture integration approach and a psf-fitting technique. A consistent natural system was established using a multi-night, multi-star, and multi-filter method as described in Manfroid (1993; see also Manfroid et al. 2001). A set of constant stars was iteratively constructed to perform precise relative photometry. The differential data were calculated with an aperture radius of 1.5″. A least-square fit of the standard star data allowed us to obtain absolute zero points and colour transformation coefficients using the large aperture (3.3″)

Table 1. Journal of the spectroscopic observations of LSS 3074.

HJD-2 450 000	Instrument	Exp. time (min.)	ϕ	RV_1 (km s^{-1})	RV_2 (km s^{-1})	$RV_{1,corr}$ (km s^{-1})	$RV_{2,corr}$ (km s^{-1})
2353.719	EMMI	60	0.48	–68.9		–70.3	
2354.691	EMMI	60	0.93	–183.6	72.4	–184.2	78.6
2355.720	EMMI	60	0.40	108.3	–160.7:	101.2	–154.4:
2381.596	FEROS	60	0.24	165.8	–203.6	161.9	–197.4
2382.597	FEROS	60	0.70	–246.7:	170.8:	–251.8:	159.1:
2383.598	FEROS	60	0.15	127.9:	–178.9:	123.2:	–172.6:
2783.576	FEROS	60	0.19	169.9:	–192.9	165.2:	–196.7
2784.620	FEROS	60	0.67	–255.6:	177.8:	–256.1:	173.8:
3130.613	FEROS	60	0.01	–51.3		–51.8	
3131.594	FEROS	75	0.46	–31.8		–29.1	
3132.576	FEROS	75	0.90	–198.0	77.3:	–203.1	69.1:
3133.629	FEROS	40	0.39	81.5	–156.3	76.9	–161.3
3133.660	FEROS	40	0.40	68.5	–151.3:	63.8	–156.3:
3134.578	FEROS	40	0.82	–266.7	154.7	–267.0	151.3
3134.608	FEROS	40	0.83	–257.8	162.8	–258.3	160.8

Notes. The phases (ϕ) are computed according to the ephemerides listed in Table 5. The radial velocities are presented in Sect. 4. The typical uncertainties on the RVs are 10–15 km s^{-1}. The colons indicate uncertainties larger than 20 km s^{-1}.

data. The derived colour transformation equations were

$$\begin{aligned}(B-V)_{\rm std} &= 0.0236\,(\pm0.0255) \\ &\quad +0.9991\,(\pm0.0323)\,(B-V)_{\rm ctio} \qquad (1)\\ (V-R)_{\rm std} &= 0.1016\,(\pm0.0153) \\ &\quad +0.7804\,(\pm0.0316)\,(V-R)_{\rm ctio} \qquad (2)\\ (V-I)_{\rm std} &= 0.0404\,(\pm0.0237) \\ &\quad +0.9396\,(\pm0.0249)\,(V-I)_{\rm ctio} \qquad (3)\\ V_{\rm std} &= -0.0145\,(\pm0.0181) \\ &\quad -0.0219\,(\pm0.0229)\,(B-V)_{\rm ctio}+V_{\rm ctio}. \qquad (4)\end{aligned}$$

The internal precision of the data corresponds to $\sigma = 0.007$, 0.010, 0.013, and 0.013 mag for the B, V, R, and I filters respectively, whereas the accuracy of the absolute magnitudes turned out to be $\sigma = 0.02$ mag. The measurements for LSS 3074 are available at the CDS in Table A.1. During the iterative removing of the variable stars, two stars were rejected early in the process and turned out to be significantly variable, i.e. HD 116827 and LSS 3072. They are further discussed in Appendix A and the corresponding measurements are available at the CDS in Tables A.2 and A.3.

2.3. XMM-Newton observations

XMM-Newton (Jansen et al. 2001) observed LSS 3074 twice. The first observation (ObsID 0109100201), taken in August 2001, was centred on LSS 3074 itself. The three EPIC (Strüder et al. 2001; Turner et al. 2001) cameras were operated in full-frame mode and the medium filter was used to discard optical and UV light. The corresponding X-ray image of the field can be found in Gosset et al. (2005). A second observation (ObsID 0036140201), centred on the low-mass X-ray binary XB 1323-619, was taken in January 2003. This time, the EPIC-pn camera and the central chip of the EPIC-MOS1 were operated in timing mode, whilst the EPIC-MOS2 was used in full-frame mode. All EPIC cameras were used in combination with the thin filter. The detectors used in timing mode do not provide data concerning LSS 3074. But since the star is located relatively far off axis in the second observation, it fell on one of the peripheral CCD chips of both MOS detectors. The raw data were processed with SAS v15.0.0 using calibration files available in June 2016 and following the recommendations of the *XMM-Newton* team[1]. We notably filtered the data to keep only best-quality data (PATTERN of 0–12 for EPIC-MOS and 0–4 for EPIC-pn data). Whilst the background level was high during the first observation, no genuine background flares due to soft protons affected either of the two observations. In the first observation, LSS 3074 falls very close to the out-of-time events of the very bright X-ray binary in the MOS2 data, thus rendering these specific data difficult to use.

Table 2. Journal of X-ray observations of LSS 3074.

Rev.	Instrument	Duration (ks)	JD (start) –2 450 000	JD (end) –2 450 000
0309	MOS1 & pn	9.9 & 6.0	2138.830	2138.945
0575	MOS1 & MOS2	50.5 & 50.8	2668.865	2669.452

We extracted the EPIC spectra of LSS 3074 via the task *especget*. For the source regions, we used a circular region with radius 30″, centred on the Simbad coordinates of the binary. The background was evaluated over an annulus with inner and outer radii of 30 and 45″, respectively. Specific ARF and RMF response files were computed to calibrate the flux and energy axes. The EPIC spectra were grouped with the SAS command *specgroup* to obtain an oversampling factor of five and to ensure that a minimum signal-to-noise ratio of 3 (i.e. a minimum of 10 counts) was reached in each spectral bin of the background-corrected spectra.

The EPIC spectrum of LSS 3074 peaks between 1.0 and 2.0 keV. It contains very few photons at energies below 1.0 keV (mainly as a result of the heavy absorption) and displays very weak emission at energies above 2 keV.

---

[1] `http://xmm.esac.esa.int/sas/current/documentation/threads/`

Table 3. X-ray spectral fits of LSS 3074.

Rev.	$\log N_{\mathrm{wind}}$ (cm^{-2})	kT (keV)	Norm (cm^{-5})	χ^2_ν	f_{X} (10^{-14} erg cm^{-2} s^{-1})	$f_{\mathrm{X}}^{\mathrm{un}}$
0309	$21.83^{+.25}_{-.48}$	$0.99^{+.65}_{-.33}$	$(1.26^{+1.06}_{-0.57})\,10^{-4}$	1.55(7)	3.6	8.7
0575	$22.07^{+.18}_{-.16}$	$0.47^{+.17}_{-.18}$	$(4.72^{+24.08}_{-2.54})\,10^{-4}$	1.55(14)	2.6	8.3
comb.	$22.00^{+.15}_{-.16}$	$0.57^{+.21}_{-.14}$	$(2.61^{+2.38}_{-1.03})\,10^{-4}$	1.64(24)	2.9	8.6

Notes. The normalization of the apec models is given as $\frac{10^{-14}\int n_{\mathrm{e}}\,n_{\mathrm{H}}\,\mathrm{d}V}{d^2}$ where d is the distance of the source (in cm), n_{e} and n_{H} are the electron and hydrogen densities of the source (in cm^{-3}). The error bars indicate 1σ uncertainties.

The fits of the X-ray spectra were performed with `xspec` (Arnaud 1996) version 12.9.0i. To evaluate the neutral hydrogen column density due to the interstellar medium (ISM), we adopt $B - V = 1.44$. Accounting for the intrinsic $(B - V)_0$ quoted by Martins & Plez (2006) and using the conversion between colour excess and neutral hydrogen column density of Bohlin et al. (1978), we estimate $N_{\mathrm{H}} = 0.99 \times 10^{22}$ cm^{-2}. The X-ray absorption by the ISM was modelled using the Tübingen-Boulder model (Wilms et al. 2000). X-ray spectra from massive stars can be further absorbed by the material of the ionized stellar wind. To model such an absorption, we imported the stellar wind absorption model of Nazé et al. (2004) into `xspec` as a multiplicative tabular model (hereafter labelled as `wind`). To the first approximation, the emission from massive stars can be represented by models of collisionally ionized equilibrium optically thin thermal plasmas. In our fits, we used `apec` models (Smith & Brickhouse 2001) computed with ATOMBD v2.0.2 as provided within `xspec`. The plasma abundances were taken to be solar (Asplund et al. 2009). Given the rather low quality of the spectra, reasonable fits were obtained for models of the kind `tbabs×wind×apec`. The results are listed in Table 3. Whilst the best-fit parameters of the two observations differ, these differences could be due to the ambiguity between a soft, highly absorbed plasma and a harder, less absorbed plasma. We have thus also performed a fit of the combined datasets. The results are again quoted in Table 3.

We find that the X-ray flux corrected for the ISM absorption is close to 8.6×10^{-14} erg cm^{-2} s^{-1}. If we consider the B and V magnitudes of LSS 3074 along with the bolometric corrections from Martins & Plez (2006), we obtain $\log L_{\mathrm{X}}/L_{\mathrm{bol}} \simeq -7.3$ which, given the uncertainties on both the X-ray and bolometric fluxes, is entirely compatible with the canonical value observed for most O-type stars (Sana et al. 2006b; Nazé 2009, and references therein).

3. Optical spectrum of LSS 3074

The spectrum of LSS 3074 is illustrated in Fig. 1. The stellar spectrum displays many absorption lines of H I, He I, He II, N III, N IV, and N V. The most prominent emission lines are He II λ 4686, N III $\lambda\lambda$ 4634-41, Hα, and He I λ 5876. Weaker emission lines of Si IV $\lambda\lambda$ 4089, 4116, 6668, and N IV $\lambda\lambda$ 4058, 6212-20 as well as P-Cygni emission components in He II λ 5412 and Hβ lines are also seen. In addition to some interstellar absorption lines (Na I, CH, CH$^+$), there are also numerous (and rather strong) diffuse interstellar bands (DIBs; see Herbig 1995). The strength of these features is an indication of the heavy interstellar absorption towards LSS 3074.

Table 4. Adopted wavelengths of the lines used to measure the RVs of LSS 3074.

Spectrum	Wavelength (Å)
H I	4340.47
He I	4471.48
He II	4541.59
He II	5411.52
He I	5875.62
He II	6406.44
He I	7065.24

Spectrum	Wavelength (Å)
N IV	4057.80
N V	4603.83
N V	4619.90
N III	4634.16
N III	4640.64

Notes. These effective wavelengths are taken from Underhill (1995). The *top part* displays the lines we used for the determination of the orbital solution of the system. The *bottom part* shows the main N emission and absorption lines.

The presence of N V $\lambda\lambda$ 4604 and 4620 may indicate that one of the components of LSS 3074 is rather hot (O3-O4, Walborn 2001, Walborn et al. 2002). The radial velocities of the N III $\lambda\lambda$ 4634, 4641, and N IV λ 4058 emission lines and the N V absorption lines are shown in Fig. 3 below and analysed in Sect. 6.2.

Several emission lines in the spectrum of the system display strong line profile variations. The most prominent modulations are seen in the He II λ 4686, He I λ 5876, and Hα lines (see Fig. 4) and they are presented in Sect. 5.

4. Orbital solution

Since LSS 3074 is a rather faint and heavily reddened object, the accuracy of any radial velocity (RV) determination is mainly limited by the S/N ratio of the data. Therefore, we have concentrated our efforts on the strongest absorption lines that are essentially free from blends with other features. In this way, we have measured the RVs of Hγ, He I $\lambda\lambda$ 4471, 5876, and 7065 and He II $\lambda\lambda$ 4542, 5412, and 6406 in the spectra. We adopted the effective wavelengths of Underhill (1995), as listed in Table 4.

For each observation, the RVs of the primary and secondary components were computed as the mean of the corresponding

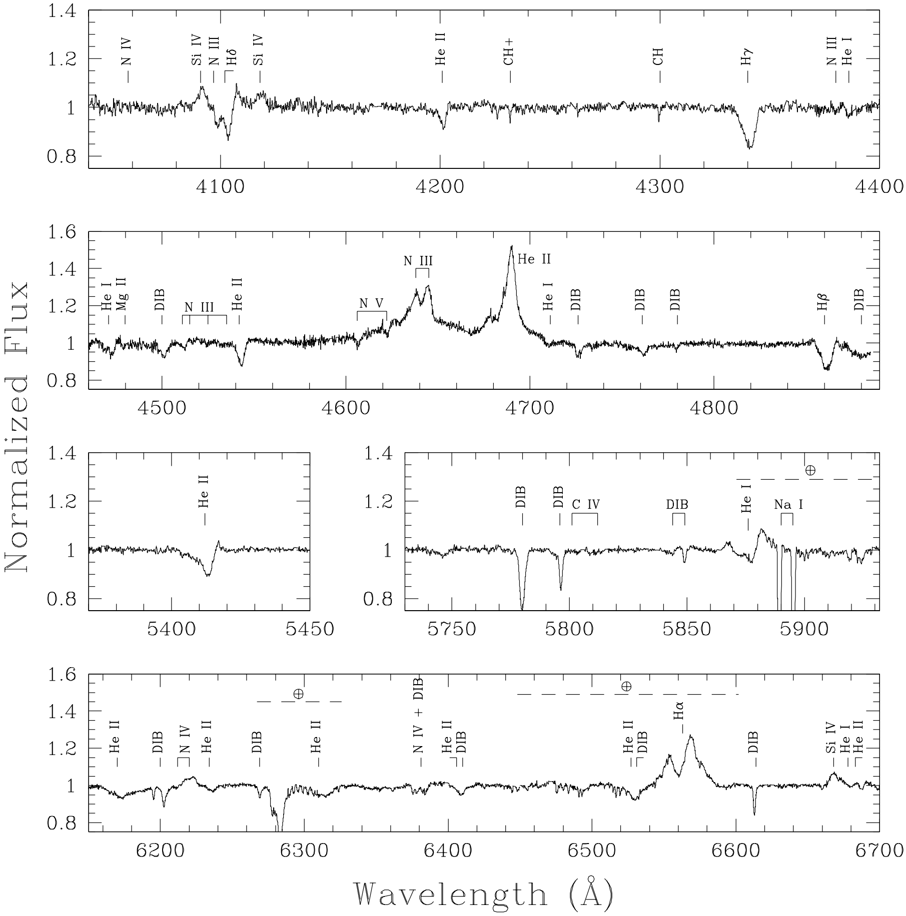

Fig. 1. Most important parts of the optical spectrum of LSS 3074 as observed with the EMMI instrument at the NTT on HJD 2 452 355.7, ϕ = 0.40. This spectrum is not corrected for the telluric absorption, and the main telluric bands are shown with dashed lines (Curcio et al. 1964).

RVs measured for the above listed lines on that observation. Unfortunately, either because of a low S/N or other problems, not all of these lines could be measured on all of our spectra. For instance, while we managed to deblend the primary and secondary components of the He I lines on most of our spectra, the intensity contrast between the two components is much larger for Hγ and for the He II lines. Therefore, the secondary component of the latter lines could only be resolved on the spectra with the highest S/N ratio. Another example is He II λ 5412: the proximity of several DIBs of similar strength as the secondary line and the fact that the line develops a P-Cygni type profile (with an emission component at a velocity of ~200 km s^{-1}) between phase ϕ = 0.35 and 0.50 lead to rather complex blends and thus highly uncertain RVs at these specific orbital phases. As a result, not all of the RV data points are based on the same set of lines. Yet, it is well known that in early-type stars featuring relatively strong winds, the systemic velocities of the different spectral lines can be significantly different (Rauw et al. 2002). Therefore combining different sets of spectral lines for different dates could bias the orbital solution. To circumvent this problem, we tied the RVs of the different lines to a single systemic velocity for each component. To do so, we first noted that the He I λ 5876 line is the one for which RVs of both components could be determined on nearly all observations, despite the fact that these absorptions lie on top of a broader emission. We thus selected He I λ 5876 as our reference line. The positions of the primary and secondary He I λ 5876 lines are shown in Fig. 4. For each of the other lines that we measured, we then determined the mean RV shift compared to He I λ 5876, and we subtracted this mean shift from the actual measurements. For each observation, the corrected RVs were then averaged, resulting in a homogeneous set of values, expressed in the rest frame of the He I λ 5876 line.

These resulting RVs are listed in Table 1. For most data points, the uncertainties on these RVs are about 10–15 km s^{-1}. In some cases however (indicated by the colons in Table 1), the uncertainties are larger than 20 km s^{-1} and can reach ~40 km s^{-1} in one case (HJD 2 452 382.597). To adopt the same notations as previous investigators, we refer to the brightest and hottest component of LSS 3074 as the primary, though its present-day mass appears to be lower than that of its companion (see below).

Owing to the severe aliasing problem, it is extremely difficult to obtain an independent determination of the orbital period of LSS 3074 from our set of RV measurements only. A Fourier analysis of the RV$_1$ and RV$_2$ data yields the highest peaks around $\nu = 0.46020$ d^{-1} ($P_{\rm orb} = 2.1730$ days) and $\nu = 0.45762$ d^{-1} ($P_{\rm orb} = 2.1852$ days). However, we caution that there are many more aliases that could hide the actual orbital period. It is worth pointing out that the second peak yields almost exactly the same period as found by Niemela et al. (1992). We performed the same Fourier analysis for each of the four bandpasses of the photometric data, *B*, *V*, *R*, and *I*, and obtained a highest peak at $\nu = 0.9158$ d^{-1}, which corresponds to an orbital frequency of $\nu = 0.9158/2 = 0.4579$ d^{-1}, corresponding to $P_{\rm orb} = 2.184$ days. While the periodogram of the photometric time series allows us to unambiguously identify the correct alias, the natural width of its peaks is much larger than in the case of our spectroscopic time series. In fact, folding the RVs into the photometric period yields an unacceptably large scatter. Therefore, combining the results from periodograms of the photometric and spectroscopic time series, we find that the most likely period of LSS 3074 is 2.1852 ± 0.0006 days, with the error bars given as 1σ deviation.

Also, the T_0 obtained with the photometric curves is HJD 2 452 000.9568, which corresponds to a phase shift of ~0.05 with the T_0 obtained with the RV data. If we lock the RV data to this T_0, we obtain a period of 2.1849 days. Considering that this result is well within the error bars of our previous calculations, we can admit the phase alignment of the RV and photometric data.

As a consistency check, we also combined our measurements in the *V* band with those taken by Haefner et al. (1994) and obtained a highest peak of the periodogram at $\nu = 0.9153$ d^{-1}, which corresponds to an orbital frequency of $\nu = 0.9153/2 = 0.45765$ d^{-1}, corresponding to $P_{\rm orb} = 2.1851$ days. This result tends to confirm the quality of our determination of the orbital period of the system.

Adopting an orbital period of 2.1852 days, we computed an orbital solution assuming a circular orbit. The RVs were weighted according to their estimated uncertainties. The result is shown in Fig. 2 and the corresponding orbital elements are provided in Table 5.

The RV amplitudes of our solution are in reasonable agreement with values from the literature ($K_1 = 222$ and $K_2 = 218$ km s^{-1}; Niemela et al. 1992). Consequently our orbital solution also leads to low minimum masses, similar to those of Niemela et al. ($m \sin^3 i = 9.5$ and 10 $M_\odot$ for the O4f primary and the secondary, respectively). The apparent systemic velocity of the primary is significantly more negative than that of the secondary. This most likely indicates that the absorption lines of the primary are not entirely formed in the static photosphere, but arise at least partly from an expanding stellar wind.

Figure 3 shows the RVs of the nitrogen emission and absorption lines in the spectrum of LSS 3074. The adopted effective wavelengths of the studied lines are listed in Table 4. All the lines seem to move with the primary, but the scatter of the velocities of the various lines is rather large, especially at phases between the 0.25 quadrature and 0.5 conjunction. During this phase interval, the N III emission lines yield systematically larger velocities than the N V absorption.

Table 5. Orbital solution computed from our RV data of LSS 3074 assuming a circular orbit and an orbital period of 2.1852 days.

	Primary	Secondary
T_0 (HJD - 2 450 000)	2000.851 ± 0.008	
γ (km s^{-1})	−66.0 ± 5.0	−21.7 ± 4.7
K (km s^{-1})	228.5 ± 7.1	196.0 ± 6.1
$a \sin i$ ($R_\odot$)	9.9 ± 0.3	8.5 ± 0.3
$q = m_1/m_2$	0.86 ± 0.04	
$m \sin^3 i$ ($M_\odot$)	8.0 ± 0.5	9.3 ± 0.7
$R_{\rm RL}/(a_1 + a_2)$	0.37 ± 0.01	0.39 ± 0.01
$R_{\rm RL} \sin i$ ($R_\odot$)	6.7 ± 0.2	7.2 ± 0.2
$\sigma_{\rm fit}$	3.11	

Notes. T_0 refers to the time of conjunction with the primary being in front. γ, K and $a \sin i$ denote respectively the apparent systemic velocity, the semi-amplitude of the radial velocity curve and the projected separation between the centre of the star and the centre of mass of the binary system. $R_{\rm RL}$ stands for the radius of a sphere with a volume equal to that of the Roche lobe computed according to the formula of Eggleton (1983). All error bars indicate 1σ uncertainties.

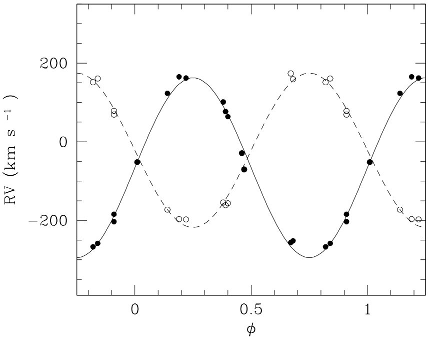

Fig. 2. Radial velocities of the components of LSS 3074 assuming a period of 2.1852 days. The RVs of the primary and secondary stars are shown with filled and empty circles, respectively. The solid and dashed lines indicate the orbital solution from Table 5.

5. Line profile variability

The most prominent emission lines in the optical spectrum of LSS 3074 show strong profile variations (see Fig. 4). For instance, the He II λ 4686 line evolves from a broad and skewed emission (around $\phi = 0.0$) into a double-peaked feature with rather narrow individual peaks and the strongest peak closely following the orbital motion of the primary (at phases near 0.5).

On the other hand, the Hα emission features a double-peaked profile on most of our spectra and the profiles observed around the two conjunctions are very similar. At phases near quadrature, the peaks are broader and less clear cut. Apart from the moving absorption lines, the He I λ 5876 profile has a morphology relatively similar to that of the Hα line.

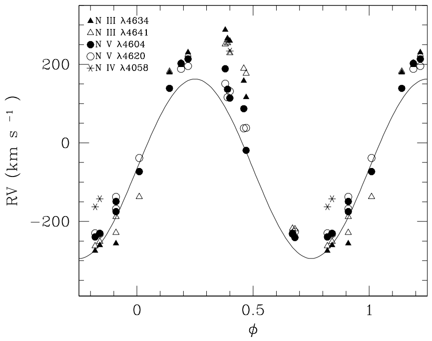

Fig. 3. Radial velocities of the N III and N IV emission lines and the N V absorptions in the spectrum of LSS 3074. The meaning of the various symbols is given in the upper left corner. The solid line yields the orbital solution of the primary from Table 5.

We measured the equivalent widths (EWs) of the Hα line between 6513 and 6604 Å. We find that $\overline{EW} = 4.09 \pm 0.60$ Å. Although the dispersion around the mean is quite large, no obvious phase-locked behaviour is apparent. In particular, we do not see any variations attributable to the modulation of the continuum.

These complex line morphologies make it impossible to assign a single RV to the He II λ 4686 and Hα emission lines, and suggest that these lines do not arise in the atmosphere of one of the two stars, but stem from an extended emission region. To further quantify this situation, we used the method of Doppler tomography to map the emitting regions of the He II λ 4686 and Hα lines in velocity space. Our method is based on the Fourier-filtered back projection technique (Horne 1991; Rauw et al. 2002; Mahy 2011). The radial velocity of any gas flow that is stationary in the rotating frame of reference of the binary can be expressed as

$$v(\phi) = v_x \cos(2\pi\phi) - v_y \sin(2\pi\phi) + v_z \qquad (5)$$

where ϕ stands for the orbital phase with $\phi = 0.0$, corresponding to the primary star being in front. The (v_x, v_y, v_z) are the velocity coordinates of the gas flow. The x and y axes are located in the orbital plane. The x-axis runs from the primary to the secondary, whilst the positive y-axis points in the direction of the orbital motion of the secondary. The v_z component represents the apparent systemic velocity of the line under consideration. The Doppler map consists of a projection of relation given by (5) on the (v_x, v_y) plane. For a given value of v_z, each pixel in a Doppler map, specified by its velocity coordinates, is therefore associated with a particular form of Eq. (5). All our spectra listed in Table 1 were given equal weights. The Doppler maps, computed adopting $v_z = -44\,\mathrm{km\,s^{-1}}$, are shown in Fig. 5. They reveal extended line formation regions in velocity space with different morphologies for the two lines. The He II λ 4686 line features an emission lobe on the negative v_x side and mostly with negative v_y. This emission seems thus mostly associated with the primary star. The Hα Doppler map displays two lobes, extending on both sides of the Roche lobes in velocity space, with the strongest one closely matching the emission lobe of the Doppler map of He II λ 4686.

A full interpretation of these Doppler maps in terms of wind-wind interactions is beyond the scope of the present paper. However, it is interesting to compare our Doppler maps with those of Algol-type systems where a cool star fills up its Roche lobe and transfers matter to a hotter companion (Richards et al. 2014). Our maps are clearly different from those presented by Richards et al. (2014). The structures seen in Fig. 5 neither resemble those produced by gas streams that directly impact the mass gainer nor do they feature the ring-like structure, centred on the mass gainer, that appears for systems with Keplerian accretion disks. These results therefore do not support the presence of an accretion disk or an accretion stream in LSS 3074.

6. Preparatory analysis

6.1. Spectral disentangling

The determination of the orbital solution allowed us to recover the individual spectra of both components through the disentangling of the normalized spectra of the binary system. For this purpose, we used our disentangling routine (Rauw 2007) based on the method of González & Levato (2006), previously used by Linder et al. (2008) and improved by Mahy et al. (2012). In this procedure, the mean spectra of each binary component are reconstructed in an iterative way by shifting the observed data into the frame of reference of one star and subtracting the best approximation of the spectrum of the other star shifted to its observed radial velocity. In the disentangling carried out in this work, we fixed the RVs of the binary components to those corresponding to the orbital solution of Sect. 4. For a more detailed description of the method, see Raucq et al. (2016).

As for any disentangling method, this technique also has its limitations (González & Levato 2006). An important limitation for our study is that broad spectral features are not recovered with the same accuracy as narrow ones. Indeed, features that are wider than a few times the RV amplitude are barely properly recovered. This is the case of the wings of the Balmer lines, for example. Moreover small residual errors in the normalization of the input spectra can lead to oscillations of the continuum in the resulting disentangled spectra on wavelength scales of several dozen Å, and a reasonable observational sampling of the orbital cycle is needed because the quality of the results depends on the radial velocity ranges covered by the observations. Finally, spectral disentangling works on continuum-normalized spectra and does not yield the brightness ratio of the stars, which must be determined by other techniques (see below).

In the particular case of LSS 3074, we also encountered problems due to the large brightness ratio of the system. Indeed, as shown in Sect. 6.3, the primary star appears much brighter than the secondary star, meaning that the latter is faint in the observed spectra, which induces difficulties in the disentangling procedure, a lower S/N ratio, and thus larger uncertainties on the resulting secondary spectrum.

6.2. Spectral types

We then determined the spectral types of the stars through the measurement of the equivalent width ratio of some spectral lines of the reconstructed individual line spectra of the primary and secondary components. We used the He I λ 4471 and He II λ 4542 lines, on the one hand, and Si IV λ 4089 and He I λ 4143 lines, on the other hand, and applied the Conti quantitative classification criteria for O-type stars (Conti & Alschuler 1971; Conti & Frost 1977; see also van der Hucht 1996) for both spectral types and luminosity classes. In this way, we obtain O5.5 I and O6.5-7 I classifications for the primary and secondary, respectively. The strong He II λ 4686 and N III $\lambda\lambda$ 4634-41 emission

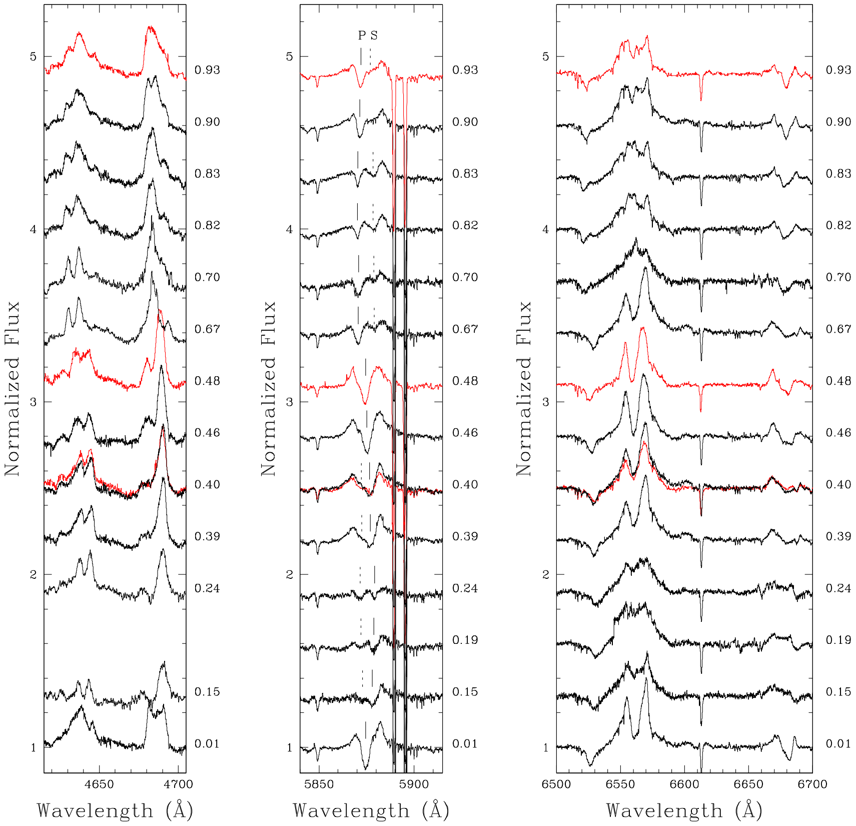

Fig. 4. Line profile variations of some important emission lines in the optical spectrum of LSS 3074. N III $\lambda\lambda$ 4634-4641 and He II λ 4686 are shown in *the left panel*; He I λ 5876 is represented in *the central panel*; and Hα is indicated in the right panel. The orbital phases computed according to the ephemerides in Table 4 are given on the right of each panel. The red spectra correspond to the EMMI observations. The vertical solid (resp. dotted) lines in *the middle panel* represent the position of the primary (resp. secondary) He I λ 5876 line for the given observation.

lines lead to the addition of an f qualifier (see Walborn et al. 2002; Sota et al. 2011; Maíz Apellániz et al. 2016, and references therein) for both components. The primary spectrum further displays emissions of Si IV $\lambda\lambda$ 4089, 4116. Previously these features were indicated by an f$^+$ qualifier, but it has been suggested that this notation is obsolete (Sota et al. 2011).

However, the Conti criterion for the luminosity classes is formulated for spectral types from O7 to O9.7 and its application to the spectrum of the primary star is thus an approximation. Moreover, Walborn et al. (2002) argued that it would be preferable to use the N IV/N III emission line ratio for the spectral classification of the earliest O-type stars rather than the ratio of the He I/He II absorption lines. As shown in Fig. 3, the N III $\lambda\lambda$ 4634, 4641, and the very weak N IV λ 4058 emission line (when present) clearly move along with the primary star. The same holds true for the weak, but definite N V $\lambda\lambda$ 4604 and 4620 absorption lines. As indicated in Sect. 3, the presence of these N V absorption lines points towards a rather hot star with an O3 to O4 spectral type (Walborn et al. 2002; Sota et al. 2011), which is at odds with our above classification based on the helium lines. We have thus compared our disentangled primary spectrum with the spectral atlas of Sota et al. (2011). The strong He II λ 4686 emission clearly confirms a supergiant luminosity class. The simultaneous presence of strong N III, very weak N IV, and definite N V lines in the spectrum of the primary is clearly a challenge both for spectral classification and spectral modelling (see Sect. 8.4). The best match, although certainly not perfect, is found with the spectra of HD 14 947 (O4.5 If) and, to a lesser extent, HD 15 570 (O4 If). For a highly deformed star, such as the primary of LSS 3074, gravity darkening leads to a non-uniform surface temperature. Hence, the discrepancy between the O5.5 If spectral type inferred from the relative strengths of the He I and He II lines and the O4-4.5 If type derived from the nitrogen spectrum could simply reflect the fact that these lines form over different parts of the stellar surface. We come back to this point in Sect. 8.4. For the secondary star, comparison with the atlas

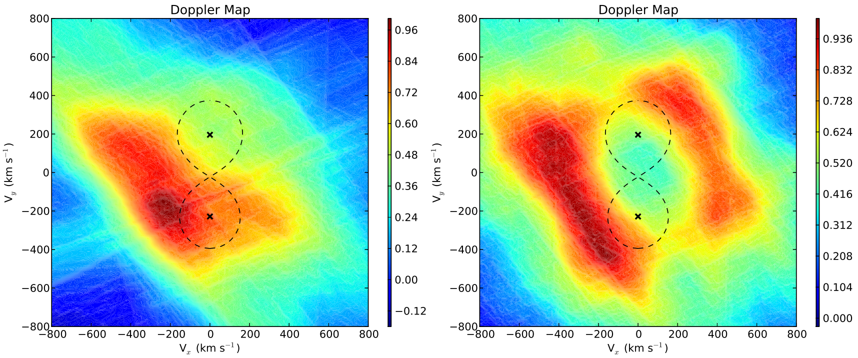

Fig. 5. Doppler maps of the He II λ4686 (*left*) and Hα (*right*) emission lines in the spectrum of LSS 3074. The crosses correspond to the radial velocity amplitudes of the centre of mass of the primary (negative v_y) and secondary (positive v_y), whereas the dashed lines indicate the Roche lobe in velocity space for a mass ratio $m_1/m_2 = 0.86$. The colour scale indicates the level of the line emissivity relative to its maximum value.

of Sota el al. (2011) yields a spectral classification O6.5-7 If, in agreement with the results from the relative strengths of the helium lines.

Finally, since our classification is based on the disentangled spectra, it is less sensitive to a possible phase dependence of the line strengths and should thus be more robust than a classification based only on spectra collected near quadrature phases.

6.3. Brightness ratio

The spectral disentangling yields the strength of the lines in the primary and secondary stars relative to the combined continuum. But as we mentioned earlier, it does not allow us to establish the relative strengths of the continua. We therefore needed to first establish the brightness ratio of the stars to further analyse the reconstructed spectra.

To estimate the optical brightness ratio of the components of LSS 3074, we measured the equivalent widths, referring to the combined continuum of the two stars, of a number of spectral lines on the reconstructed primary and secondary spectra. The results are listed in Table 6 along with the mean equivalent widths of the same lines in synthetic spectra of stars of the same spectral type, computed with the non-LTE model atmosphere code CMFGEN (Hillier & Miller 1998), which we describe in Sect. 8.2. For comparison, we also list the mean equivalent widths of the same lines in spectra of stars of similar spectral type as measured by Conti (1973, 1974) and Conti & Alschuler (1971).

The brightness ratio of the two stars can then be evaluated from

$$\frac{l_1}{l_2} = \left(\frac{EW_1}{EW_2}\right)_{\rm obs} \left(\frac{EW_{O7}}{EW_{O5.5}}\right)_{\rm mean}.$$

By combining our measurements with those from synthetic spectra, we derive an optical brightness ratio of 2.50 ± 0.43. As a consistency check, we can also determine the brightness ratio through a comparison with the measurements made by Conti, and we obtain 2.61 ± 0.41.

The disentangled continuum normalized primary and secondary optical spectra are shown in Fig. 8.

7. Light curve

To improve our understanding of the system LSS 3074, and in particular its geometry, we performed an analysis of the photometric light curves by modelling the system using the eclipsing binary star simulator NIGHTFALL[2], developed by Wichmann, Kuster and Risse. We worked in an iterative way. First of all, we fixed the mass ratio and orbital period to the values obtained from the orbital solution (see Table 5) and the effective temperatures to typical values for stars of similar spectral types (Martins et al. 2005). This permitted us to obtain a first estimation of the photometric solution and of the stellar radii and masses. Based on these approximated parameters, together with the effective temperatures, we calculated the associated surface gravities and stellar luminosities. This first approximation of the stellar fundamental parameters was then used as starting point input in our study of the atmosphere modelling procedure (see Sects. 8.2 and 8.3). This procedure then permitted us to accurately determine the effective temperatures of the stars, giving us a new input for the light curve study with NIGHTFALL.

Inspection of the light curve reveals a lack of a plateau between the minima, indicating important contributions of ellipsoidal variations to the photometric variability. Actually, the shape of the light curve suggests that almost the entire photometric variations could stem from such ellipsoidal variations, thereby implying that at least one of the stars must fill or overflow its Roche lobe.

The only evidence for the existence of genuine eclipses comes from the fact that the secondary minimum seems about 0.02 mag deeper than the primary minimum. The primary minimum corresponds to the occultation of the primary star by the secondary. What is surprising here is that the deeper minimum actually corresponds to the spectroscopically hotter star being in front. Given the level of dispersion in the light curve, it is quite possible that the small difference in depth of the minima is not significant and could arise, for example, from intrinsic variations of the stars. An alternative explanation for this situation could be an atmospheric eclipse produced by the wind of the primary

---

[2] For more details, see the NIGHTFALL user manual by Wichmann (1998) available at the URL: `http://www.hs.uni-hamburg.de/DE/Ins/Per/Wichmann/Nightfall.html`

Table 6. Brightness ratio determination from the dilution of prominent lines.

Line	Equivalent width (Å)						l_1/l_2
	Observations		Synthetic spectra		Conti (1973, 1974)		
	Primary	Secondary	O5.5	O7	O5.5	O7	
He I λ 4026	0.42	0.19	0.51	0.69	0.46	0.61	3.00
He II λ 4200	0.41	0.17	0.53	0.45	0.58	0.59	2.00
Hγ	0.90	0.34	1.56	1.75	1.85	2.22	3.00
He I λ 4471	0.25	0.26	0.29	0.61	0.29	0.59	2.08
He II λ 4542	0.56	0.19	0.62	0.53	0.75	0.67	2.43

Notes. The measured EWs are compared with values for the same lines in synthetic spectra of the same spectral type and in the compilation of measurements from the literature. The last column yields the brightness ratio for each line considered, using the synthetic spectra EWs.

star. Antokhina et al. (2013) studied the impact of free electron scattering in the wind of one star on the light curves of close eclipsing binaries. For a contact binary made of otherwise equal stars, these authors show that the presence of a stellar wind with $\dot{M} = 10^{-5}\,M_{\odot}\,\mathrm{yr}^{-1}$ around one component deepens the eclipse corresponding to the star with the wind passing in front of its companion by about 0.08 mag. At the same time, the depth of the other eclipse is slightly reduced. In the case of LSS 3074, the fact that most emission lines closely follow the motion of the primary star suggests that this star has the strongest wind, thus lending support to this explanation. However, as pointed out by Antokhina et al. (2013), a quantitative assessment of the impact on the light curve requires some independent determination of the wind parameters (mass-loss rate, asymptotic velocity and exponent of velocity law). In our case, this is difficult to achieve (see Sect. 8). This is because of the lack of UV spectroscopy and the complexity of the line emission regions. Indeed, as revealed by our tomographic analysis, at least parts of the Hα and He II λ 4686 emissions arise from an interaction zone and these lines hence do not necessarily reflect the genuine properties of the winds. Yet, our best-fit model atmosphere parameters (see the forthcoming Table 10) yield upper limits on the wind density that could be consistent with the observed difference in eclipse depth. However, these best-fit parameters also suggest that both binary components lose material at a similar rate. Hence, one would expect both eclipses to be affected by stellar wind absorption. We thus conclude that a better knowledge of the wind parameters of LSS 3074 is required before we can attempt a model of the light curve accounting for the effects of the stellar winds. Whatever the origin of the slight difference in depth of the minima, we need to keep in mind that this situation affects the quality of the fits of the light curve.

To explain the shape of the secondary minimum by the sole effect of ellipsoidal variations, we at least need to assume that either both components of the binary system fill up (contact-contact) or even overflow their Roche lobes (overcontact), or that one of the components must be much smaller and much fainter than the other star that fills up its Roche lobe. In the former case, one expects both stars to be of very comparable size and, given their effective temperatures, also of rather comparable brightness. To explain the depth of almost 0.2 mag by the sole effect of ellipsoidal variations is actually not possible here without requiring the presence of true eclipses. In this context, the necessity to invoke a contact-contact or an overcontact configuration remains valid, along with the conclusion that sizes and brightness of both stars should be comparable.

This is precisely the outcome of our fits with the NIGHTFALL code. The best-fit quality ($\chi^2_\nu = 4.4$) is achieved for overcontact configurations with a filling factor of 1.008 ($i \simeq 54.5°$), where the corresponding V-band brightness ratio is predicted to be 1.09. The corresponding photometric solution is presented in Table 7 and the associated plot is shown in Fig. 6. Yet, our spectroscopic analysis suggests an optical brightness ratio (primary/secondary) near 2.50. This situation is thus clearly at odds with explaining the photometric light curve via a double contact or overcontact configuration. To achieve a brightness ratio of 2.50 ± 0.43, the ratio between the mean radii of the primary and secondary stars would have to be 1.15 ± 0.10. This translates into a ratio of the filling factors of 1.23 ± 0.11, which is only possible for detached or semi-detached configurations. As could be expected, the fact that the hotter star is in front during the deepest minimum leads to difficulties to fit this minimum.

Table 7. Photometric solution for LSS3074.

Parameters	Primary	Secondary
i (°)	54.5 ± 1.0	
$q = m_1/m_2$	0.86 (fixed)	
Filling factor[a]	1.008 ± 0.010	1.008 ± 0.010
$T_{\rm eff}$ (K)	39 900 (fixed)	34 100 (fixed)
$m\,(M_{\odot})$	14.8 ± 1.1	17.2 ± 1.4
$R_{\rm pole}\,(R_{\odot})$	7.8	8.4
χ^2	1820.7	
$N_{\rm d.o.f.}$	415	

Notes. $N_{\rm d.o.f.}$ is the number of degrees of freedom. [(a)] The filling factor of a given binary component is defined here as the fraction of its polar radius over the polar radius of its Roche lobe.

Since the eclipses are only partial, one way to solve this issue would be to postulate the existence of a dark spot on the side of the secondary star facing the primary. Such a spot would then lead to a deeper minimum when the primary star is in front. From a purely numerical point of view this would improve the fit quality significantly with χ^2_ν now approaching 2.9. In addition, it would certainly help to bring the spectroscopic and photometric brightness ratios into better agreement. Yet, aside from the difficulty of explaining the physical origin of such a spot, there is another issue that concerns the fact that the spot size and its dim factor (i.e. the reduction in local temperature) are not fully independent and we lack any objective constraints on these parameters. Test calculations have shown that for some situations, the best-fit model would actually correspond to a spot that covers more than 75% of the surface of the secondary, which is clearly not physical.

As an alternative to the overcontact configuration, one might consider a scenario where the primary star overflows its Roche

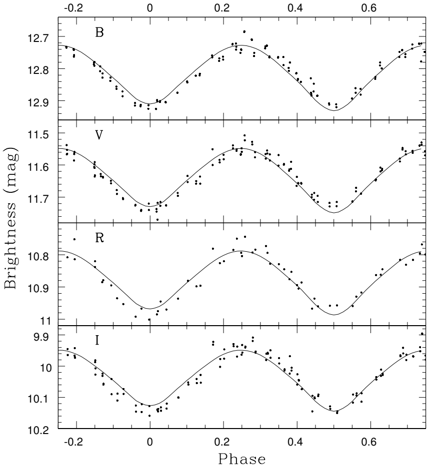

Fig. 6. Photometry of LSS 3074. The observational data are presented as black dots, and the solid black line corresponds to the best-fit theoretical light curve fit with NIGHTFALL with the parameters presented in Table 7. The zero phase corresponds to the secondary eclipse, when the primary is occulting the secondary.

lobe and transfers matter to a geometrically thick accretion disk around the more massive secondary star. This kind of scenario has been proposed to explain the light curves of β Lyrae (Wilson 1974), RY Sct (Antokhina & Kumsiashvili 1999), and V455 Cyg (Djurašević et al. 2012), among others. On the positive side of such a scenario, it might help reconcile the photometric and spectroscopic brightness ratios. On the negative side, we have the lack of a clear signature of an accretion disk in the Doppler maps of the Hα line and the fact that LSS 3074 is a very compact system, leaving very little room for the formation of a disk, unless the secondary star is very small. To test this scenario, we used the disk option in the NIGHTFALL code. In addition to the effective temperatures that we fixed at the values obtained from our model atmosphere fits (see Sect. 8.3), we set the Roche lobe filling factor of the primary star to unity and that of the secondary star to 0.75. This choice results in a brightness ratio that is consistent with our spectroscopic value. We tested various options for the disk available in the NIGHTFALL code (simple disk with uniform temperature, isothermal disk and reprocessing disk), which correspond to different prescriptions of the variations of the disk height and temperature with radius. Since the disk in our models resembles more an annulus than a genuine disk, these three options actually yield nearly identical results. These models fail to reproduce the width of the secondary minimum. This failure increases the χ^2 of the fits. Still, we managed to find fits with $\chi^2_\nu \sim 4.6$, but this was only possible for a disk temperature exceeding the temperatures of both stars, which is most probably not physical[3]. Better quality fits can be obtained if the Roche lobe filling factor of the secondary is allowed to drop below 0.75: we obtained $\chi^2_\nu = 3.9$ for a secondary filling factor of 0.47 (which would correspond to a secondary radius of only 3.9 $R_\odot$) and a disk temperature of 51 300 K. Both parameters (secondary radius and disk temperature) are most probably not physical. We thus conclude that a disk model cannot solve the issues raised above any better than the pure Roche potential model.

Table 8. Fit of the light curves of LSS 3074 by a sine function.

	Filter			
	B	*V*	*R*	*I*
P = 1.0926 d				
$a(P)$	0.0901	0.0910	0.0964	0.0980
σ_a	0.0022	0.0022	0.0039	0.0027
χ^2_ν	5.96	2.92	2.65	2.66
$\sigma_{\rm fit}$	0.0171	0.0171	0.0212	0.0212
P = 2.1852 d				
$a_1(P)$	0.0118	0.0125	0.0107	0.0125
σ_{a_1}	0.0020	0.0020	0.0038	0.0020
$a_2(P/2)$	0.0896	0.0905	0.0958	0.0905
σ_{a_2}	0.0019	0.0019	0.0037	0.0019
χ^2_ν	4.60	2.20	2.38	1.30
$\sigma_{\rm fit}$	0.0150	0.0148	0.0200	0.0148
N	120	122	58	118
σ	0.007	0.010	0.013	0.013

Notes. P is the adopted period, a_i the semi-amplitudes, σ_{a_i} the 1σ error on semi-amplitude, χ^2_ν the minimum reduced χ^2, $\sigma_{\rm fit}$ the rms of the residuals, N the number of points and σ the expected error.

From a purely phenomenological point of view, we can expand the light curve into a sum of sine functions. We tried a period of 2.1852/2 = 1.0926 days and a mere sine and a period of 2.1852 days and the fundamental sine plus its harmonic. The results are given in Table 8. The photometric observations exhibit a variation with a semi-amplitude of 0.09 mag in all filters. The semi-amplitude associated with the modulation on the orbital period is 0.01 mag reflecting the above-mentioned difference between the depths of the two minima. The corresponding χ^2_ν are lower than for any other fit we tried but still not satisfactory. Including a larger number of harmonics in our expansion does not improve the situation. However, in terms of standard binary models, this fit is unphysical since a modulation with a semi-amplitude as large as 0.09 mag cannot be explained by ellipsoidal variations for such models. The fit of the *B* light curve corresponds to a larger χ^2_ν; the corresponding χ^2_ν would be similar to those found for the data from the other filters provided that the photometric errors used to normalize the χ^2_ν were 0.010 mag instead of 0.007 mag.

The χ^2_ν of Table 8 are too large and this anomaly could have several origins. One possibility is that the above-mentioned photometric errors deduced from the comparison stars might not apply to the case of LSS 3074. This could be due to an unfortunate location on the CCDs or for example to strange behaviour due to peculiar stellar colours. This interpretation is however not very likely. Alternatively, the fitted mathematical model might not be correct. Since any periodic function can be expanded into a Fourier series and we found that our sine fits do not require additional terms, the additional, non-periodic component of the model behaves similarly to an observational noise although it must have a different origin. A possible explanation could be an intrinsic variability of the star at high frequencies since no low-frequency variations were previously detected beyond the orbital one. Of course, this additional component has an upper limit. Since the sine fits are our best models, we can consider

---

[3] Raising the disk temperature allows the model to better reproduce the depth of the primary minimum, hence partially compensating for the increase of χ^2 due to the poor fit of the secondary minimum.

estimating this upper limit from the corresponding residuals. In the V filter for instance, we would need an additional variability compared to the expected $\sigma = 0.010$ mag photometric error that quadratically adds to it to reach $\sigma_{\rm fit} = 0.0148$ mag for the two periods fit or $\sigma_{\rm fit} = 0.0171$ mag for the single period fit. Considering that the difference in depth between the two minima is not well established, we can adopt the latter and the relevant value would thus be $\sigma_{\rm fit} = 0.0171$ mag.

The transition from $\sigma = 0.010$ to 0.0171 mag translates into a change from $\sigma = 0.009$ to $\sigma^{\rm corr} = 0.0185$ mag for the global fit of the data from all four filters. The substitution by these newly estimated errors alleviates the rejection of the NIGHTFALL model, since it reduces the χ^2. However, this is purely artificial. In addition, the ${\chi_\nu}^2$ of 4.4 could still be due to a lack of ability of the NIGHTFALL model to fit the light curve, even if it were noiseless. However, under the hypothesis of the fit of the NIGHTFALL model, the errors on the parameters must be modified to remain coherent. Even though this additional dispersion does not stem from the same origin as the genuine photometric errors, impact of this dispersion on the derived parameters is similar to that of photometric errors.

To obtain the 1σ error on the parameters of the NIGHTFALL models, we have to consider the dispersion at $\chi^2_{\rm min} + \Delta\chi^2_{1\sigma}$ where $\Delta\chi^2_{1\sigma} = 2.3$ for the 1σ confidence interval of the simultaneous adjustment of two free parameters (i and $fill_{\rm p} = fill_{\rm s}$ as is the case when we fit the light curve assuming an overcontact configuration with NIGHTFALL). From the values of the χ^2 of our best-fit NIGHTFALL model, the 1σ error bars on the orbital inclination and the filling factors would be unrealistically small (e.g. about 0.1° for the error on i). However, as pointed out above, the dispersion of the photometric data about the best-fit synthetic light curve exceeds the value of our estimated photometric errors, suggesting that there could be an intrinsic photometric variability in addition to the orbital modulation.

Admitting the impact of the additional dispersion, we have to correct the $\Delta\chi^2_{1\sigma} = 2.3$ to take this effect into account. Therefore, we have to adopt a corrected $\Delta\chi^2_{1\sigma,{\rm corr}} = \Delta\chi^2_{1\sigma} \times \left(\frac{\sigma^{\rm corr}}{\sigma}\right)^2 = 8.9$. We have then estimated the errors on the NIGHTFALL model parameters by accordingly adopting this new corrected value. In this way, rounding the values uppards, we estimate errors of 1.0° and of 0.01 for the inclination and the filling factors of both stars, respectively.

8. Spectral analysis

8.1. Rotational velocities and macroturbulence

In order to determine the projected rotational velocities ($v \sin i$) of the stars of the system, we applied a Fourier transform method (Simón-Díaz & Herrero 2007; Gray 2008). For the primary star, we used the profiles of the He I λ4471, He II $\lambda\lambda$ 4200, 4542, 6118, and N III λ6075 lines of the reconstructed spectrum. We selected these lines as they are rather well isolated in the spectra and should thus be free of blends. Unfortunately, we could not use the same lines for the secondary star because they are particularly deformed. Indeed, the red wing of these lines is steeper than the blue wing. We then used the He II λ5412 and Si IV λ4089 lines to determine the projected rotational velocity of the secondary star. The results are presented in Table 9. The mean $v \sin i$ of the primary star is (110 ± 13) km s^{-1}, while that of the secondary is (127 ± 6) km s^{-1}. Owing to the small number of lines usable to study the rotation of the secondary star, we could not use a classical standard deviation method to determine the associated error bars. We thus studied the Fourier transforms for a sample of rotational velocities to estimate these errors. From these values of $v \sin i$ and considering the inclination of the system from Sect. 7, we found that the stars are in synchronous rotation with a rotational period very close to the orbital period of the system.

Table 9. Projected rotational velocities ($v \sin i$ expressed in km s^{-1}) of the components of LSS 3074.

Line	Primary	Secondary
Si IV λ4089	–	126
He II λ 4200	115	–
He I λ4471	97	–
He II λ 4542	119	–
He II λ5412	–	128
N III λ6075	92	–
He II λ6118	125	–
Mean value	110 ± 13	127 ± 6

Macroturbulence is defined as a non-thermal motion in the stellar atmosphere with turbulent cells larger than the mean free-path of the photons. The main effect of macroturbulence is an additional broadening of the spectral lines. An approximation of the macroturbulence velocities was obtained by applying the radial-tangential anisotropic macroturbulent broadening formulation of Gray (2008) on the spectra, after the inclusion of rotational velocity broadening. For this purpose, we used the auxiliary program MACTURB of the stellar spectral synthesis program SPECTRUM v2.76 developed by Gray (2010). We applied this technique to the lines He I $\lambda\lambda$ 4026, 4471, and 5016, and He II λ 4542 and obtained macroturbulence velocities of 20 and 50 km s^{-1}, for the primary and secondary stars, respectively.

Both rotational and macroturbulence velocities were applied on the synthetic spectra (see Sect. 8.2) before comparing the latter with the disentangled spectra.

8.2. CMFGEN code

In order to determine the fundamental properties of both components of LSS 3074, we used the non-LTE model atmosphere code CMFGEN (Hillier & Miller 1998). This code solves the equations of radiative transfer and statistical equilibrium in the co-moving frame, is designed to work for both plane-parallel and spherical geometries, and can be used to model Wolf-Rayet stars, O stars, luminous blue variables and supernovae. A super-level approach is adopted for the resolution of the equations of statistical equilibrium. The CMFGEN code also further accounts for line blanketing and its impact on the energy distribution. The hydrodynamical structure of the stellar atmosphere is directly specified as an input to the code, and a β law is used to describe the velocity law within the stellar winds. We included the following chemical elements and their ions in our calculations: H, He, C, N, O, Ne, Mg, Al, Si, S, Ca, Fe, and Ni. The solution of the equations of statistical equilibrium is used to compute a new photospheric structure, which is then connected to the same β wind velocity law. The radiative transfer equations were solved based on the structure of the atmosphere with a microturbulent velocity varying linearly with wind velocity from 20 km s^{-1} in the photosphere to $0.1 \times v_\infty$ at the outer boundary, and generated synthetic spectra were compared to the reconstructed spectra of the primary and secondary stars.

As a first approximation, the mass-loss rates and β parameters were taken from Muijres et al. (2012) for the spectral types of both stars, whilst the wind terminal velocity was assumed equal to the mean value for stars of the same spectral type (Prinja et al. 1990). We then estimated the surface gravities, stellar masses, radii, and luminosities from our study of the photometric curves. The relevant parameters were then adjusted via an iterative process, as each adjustment of a given parameter leads to some modifications in the value of other parameters. This process and the results we obtained are presented in Sects. 8.3 and 8.4, respectively. As explained in Sect. 6, this iterative process was then coupled with a second iterative process, through the study of the photometric light curve.

8.3. Method

The first step is to adjust the effective temperature in the models of the stars. To do so, we adjusted the relative strengths of the He I λ 4471 and He II λ 4542 lines (Martins 2011). Final values are 39 900 and 34 100 K for the primary and secondary stars, respectively. Once the effective temperatures were determined, we used them, together with the stellar radii obtained in our study of the photometric curves, to constrain the luminosities of the stars. We therefore obtained luminosities of $1.38 \times 10^5\ L_\odot$ and $8.49 \times 10^4\ L_\odot$ for the primary and secondary stars.

Subsequently, the binarity of the studied system causes some problems. Indeed, the next step is to adjust the surface gravities in the models, but as we mentioned in Sect. 6.1, the wings of the Balmer lines are too broad to be properly recovered by the spectral disentangling. To circumvent this problem, we recombined the models of the primary and secondary star spectra for several phases and compared the resulting binary spectra directly to the observations. This permitted us to better adjust the gravities, but with larger uncertainties than in the case of a single star.

A second problem arises with the adjustment of the wind parameters. Indeed, the He II λ 4686 and Balmer lines may be polluted by some emission from the wind-wind interaction zone. Therefore, the uncertainties on the terminal velocity, the β of the velocity law, the clumping factor, the clumping velocity factor, and the mass-loss rate are quite high. Indeed, considering the possible existence of such additional emission polluting these diagnostic lines, the adjustment of the models onto the reconstructed spectra may lead to an underestimate of the terminal velocity, and an overestimate of the β of the velocity law, clumping factor, clumping velocity factor, and mass-loss rate. Therefore, the obtained values can only be considered as lower and upper limits of the real properties of the stellar winds. However, we still adjusted them as well as possible: we obtained for the primary and secondary stars values of 2615 and 3055 km s^{-1} for v_∞, 1.30 and 1.40 for β and 3.00×10^{-6} and $3.51 \times 10^{-6}\ M_\odot\,\mathrm{yr}^{-1}$ for the mass-loss rate, based on the strength of Hα, the width of the He II λ 4686 and Hα lines, and both the strengths of Hγ and Hδ, respectively. The clumping formalism used in the CMFGEN model is

$$f(r) = f_1 + (1 - f_1)\mathrm{e}^{\left(-\frac{V(r)}{f_2}\right)}$$

with a clumping filling factor f_1 of 0.7, a clumping velocity factor f_2 of 200 kms^{-1} and $V(r)$ the velocity of the wind for both primary and secondary stars, and we adjusted these two clumping factors through the strength and shape of Hα and Hβ lines.

Finally, once the fundamental properties of the stars had been established or fixed, we investigated the CNO abundances within their atmosphere through the strengths of associated lines. At that point, we encountered several problems. Indeed, there is no visible O line in both primary and secondary spectra, and the only present C lines are the C IV $\lambda\lambda$ 5801 and 5812 lines, which cannot be considered in the determination of the surface C abundance since they can exhibit complex profiles influenced by various phenomena among which is continuum fluorescence (Conti 1974; Bouret et al. 2012). We thus were only able to determine upper limits for C and O abundances. We used the N III λ 4379 and N III $\lambda\lambda$ 4511-15-18-24-30-35 lines to adjust the N abundance for the primary star. The same lines were used for the secondary star except for the N III λ 4530 and N III λ 4535 lines. These *N* abundance diagnostic lines are taken from Martins et al. (2015) study of a sample of 74 objects comprising all luminosity classes and spectral types from O4 to O9.7. We selected, from their study, all the suggested lines that were significantly seen in our observations. We performed a normalized χ^2 analysis to determine the best fit to these lines (Martins et al. 2015). The normalization consists in dividing the χ^2 by its value at minimum, χ^2_{min}. As a 1σ uncertainty on the abundances, we then considered abundances up to a χ^2 of 2.0, i.e. an approximation for 1 over χ^2_{min}, as suggested by Martins et al. (2015).

8.4. Results

Figure 8 shows the best fit of the optical spectra of the primary and secondary stars obtained with CMFGEN, and we present in Table 10 the associated stellar parameters.

Figure 8 reveals that we encountered a lot of difficulty adjusting the spectra of the components of LSS 3074. First of all, it clearly shows that the noise is strongly enhanced in the reconstructed secondary spectrum, because of the high brightness ratio of the system. This peculiarity makes the adjustment of the secondary spectrum even more difficult. Second, if we can see that the He lines are generally well reproduced for both stars, some of these lines in the observed spectra, especially for the secondary star, feature some emission in their wings that is not reproduced by the models. We can also see that the Balmer and He II λ 4686 lines are not perfectly well recovered, probably owing to the complexity of the winds and the presence of a wind-wind interaction zone, as discussed in Sect. 8.3.

Concerning the N lines, most N III features are reasonably well reproduced by the models, but a few lines of other nitrogen ions are not, especially in the primary spectrum. Indeed, the model predicts a rather strong N IV λ 4058 emission, while the observations clearly show that this is not the case. Another remarkable issue is the presence in the observed primary spectra of the N V $\lambda\lambda$ 4604, 4620 lines, which are not predicted by the model. These N V lines are seen in the spectra of the earliest O supergiants (starting from O4 If Walborn et al. 2002; Sota et al. 2011) and, in some cases, in the spectra of early O main-sequence stars (e.g. Mahy et al. 2012), and could suggest that our value of the primary effective temperature (39 900 K) is too low. To test this hypothesis, we computed a set of CMFGEN models with temperatures ranging from 38 000 to 44 000 K. As one can see in Fig. 7, a temperature of about 44 000 K would be needed to reproduce the strength of the N V lines. However, in this case, the model predicts N III emissions that are much weaker than observed as well as a huge N IV line that is clearly not observed. To reproduce the strength of the observed N III and N IV lines, a lower temperature of 38 000 K seems more indicative. But this lower temperature is clearly not sufficient to produce the N V lines. The temperature that we determined in our CMFGEN fits is the temperature that properly reproduces

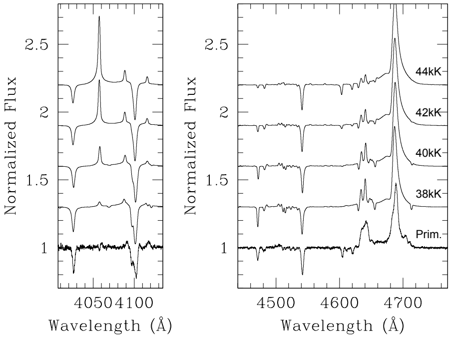

Fig. 7. Evolution of the strength of the N III λλ 4634-41, N IV λ 4058, and N V λλ 4604, 4620 lines in synthetic CMFGEN spectra as a function of effective temperature. The primary spectrum of LSS 3074 obtained via disentangling is shown at the bottom for comparison.

the strength of the helium lines and represents a compromise between the contradicting trends of the nitrogen lines.

Our difficulty in reproducing simultaneously the lines of N III, N IV, and N V in the spectra of O supergiants is actually not new. Crowther et al. (2002) and Rauw et al. (2002) encountered similar problems in their attempts to fit the spectra of the O4 Iaf$^+$ star HDE 269 698 and of the O7 + O4 If/WN8ha binary HDE 228 766, respectively. More recently, Bouret et al. (2012) applied the CMFGEN code to a sample of early O supergiants. These authors also failed to reproduce consistently the lines of the three nitrogen ions in the spectra of the three O4 If supergiants HD 15 570, HD 16 691, and HD 190 429A for which they derived effective temperatures of 38 000, 41 000, and 39 000 K, respectively. We note that these effective temperatures are very close to our best-fit value for the primary of LSS 3074.

The origin of these difficulties is currently unclear. One possibility could be that the models do not account (correctly) for the Auger effect. X-ray emission arising in the wind and back illuminating the stellar photosphere could lead to an overionization of nitrogen and favour the formation of the N V lines. In the specific case of the primary of LSS 3074, the simultaneous presence of the three ionization stages of nitrogen could also be from a non-uniform surface temperature as a result of gravity darkening. Applying the von Zeipel theorem to the primary, we find that the effective temperature near the poles should be about 15% higher than near the equator. The observed spectrum of the primary results from the combination of the spectra emitted by the various regions, which have their own temperatures (Palate & Rauw 2012; Palate et al. 2013). Therefore, gravity darkening could indeed result in a spectrum with an unusual combination of spectral lines.

However, we can stress three very interesting results from our spectral analysis. First of all, as we can see in Table 10, we confirm the very low masses and radii predicted by Morrell & Niemela (1990), which is unusual for stars with such spectral types. We can also see that the system seems to display strong winds, even though these winds are not perfectly constrained. Finally, we found a strong overabundance in N and a strong depletion in C and O in both stars of the system, together with a strong He enrichment of the primary atmosphere.

Table 10. Best-fit CMFGEN model parameters of the primary and secondary stars.

	Prim.	Sec.
R ($R_\odot$)	7.5 ± 0.6	8.2 ± 0.7
M ($M_\odot$)	14.6 ± 2.1	17.2 ± 3.0
$T_{\rm eff}$ (10^4 K)	3.99 ± 0.15	3.41 ± 0.15
$\log(g)$ (cgs)	3.82 ± 0.20	3.83 ± 0.20
$\log\left(\frac{L}{L_\odot}\right)$	5.14 ± 0.07	4.93 ± 0.08
β	$\leq$1.30	$\leq$1.40
v_∞ (km s^{-1})	$\geq$2615	$\geq$3055
$\dot{M}/\sqrt{f_1}$ ($M_\odot$ yr^{-1})	$\leq 3.00 \times 10^{-6}$	$\leq 3.51 \times 10^{-6}$

Notes. The quoted errors correspond to 1σ uncertainties.

Table 11. Chemical abundances of the components of LSS 3074.

	Primary	Secondary	Sun
He/H	0.25	0.09	0.089
C/H	$\leq 6.45 \times 10^{-5}$	$\leq 2.05 \times 10^{-5}$	2.69×10^{-4}
N/H	$5.65^{+4.07}_{-3.02} \times 10^{-4}$	$3.69^{+0.83}_{-0.91} \times 10^{-4}$	6.76×10^{-5}
O/H	$\leq 2.67 \times 10^{-5}$	$\leq 1.00 \times 10^{-5}$	4.90×10^{-4}

Notes. Abundances are given by number as obtained with CMFGEN. The solar abundances (Asplund et al. 2009) are quoted in the last column. The 1σ uncertainty was set to abundances corresponding to a normalized χ^2 of 2.0.

9. Discussion and conclusions

Our analysis of the light curve of LSS 3074 indicates that this system is a candidate for an overcontact binary. Massive overcontact binaries are important objects as they could be progenitors of merger events or of binary black hole systems (Lorenzo et al. 2014; Almeida et al. 2015). Yet, only a handful of such systems are known and sometimes the exact configuration (double contact versus semi-detached) is controversial (e.g. Yaşarsoy & Yakut 2013; and Zhao et al. 2014, respectively). Among the best-studied systems hosting O-type stars are HD 100 213 (=TU Mus, Linder et al. 2007), VFTS 352 (Almeida et al. 2015), and MY Cam (=BD+56°864, Lorenzo et al. 2014). Lorenzo et al. (2014) and Almeida et al. (2015) note that the components of MY Cam and VFTS 352 appear hotter than one would expect from their masses. This discrepancy also exists for LSS 3074 and is even worse than in the other systems. Lorenzo et al. (2014) interpret this result as a consequence of the highly elongated shape of the stars. In the case of VFTS 352, Almeida et al. (2015) further report an enhanced He abundance. These authors interpret this situation as the result of enhanced mixing in a tidally locked binary (de Mink et al. 2009) and suggest that the system is currently in a long-lived overcontact phase of case A mass transfer. Again LSS 3074 also shows abundance anomalies indicating that both stars are evolved (enhanced *N* abundance) and the primary is the more evolved star (enhanced He abundance).

9.1. Evolutionary status

We first remark that we did not consider the possibility of quasi-chemically homogeneous evolution as described in Heger et al. (2000), because the observed rotational velocities of both components are too small.

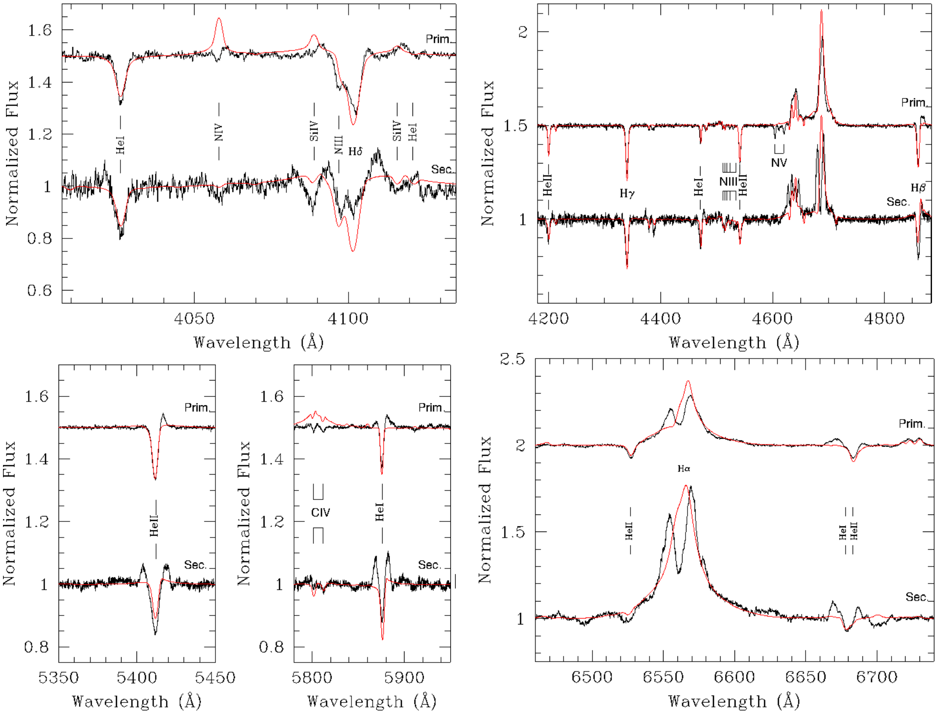

Fig. 8. Part of the normalized separated spectra of the primary (top, shifted upwards by 0.5 continuum units in *the first three panels*, and by 1.0 continuum units for *the last panel*) and secondary stars (bottom), along with the best-fit CMFGEN model spectra (red).

The altered CNO abundances in the atmosphere of the primary, the luminosity of primary, and the increased helium abundance are strong arguments that the star is in the slow phase of case B RLOF. If the star were post-RLOF, accounting for the present mass, its luminosity would have to be log $(\frac{L}{L_{\odot}}) = 5.5$ rather than the observed 5.14 (e.g. Vanbeveren et al. 1998, formula 5.4). Moreover, the observed CNO abundances of the secondary seem to indicate that at least some mass lost by the primary was accreted by the secondary. The normal (solar) helium abundance, on the other hand, lead us to conclude that not all the helium enhanced layers lost by the primary were accreted by the secondary. Accounting for these facts a theoretical study can be undertaken to attempt to identify its possible progenitors. For this purpose, the Brussels binary population synthesis code is used. This code uses as input thousands of detailed evolutionary calculations performed with the Brussels binary evolution code. Both codes are described in detail in De Donder & Vanbeveren (2004). However, the theoretical treatment of binary evolution is still subject to a number of uncertainties, which are typically implemented by means of parameters. For the present discussion, two uncertain aspects of binary mass transfer, characterized in population synthesis by two parameters, are of interest. The first is the fraction of the mass lost by the donor star that is actually accreted by the gainer star. This fraction necessarily lies between zero (i.e. totally non-conservative mass transfer) and one (i.e. totally conservative mass transfer), and is characterized in population synthesis by the parameter $\beta_{\rm RLOF}$[4] (hence $0 \leq \beta_{\rm RLOF} \leq 1$). If $\beta_{\rm RLOF} < 1$, and thus mass is lost from the system, a second critical assumption concerns how much angular momentum is taken along from the system by this lost mass. This is determined by a parameter η (for a formal definition, see De Donder & Vanbeveren 2004). For the present discussion, it suffices to know that the larger η, the more angular momentum is removed from the binary by a given amount of mass loss. A common assumption made in many population synthesis studies is that the mass lost takes along only the specific orbital angular momentum of the gainer star (and thus leaves this star in a spherically symmetric way). This results in a low angular momentum loss, characterized by a low value of $\eta \sim 0.05$. An alternative assumption is that mass is lost through the second Lagrangian point and forms a circumbinary ring, taking along some of the orbital angular momentum of this ring. This entails a much larger angular momentum loss, and has been shown to result in $\eta = 2.3$. Various other, less common assumptions are also possible (e.g. gainer orbital plus spin angular momentum and specific binary angular momentum), which all result in intermediate cases and can be approximated by taking $\eta = 1$. The purpose of this paragraph is to investigate, for various combinations of the

---

[4] The usual designation for this parameter is β, but we used the $\beta_{\rm RLOF}$ designation to avoid any confusion with the β of the velocity law in the stellar winds.

Table 12. Initial masses and orbital period, leading to a 14.8+17.2 $M_{\odot}$, 2.2 d post-RLOF binary for different combinations of β_{RLOF} and η.

	$\beta_{\mathrm{RLOF}} = 1$	$\beta_{\mathrm{RLOF}} = 0.5$	$\beta_{\mathrm{RLOF}} = 0.1$
$\eta = 2.3$	no solution	34+7.9 $M_{\odot}$, 560 d	34+15 $M_{\odot}$, 1000 d
$\eta = 1$	no solution	34+7.9 $M_{\odot}$, 90 d	34+15 $M_{\odot}$, 80 d
$\eta \sim 0.05$	no solution	34+7.9 $M_{\odot}$, 5.3 d	34+15 $M_{\odot}$, 1.4 d

parameters β_{RLOF} and η, whether they can indeed result in the formation of a binary in the slow phase of case B RLOF with the physical parameters (masses and orbital period) of LSS3074, and if so, originating from which initial conditions. All calculations are performed for solar-like metallicity.

Table 12 shows the initial masses and orbital period, depending on the assumed values of β_{RLOF} and η, which produce a 14.8+17.2 $M_{\odot}$ binary in the slow phase of case B RLOF and with an orbital period of 2.2 days.

Our simulations reveal that the primary progenitor was a star with initial mass 30–35 $M_{\odot}$. We find no physically realistic solution if the RLOF is treated conservatively. If it is assumed that $\beta_{\mathrm{RLOF}} = 0.5$, we have to start with an initial 34+7.9 $M_{\odot}$ binary. It is however doubtful that a binary with such an extreme initial mass ratio would avoid merging. Our best guess is then a model with $\beta_{\mathrm{RLOF}} < 0.5$, such as the $\beta_{\mathrm{RLOF}} = 0.1$ model of Table 12. If the matter that leaves the binary takes with it the specific angular momentum of the gainer ($\eta = 0.05$), the initial period of the binary had to be very small (of the order of 1 or 2 days) and this means that the progenitor binary first went through a case A RLOF phase followed by case B. Interestingly, our simulations show that the slow case B RLOF will stop after some 10 000 yr. The primary star then will be a 11–12 $M_{\odot}$ WR star, i.e. the binary will be very similar to the WR binary CQ Cep.

9.2. Summary and conclusions

From what we have seen above, LSS 3074 is clearly a very peculiar binary system that challenges our current methods of binary spectral analysis. In this paper, we have tried to get a deeper understanding of this system, but we encountered a number of problems that prevent us from establishing a fully consistent explanation of all the properties of the system. Here we discuss these problems and try to highlight some avenues for possible solutions.

The properties of the components of LSS 3074 that we determined from our spectral and photometric analysis do not concur with those of genuine early O-type supergiants as determined, for instance, by Bouret et al. (2012). Indeed, these latter authors used the CMFGEN code to analyse UV and optical spectra of typical early and mid-O supergiants. They found that O4-4.5 supergiants have radii between 18.5 and 21.6 $R_{\odot}$, $\log g$ in the range 3.51 to 3.66 and $\log L/L_{\odot}$ between 5.83 and 5.96. For O6-7.5 supergiants, Bouret et al. (2012) determined radii between 20.5 and 21.3 $R_{\odot}$, $\log g$ between 3.41 and 3.54, and $\log L/L_{\odot}$ in the range 5.68 to 5.80. The components of LSS 3074 have significantly smaller radii, which are actually even smaller than the typical radii of early-O main-sequence stars. Stars as big as the supergiants analysed by Bouret et al. (2012) would not fit into such a short-period binary system as LSS 3074, even considering, as we have here, the possibility of an overcontact configuration. The luminosities of the components of LSS 3074 are also far from those determined by Bouret et al. (2012), and are again lower than those of main-sequence stars of the same spectral type. As for the $\log g$ of the stars in LSS 3074, their values are higher than those of genuine supergiants, indicating a more compact stellar atmosphere than for supergiants. The values we found are intermediate between those of giants and main-sequence stars. Last but not least, the masses of the components (14.6 and 17.2 $M_{\odot}$ for the primary and secondary, respectively) are considerably lower than the spectroscopic or evolutionary masses of genuine O supergiants, which are around 50 $M_{\odot}$ for early-O supergiants and around 40 $M_{\odot}$ for mid-O supergiants (Bouret et al. 2012). In fact, the masses that we determined are more compatible with those of O9-B0 main-sequence stars.

Yet, despite these very discrepant stellar properties, the spectrum of the primary star of LSS 3074 is very similar to the spectrum of HD 16 691 (O4 If) analysed by Bouret et al. (2012), including the presence of N V $\lambda\lambda$ 4605-4620 in absorption and the weakness of N IV λ 4058. This situation suggests that the spectra of the LSS 3074 could be biased in some way. Our spectral analysis relies on the individual spectra reconstructed via spectral disentangling. Such a reconstructed spectrum is a brightness-weighted mean over the various parts of the stellar surface that can be observed given the inclination of the system. Owing to the effect of gravity darkening, the temperature at the surface of a rotating star is not uniform: the polar regions that have the higher value of $\log g$ are hotter than the equatorial regions where $\log g$ is lower. Things are even more complicated in a close binary system, where the local acceleration of gravity is determined by the gradient of the Roche potential $\nabla\,\Omega$ (e.g. Palate & Rauw 2012; Palate et al. 2013). To evaluate whether or not this situation leads to a surface gravity that comes close to that of a supergiant, we computed $|\nabla\,\Omega|$ over the surface of the primary star, adopting a Roche lobe filling factor of 1.008. We then compared this value to the acceleration of gravity one would have for a single star of same mass and radius. Except for a small region near the bridge of material that connects both stars, $|\nabla\,\Omega|$ is typically between 3 and 9 times larger than the g value for a single star. Therefore, the Roche potential should lead to an increase of $\log g$ compared to its value if binarity is neglected. Hence, this situation cannot explain the discrepancy between the stellar properties and the observed spectrum. A possible way out could be the effect of the radiation pressure on the potential. Howarth (1997) has shown that radiation pressure leads to a scaling of the potential and a reduction of the local gravity by a factor $1 - \Gamma$, where Γ is a measure of the relative importance of radiation pressure over gravity. The primary star of LSS 3074 could have lost a substantial fraction of its initial mass to the surroundings and, as a result, appears now as a very hot object, significantly hotter than expected from its mass. This assumption is strengthened by the He and CNO primary surface abundances, as shown in Sect. 9.1. Given the high temperature of the components of LSS 3074, the resulting strong radiation pressure appears then to be the best candidate to explain why the stars display unusual spectra.

Another odd feature of LSS 3074 is the discrepancy between the brightness ratios inferred from spectroscopy and photometry. The spectroscopic brightness ratio mainly stems from the weakness of the secondary spectral lines. One possibility could be that these lines are filled in by emission either from the primary star or from circumstellar material. Some evidence for circumstellar emission can be seen in the He I λ 5876 and He II λ 5412 lines of the recontructed spectra, which are flanked by emission wings in the case of the secondary. Yet, it seems unclear whether this effect applies to all spectral lines and would be sufficient to explain the discrepancy between photometry and spectroscopy.

The fact that the light curve of LSS 3074 is actually better fitted by a simple sine function than by the NIGHTFALL model suggests that the components of the binary system might actually be more elongated than expected from the Roche potential. The inclusion of radiation pressure in the calculation of the surface shape can actually lead to systems that are detached whilst they would be in a contact configuration based only on the Roche potential (Drechsel et al. 1995; Palate et al. 2013). Radiation pressure also changes the ellipticity of the stars, making them appear less elongated for a given value of the polar radius (e.g. Fig. 3 Palate et al. 2013), although a further increase in the polar radius could lead to a higher ellipticity whilst preserving a detached configuration (Drechsel et al. 1995). Whilst a detailed modelling of the light curve of LSS 3074, including the effect of radiation pressure, is beyond the scope of the present study, we note that the temperature distribution at the surface of the stars will also be altered and this could possibly help explain the observed light curve. A detached configuration resulting from the effect of radiation pressure could in principle also help bring the photometric and spectroscopic brightness ratios into better agreement.

Acknowledgements. The Liège team acknowledges support from the Fonds de la Recherche Scientifique (F.R.S/FNRS) including especially an F.R.S/FNRS Research Project (T.0100.15), as well as through an ARC grant for Concerted Research Actions financed by the French Community of Belgium (Wallonia-Brussels Federation), and an XMM PRODEX contract (Belspo). We are particularly grateful to Reinhold Haefner for having made his IBVS data available and to Ella Antokhina and Igor Antokhin for discussions on the photometric solution. EG is greatly indebted to Stephanie Wachter and Suzanne Tourtelotte for having spared no pains in facilitating the interaction with the YALO archives. We are grateful to I. Stevens, H. Sana, Y. Nazé, J.-M. Vreux, and M. da Silva Pires for taking some of the spectroscopic data or for discussions on earlier versions of this work. We thank John Hillier for making his code available.

References

Almeida, L. A., Sana, H., de Mink, S. E., et al. 2015, ApJ, 812, 102
Antokhina, E. A., & Kumsiashvili, M. I. 1999, Astron. Lett., 25, 662
Antokhina, E. A., Antokhin, I. I., & Cherepashchuk, A. M. 2013, Astron. Astrophys. Trans., 28, 3
Arnaud, K. A. 1996, in Astronomical Data Analysis Software and Systems V, eds. G. Jacoby, & J. Barnes, ASP Conf. Ser., 101, 17
Asplund, M., Grevesse, N., Sauval, A. J., & Scott, P. 2009, ARA&A, 47, 481
Bohlin, R. C., Savage, B. D., & Drake, J. F. 1978, ApJ, 224, 132
Bouret, J.-C., Hillier, D. J., Lanz, T., & Fullerton, A. W. 2012, A&A, 544, A67
Conti, P. S. 1973, ApJ, 179, 161
Conti, P. S. 1974, ApJ, 187, 539
Conti, P. S., & Alschuler, W. R. 1971, ApJ, 170, 325
Conti, P. S., & Frost, S. A. 1977, ApJ, 212, 728
Crowther, P. A., Hillier, D. J., Evans, C. J., et al. 2002, ApJ, 579, 774
Curcio, J. A., Drummeter, L. F., & Knestrick, G. L. 1964, Appl. Opt., 3, 1401
De Donder, E., & Vanbeveren, D. 2004, New Astron. Rev., 48, 861
de Loore, C., & Vanbeveren, D. 1994, A&A, 292, 463
de Mink, S. E., Pols, O. R., & Hilditch, R. W. 2007, A&A, 467, 1181
de Mink, S. E., Cantiello, M., Langer, N., et al. 2009, A&A, 497, 243
Djurašević, G., Vince, I., Antokhin, I. I., et al. 2012, MNRAS, 420, 3081
Dray, L. M., & Tout, C. A. 2007, MNRAS, 376, 61
Drechsel, H., Haas, S., Lorenz, R., & Gayler, S. 1995, A&A, 294, 723
Eggleton, P. P. 1983, ApJ, 268, 368
González, J. F., & Levato, H. 2006, A&A, 448, 283
Gosset, E., Royer, P., Rauw, G., Manfroid, J., & Vreux, J.-M. 2001, MNRAS, 327, 435
Gosset, E., Rauw, G., Manfroid, J., et al. 2005, Proceedings of Massive Stars and High-Energy Emission in OB Associations, a workshop of the JENAM 2005, Distant Worlds, held in Liège (Belgium), July 4–7, eds. G. Rauw, Y. Nazé, R. Blomme, & E. Gosset, 77
Gray, D. F. 2008, The Observation and Analysis of Stellar Photospheres, 3rd edn. (Cambridge University Press)
Gray, R. O. 2010, `http://www.appstate.edu/~grayro/spectrum/spectrum276/node38.html`
Haefner, R., Simon, K. P., & Fiedler, A. 1994, IBVS, 3969, 1
Heger, A., Langer, N., & Woosley, S. E. 2000, ApJ, 528, 368
Herbig, G. 1995, ARA&A, 33, 19
Hillier, D. J., & Miller, D. L. 1998, ApJ, 496, 407
Horne, K. 1991, in Fundamental Properties of Cataclysmic Variable Stars: 12th North American Workshop on Cataclysmic Variables and Low Mass X-ray Binaries, ed. A. W. Shafter (SDSU Press), 23
Houk, N., & Cowley, A. P. 1975, in University of Michigan Catalogue of two-dimensional spectral types for the HD stars, Vol. I. Declinations –90 to –53°
Howarth, I. D. 1997, The Observatory, 117 335
Hurley, J. R., Tout, C. A., & Pols, O. R. 2002, MNRAS, 329, 897
Jansen, F., Lumb, D., Altieri, B., et al. 2001, A&A, 365, L1
Kaufer, A., Stahl, O., Tubbesing, S., et al. 1999, The Messenger, 95, 8
Kippenhahn, R., & Weigert, A. 1967, Z. Astrophys., 65, 251
Langer, N. 2012, ARA&A, 50, 107
Linder, N., Rauw, G., Sana, H., De Becker, M., & Gosset, E. 2007, A&A, 474, 193
Linder, N., Rauw, G., Martins, F., Sana, H., De Becker, M., & Gosset, E. 2008, A&A, 489, 713
Lorenzo, J., Negueruela, I., Val Baker, A. K. F., et al. 2014, A&A, 572, A110
MacConnell, D. J. 1981, A&AS, 44, 387
Mahy, L. 2011, Ph.D. Thesis, University of Liège, Belgium
Mahy, L., Gosset, E., Sana, H., et al. 2012, A&A, 540, A97
Maíz Apellániz, J., Sota, A., Arias, J. I., et al. 2016, ApJS, 224, 4
Manfroid, J. 1993, A&A, 271, 714
Manfroid, J., Royer, P., Rauw, G., & Gosset, E. 2001, in Astronomical Data Analysis Software and Systems X, eds. F. Harnden, F. Primini, & H. Payne, ASP Conf. Ser., 238, 373
Martins, F. 2011, Bull. Soc. Roy. Sci. Liège, 80, 29
Martins, F., & Plez, B. 2006, A&A, 457, 637
Martins, F., Schaerer, D., & Hillier, D. J. 2005, A&A, 436, 1049
Martins, F., Hervé, A., Bouret, J.-C., et al. 2015, A&A, 575, A34
Mason, B. D., Gies, D. R., Hartkopf, W. I., et al. 1998, AJ, 115, 821
Morrell, N. I., & Niemela, V. S. 1990, in Properties of hot luminous stars, ASP Conf. Ser., 7, 57
Muijres, L. E., Vink, J. S., de Koter, A., Müller, P. E., & Langer, N. 2012, A&A, 537, A37
Nazé, Y. 2009, A&A, 506, 1055
Nazé, Y., Rauw, G., Vreux, J.-M., & De Becker, M. 2004, A&A, 417, 667
Niemela, V. S., Cerruti, M. A., Morrell, N. I., & Luna, H. G. 1992, in Evolutionary Processes in Interacting Binary Stars (Dordrecht Kluwer: Acad. Publ.), 505
Palate, M., & Rauw, G. 2012, A&A, 537, A119
Palate, M., Rauw, G., Koenigsberger, G., & Moreno, E. 2013, A&A, 552, A39
Pigulski, A., & Pojmański, G. 2008, A&A, 477, 917
Podsiadlowski, P., Joss, P. C., & Hsu, J. J. L. 1992, ApJ, 391, 246
Prinja, R. K., Barlow, M. J., & Howarth, I. D. 1990, ApJ, 361, 607
Raucq, F., Rauw, G., Gosset, E., et al. 2016, A&A, 588, A10
Rauw, G. 2007, DSc Thesis, University of Liège, Belgium
Rauw, G., Crowther, P. A., Eenens, P. R. J., Manfroid, J., & Vreux, J.-M. 2002, A&A, 392, 563
Reed, B. C. 2003, AJ, 125, 2531
Richards, M. T., Cocking, A. S., Fisher, J. G., & Conover, M. J. 2014, ApJ, 795, 160
Sana, H., Gosset, E., & Rauw, G. 2006a, MNRAS, 371, 67
Sana, H., Rauw, G., Nazé, Y., Gosset, E., & Vreux, J.-M. 2006b, MNRAS, 372, 661
Sana, H., de Mink, S. E., de Koter, A., et al. 2012, Science, 337, 444
Sana, H., Le Bouquin, J.-B., Lacour, S., et al. 2014, ApJS, 215, 15
Seidensticker, K. J. 1989, A&AS, 79, 61
Seidensticker, K. J., & Schmidt-Kaler, Th. 1989, A&A, 225, 192
Simón-Díaz, S., & Herrero, A. 2007, A&A, 468, 1063
Smith, R. K., Brickhouse, N. S., Liedahl, D. A., & Raymond, J. C. 2001, ApJ, 556, L91
Sota, A., Maíz Apellániz, J., Walborn, N. R., et al. 2011, ApJS, 193, 24
Sota, A., Maíz Apellániz, J., Morrell, N. I., et al. 2014, ApJS, 211, 10
Stetson, P. B. 1987, PASP, 99, 191
Strüder, L., Briel, U., Dennerl, K., et al. 2001, A&A, 365, L18
Turner, M. J. L., Abbey, A., Arnaud, M., et al. 2001, A&A 365, L27
Underhill, A. B. 1995, ApJS, 100, 433
Vanbeveren, D., de Loore, C., Van Rensbergen, W. 1998, A&ARv, 9, 63
van der Hucht, K. A. 1996, in Wolf-Rayet stars in the framework of stellar evolution, Liège International Astrophysical Colloquium, 33, eds. J.-M. Vreux, A. Detal, D. Fraipont-Caro, E. Gosset, & G. Rauw, 1
Walborn, N. R. 2001, in Eta Carinae and Other Mysterious Stars: The hidden opportunities of emission spectroscopy, eds. T. R. Gull, S. Johannson, & K. Davidson, ASP Conf. Ser., 242, 217
Walborn, N. R., Howarth, I. D., Lennon, D. J., et al. 2002, AJ, 123, 2754
Wellstein, S., Langer, N., & Braun, H. 2001, A&A, 369, 939
Wilms, J., Allen, A., & McCray, R. 2000, ApJ, 542, 914
Wilson, R. E. 1974, ApJ, 189, 319
Yaşarsoy, B., & Yakut, K. 2013, AJ, 145, 9
Zhao, E., Qian, S., Li, L., et al. 2014, New Astron., 26, 112

Appendix A

During the above-mentioned iterative process to derive the equivalent of global differential magnitudes (see Sect. 2.2), a few stars were rejected owing to suspected variability. Two stars turned out to be significantly variable: they are analysed here below.

A.1 HD 116827 ≡ CPD -61° 3706

HD 116827 is known to have Hα in emission and is thus classified as a Be star (MacConnell 1981). The Hβ line also presents a weak emission within the absorption profile; the spectral type is B2Ve-B5Ve as derived by Houk & Cowley (1975). Pigulski & Pojmański (2008) observed it in photometry as part of the ASAS-3 endeavour and reported the presence of two pulsation modes with periods 0.22429 d and 0.45217 d; they concluded to a β Cep nature for this object. We confirm the variable nature of this star and the magnitudes measured in the framework of the present work are given in Table A.2, available at the CDS. These magnitudes have been analysed using the same multi-frequency Fourier methods as referred to in the main text. For each filter, we decomposed the light curve into deterministic processes considering up to three frequencies and an additional white-noise process. The dominant frequency peaks are $\nu = 2.312, 4.455, 3.349\,\mathrm{d}^{-1}$ for the B bandpass (semi-amplitudes 0.013, 0.012, and 0.012, respectively), $\nu = 1.210$, 2.213, and $4.458\,\mathrm{d}^{-1}$ for the V bandpass (semi-amplitudes 0.012, 0.011, and 0.010, respectively), $\nu = 4.761$, 2.236, and $1.235\,\mathrm{d}^{-1}$ for the R bandpass (semi-amplitudes 0.012, 0.011, and 0.010, respectively), and, finally, $\nu = 1.288$, 2.287, and $4.492\,\mathrm{d}^{-1}$ for the I bandpass (semi-amplitudes 0.020, 0.019, and 0.018, respectively). Considering that the one-day aliasing remains strong in the sample, we conclude that the dominant frequencies for the different bandpasses could in some cases share the same single origin. No frequency other than the dominant frequencies seems to present some ubiquity among the various filters, indicating that we are nearing the noise level. We removed the mean magnitude from each dataset and merged the four light curves aiming at decreasing the noise. The corresponding Fourier (semi-amplitude) periodogram is given in Fig. A.1. Four main frequency peaks can be spotted at $\nu = 2.286\,\mathrm{d}^{-1}$ (semi-amplitude 0.013), $\nu = 1.286\,\mathrm{d}^{-1}$ (semi-amplitude 0.011), $\nu = 3.319\,\mathrm{d}^{-1}$ (semi-amplitude 0.011), and $\nu = 4.355\,\mathrm{d}^{-1}$ (semi-amplitude 0.010). The one-day alias makes no doubt and we should be careful while making such a list. We also analysed the global data with the multi-frequency method introduced by Gosset et al. (2001). Two independent frequencies were found to be $\nu = 2.286\,\mathrm{d}^{-1}$ (semi-amplitude 0.014) and $\nu = 4.493\,\mathrm{d}^{-1}$ (semi-amplitude 0.014), but no other significant frequency can be spotted. The two derived independent frequencies are strongly reminiscent of those reported on the basis of the ASAS-3 photometry ($\nu = 4.459\,\mathrm{d}^{-1}$ and $\nu = 2.212\,\mathrm{d}^{-1}$), particularly taking into account the $0.03\,\mathrm{d}^{-1}$ aliasing.

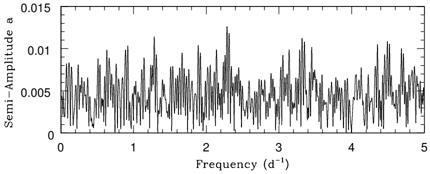

Fig. A.1. Fourier (semi-amplitude) periodogram for HD 116827.

A.2 LSS3072 ≡ CPD -61° 3692

This object appears in the catalogue of OB stars of Reed (2003) and is classified as O9. The magnitudes measured in the framework of the present work are given in Table A.3, available at the CDS. It is clearly variable and the light curve is plotted against time in Fig. A.2. A search for periods results in the detection of the possible frequency $\nu = 0.1092\,\mathrm{d}^{-1}$ ($P = 9.16$ d) for each of the four bandpasses and for the combined data (semi-amplitude 0.023 mag in B, 0.023 in V, 0.024 in R and 0.023 in I). Two bumps are clearly present in Fig. A.2. A few discrepant data points are present at HJD 2 451 999.71 and at HJD 2 452 027.54. The deletion of these data points does not change the result of the period search. However, it is worth noticing that they are separated by some three entire cycles and could thus be related to the possible main period. We have no particular reason to reject these possible outliers.

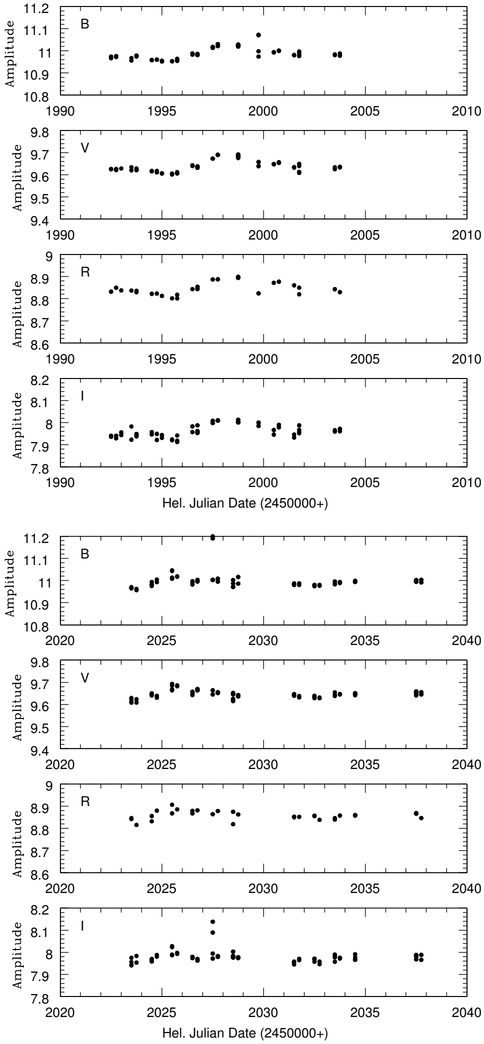

Fig. A.2. Light curve of LSS 3072.

3.3.1 Comparison with single-star evolutionary models

As we have shown in Raucq et al. (2017), the spectra of both components of LSS 3074 display the signature of some abundance modifications in CNO. In Fig. 3.2, we compare our inferred N/O and N/C ratios with the predictions from the Geneva evolution models of single massive stars of different masses (Ekström et al. 2012), either without rotation (left panel) or with a rotational velocity of $0.4 \times v_{\rm crit}$ (right panel). Since we were only able to obtain upper limits for the C and O abundances in our analysis (see Raucq et al. 2017, Sect. 8.3), the obtained N/C and N/O ratios can only be considered as lower limits of the real abundances in the stellar atmospheres of the components of LSS 3074. The lower error bars for these limits are determined from the lower error bars of the N abundances (see Raucq et al. 2017, Table 11).

The figure clearly shows that, considering the spectroscopic masses of 14.6 and 17.2 $M_\odot$ obtained in our analysis for the primary and secondary stars respectively, these models cannot account for the observed CNO abundance patterns. Indeed, if we compare our results to the models without any rotation (left panel of Fig. 3.2), there is no chemical enrichment expected over the duration of the main-sequence evolutionary phase for stars with masses < 60 $M_\odot$. Surface chemical abundances in CNO only begin to change for models of stars with masses > 60 $M_\odot$, when the loss of material through the stellar wind is sufficient to reveal the products of the CNO cycle at the surface before the end of the main-sequence evolution.

On the other hand, if we consider the models including an initial rotational velocity of $0.4 \times v_{\rm crit}$ (Fig. 3.2, right panel), the CNO abundance patterns of both primary and secondary atmospheres may only be explained by single star evolution if we consider stars with initial masses of 60 $M_\odot$. Following these models, the surface abundances of a single star of 60 $M_\odot$ initial mass reach the values observed for the primary and secondary stars with a current mass of about 45 $M_\odot$, while the spectroscopic masses of both stars are 14.6 and 17.2 $M_\odot$ respectively[1].

Figure 3.3 represents the positions of the primary (empty square) and secondary stars (filled squares) in the Hertzsprung-Russel diagram (HRD; upper panels) and in the $\log g$-$\log T_{\rm eff}$ diagram (lower panels), along with the evolutionary tracks from Ekström et al. (2012) for the core hydrogen burning phase of single stars at solar metallicity, both for non-rotating (left panels) and rotating stars (right panels). This figure illustrates once

---

[1] In the specific case of LSS 3074, the spectroscopic masses of the primary and secondary stars (14.6 and 17.2 $M_\odot$, respectively) obtained with the CMFGEN code are almost identical to the dynamical masses obtained from the photometric solution (14.8 and 17.2 $M_\odot$, respectively).

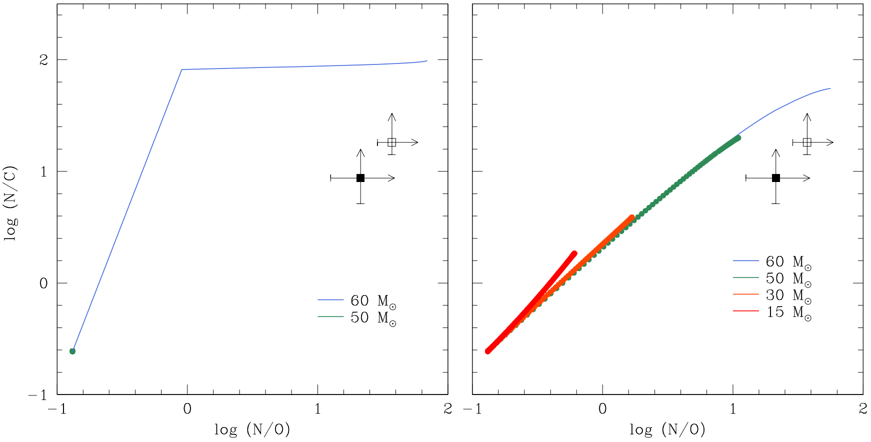

Figure 3.2: Comparison of the N/C and N/O ratios determined from our spectral analyses with predictions from single-star evolutionary models of different masses (Ekström et al. 2012). The primary and secondary stars are shown by the filled and open square symbols, respectively. The left panel illustrates the results for core hydrogen-burning phase tracks without stellar rotation, whilst the right panel corresponds to the same tracks for stars rotating at 0.4 × v_{crit}. Since the C and O abundances determined from our analysis are only upper limits, the obtained N/C and N/O ratios represent lower limits, which is indicated by the arrows on the figure. The lower error bars of the N abundances permitted us to determine a lower error bar to these limits.

again that the single star evolutionary models fail to explain the current properties of the components of LSS 3074.

Indeed, we can see in the HRD that, considering both the non-rotating and 40% critical rotation cases, the properties of the primary star can only be explained by models of initial mass close to 32 $M_\odot$, which is a factor two larger than the current spectroscopic mass of the primary (14.6 $M_\odot$). Concerning the secondary star, models of initial mass between 20 to 25 $M_\odot$ could explain the current properties of the secondary component, while the obtained spectroscopic mass is 17.2 $M_\odot$.

In the $\log g$-$\log T_{\rm eff}$ diagram, we can see that the primary star displays properties close to what is expected for stars of initial mass of 50 $M_\odot$ for the non-rotating case and of 40 $M_\odot$ for the rotating case, while the secondary star shows parameters close to a 25 $M_\odot$ star in both cases.

In both diagrams, we can thus see that both the luminosity and the $T_{\rm eff}$ of both components of LSS 3074 are larger than what is expected for stars of such spectroscopic masses, either considering a non-rotating star or a star rotating at 40% of its critical velocity.

Finally, in all the cases, we also note that the two components of LSS 3074 are not located on the same isochrone, although one would expect them to have the same age.

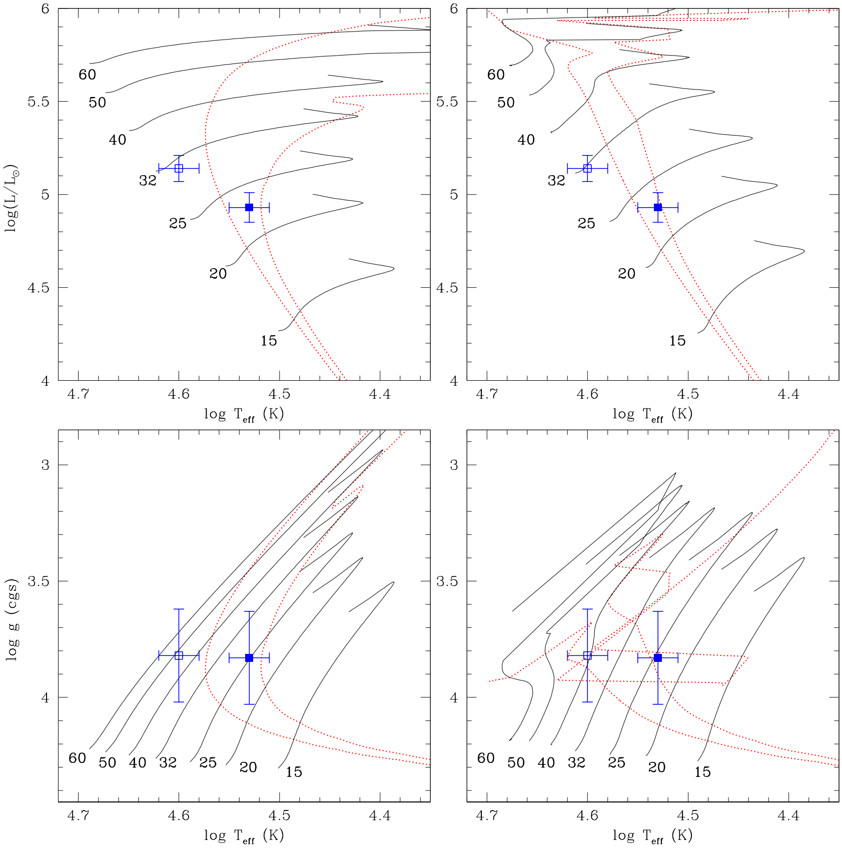

Figure 3.3: Position of the primary (empty square) and secondary (filled square) stars of LSS 3074 in the Hertzsprung-Russell diagram (upper panels) and the $\log g$-$\log T_{\rm eff}$ diagram (lower panels) along with evolutionary tracks for single massive stars at solar metallicity during the core-hydrogen burning phase (Ekström et al. 2012). In the left panels, the evolutionary tracks correspond to non-rotating stars, whilst the right panels yield the results for stars rotating at $0.4 \times v_{crit}$. The dotted red lines correspond to isochrones of 3.2 and 5.0 million years.

We can conclude, from the analysis of Fig. 3.2 and Fig. 3.3, that the system LSS 3074 has been, and may still be, significantly affected by binary interaction, and that both stars have probably lost a significant amount of matter.

3.3.2 SB1 orbital solution

We presented in Raucq et al. (2017) the orbital solution of LSS 3074 (see Sect. 4 of the paper, presented here-before). We also showed that the RVs of the N emission and absorption lines in the spectrum of LSS 3074 seem to move along with the primary, with a rather large scatter of velocities of the various RVs, especially at phases between 0.25 quadrature and 0.5 conjunction (see Fig. 3 of Raucq et al. 2017).

To complement our study of the behaviour of these nitrogen lines, we performed four SB1 orbital solutions based on the N III $\lambda\lambda$ 4634 and 4641 emission lines, N III λ 4379 absorption line, N IV λ 4058 line and N V $\lambda\lambda$ 4604 and 4620 lines respectively. A comparison between these SB1 solutions and the SB2 orbital solution of the system is presented in Table 3.2, and the corresponding RV curves are shown in Fig. 3.4. The orange stars and purple squares represent the measured values of the RVs of N IV λ 4058 and N III λ 4379 lines, respectively, and the orange and purple curves show the corresponding SB1 orbital solutions. The red curve represents the SB1 orbital solution obtained with the RVs of the N III $\lambda\lambda$ 4634 (filled triangles) and 4641 (open triangles) lines, and the blue curve displays the SB1 orbital solution based on the RVs of the N V $\lambda\lambda$ 4604 (filled circles) and 4620 (open circles) lines. The black dashed curve shows the primary curve of the SB2 orbital solution presented in Raucq et al. (2017). To perform these orbital solutions, we used the Liège Orbital Solution Package (LOSP) program (Sana et al. 2009, and references therein), and we weighted the RVs according to their estimated uncertainties.

This study of the nitrogen lines confirmed that most of these lines seem to be produced by the primary star. We can see here that the curves corresponding to all of the N lines are in phase with the general primary SB2 curve, considering that they display the same T_0, within the error bars. This indicates that they are indeed produced by the primary star. Moreover, the curves corresponding to the N III absorption lines and the N IV and N V lines have the same amplitude than the general primary SB2 curve, which suggests that they are produced in the same zone of the primary atmosphere than the other absorption lines that we considered for the general orbital solution (see Raucq et al. 2017, Sect. 4). On the other hand, the larger amplitude of the velocity curve associated to the N III emission lines suggests that these lines are mainly produced over parts of the primary's atmosphere opposite to the secondary star.

Table 3.2: SB1 orbital solution computed from the mean RV of the N lines in the spectra of LSS 3074, assuming a circular orbit and an orbital period of 2.1852 days, compared to the SB2 orbital solution presented in Raucq et al. (2017).

	This study		
	N III emission lines	N III absorption lines	N IV lines
T_0 (HJD - 2 450 000)	2000.990 ± 0.010	2000.833 ± 0.011	2000.821 ± 0.061
γ (km s^{-1})	-2.3 ± 4.7	-68.7 ± 5.9	-0.6 ± 31.1
K (km s^{-1})	278.5± 5.9	242.8± 13.8	229.1± 68.5
$a \sin i$ (R$_\odot$)	12.0 ± 0.3	10.5 ± 0.6	9.9 ± 3.0
$f(m)$ (M$_\odot$)	4.9 ± 0.3	3.2 ± 0.6	2.7 ± 2.4

	This study	Raucq et al. (2017)	
	N V lines	Primary	Secondary
T_0 (HJD - 2 450 000)	2000.893 ± 0.008	2000.851 ± 0.008	
γ (km s^{-1})	-22.4 ± 3.1	-66.0 ± 5.0	-21.7 ± 4.7
K (km s^{-1})	229.9± 3.9	228.5 ± 7.1	196.0 ± 6.1
$a \sin i$ (R$_\odot$)	9.9 ± 0.2	9.9 ± 0.3	8.5 ± 0.3
$f(m)$ (M$_\odot$)	2.8 ± 0.1	2.7 ± 1.1	1.7 ± 0.7

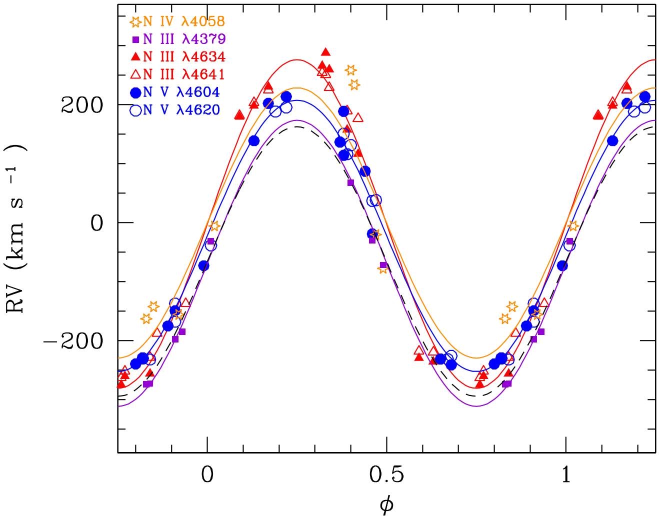

Figure 3.4: The orange stars and purple squares represent the measured values of the RVs of N IV λ 4058 and N III λ 4379 lines, respectively, and the orange and purple curves show the corresponding SB1 orbital solutions. The red curve represents the SB1 orbital solution based on the RVs of the N III $\lambda\lambda$ 4634 (filled triangles) and 4641 (open triangles) lines. The blue curve represents the SB1 orbital solution based on the RVs of the N V $\lambda\lambda$ 4604 (filled circles) and 4620 (open circles) lines. The black dashed curve represents the RV curve of the primary star in the SB2 orbital solution presented in Raucq et al. (2017).

3.4 HD 17505

3.4.1 Introduction

HD 17505 is an O-star system dominating the center of the cluster IC 1848, within the Cas OB6 stellar association. The Cas OB6 region is located in the Perseus arm of the Galaxy, at a distance of about 2.3 kpc (Garmany & Stencel 1992; Massey et al. 1995), revised by Hillwig et al. (2006) to 1.9 kpc. The open cluster IC 1848 (OCL 364) is located in the eastern part of the association. Its primary source of ionizing flux seems to be HD 17505 (Stickland & Lloyd 2001).

Previous studies suggested that HD 17505 is a multiple system with at least four O stars (with a total mass close to 100 $M_\odot$) that are apparently gravitationally bound (Stickland & Lloyd 2001; Hillwig et al. 2006 and references therein), and up to six visual companions that have not been shown to be gravitationally bound (Mason et al. 1998), at distances ranging from 2".1 to 124".0. Walborn (2002) suggested that the multiplicity of the star is the reason it appears so bright in the HRD. The inner binary (HD 17505Aa, see Hillwig et al. 2006) is composed of two massive O7.5V stars, with a short orbital period of P = 8.5710 ± 0.0008 days, two reasons that made it a good candidate for our study of possible past RLOF episodes in massive binaries. The inner binary spectra are also influenced by the third component (HD 17505Ab), which is an O6.5III with an orbital period of < 61 years (Hillwig et al. 2006). This star is the hottest and the brightest of the inner triple system, and its spectral type is similar to the one previously assigned to the entire system (Walborn 1972). The period of the fourth companion around the inner triple is much longer (~27 000 years), with an angular separation of 2".15 from the inner triple system, and this star is much less luminous than the components of the triple system (Perryman 1997 estimated a magnitude difference of $\Delta H_P = 1.66$ mag). Considering the seeing of 2" of the TIGRE telescope, we calculated the fraction of the flux of the fourth companion entering the fiber of the HEROS spectrograph, compared to the flux of the inner triple system. This is illustrated on Fig. 3.5. We thus see that the contribution of the fourth companion to the total flux is negligible: 2.1%.

In this study, we determined the fundamental parameters of the stars of the inner binary of HD 17505 through a set of several analysis techniques. The data used in our study are presented in Sect. 3.4.2. In Sect. 3.4.3 we present a revised orbital solution for this inner binary system. The preparatory treatment of our data, including the disentangling of the spectra of the binary system to reconstruct individual spectra of the binary components, is presented in Sect. 3.4.4, followed by the spectral analysis performed with the non-LTE model atmosphere code CMFGEN

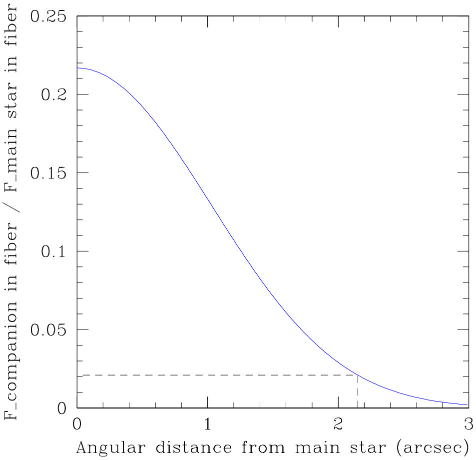

Figure 3.5: Fraction of flux of the fourth component entering the fiber compared to the flux of the inner triple system of HD 17505.

in Sect. 3.4.5. Finally, we discuss the results of our study of HD 17505 in Sect. 3.4.6.

3.4.2 Observations and data reduction

Fifteen high-resolution optical spectra of HD 17505 were obtained with the HEROS spectrograph, mounted on the 1.2 m TIGRE telescope at La Luz Observatory (Mexico; Schmitt et al. 2014), between the 26th of August 2014 and the 25th of October 2014. The HEROS spectrograph covers two spectral domains, ranging from 3500 to 5600 Å (the blue channel) and from 5800 to 8800 Å (red channel), with a resolution of ∼20 000. The spectra were automatically reduced with an Interactive Data Language (IDL) pipeline based on the reduction package REDUCE written by Piskunov & Valenti (2002; see Schmitt et al. 2014).

We also collected one reduced spectrum from the ELODIE archive and a set of six medium-resolution reduced spectra from the FIES archive. The ELODIE échelle spectrograph was mounted on the 1.93 m telescope at the Observatoire de Haute Provence (OHP, France) from 1993 to 2006, and covered the spectral range from 3850 to 6800 Å with a resolution of∼42 000. The FIES échelle spectrograph is mounted on the 2.5 m Nordic Optical Telescope (NOT) located at the Observatorio del Roque de los Muchachos (La Palma, Spain). It covers the spectral range from 3700 to 7300 Å with a resolution of ∼46 000 in medium-resolution mode.

The journal of the observations is presented in Table 3.3.

Table 3.3: Journal of the spectra of HD 17505.

HJD -2 450 000	Instrument	Exp. time (min)	ϕ	RV_1	RV_2 ($km\,s^{-1}$)	RV_3
3327.473	ELODIE	60	0.75	-191.0	114,3	-31.3
5447.762	FIES	15	0.19	115,5	-193,3	-31.7
5577.414	FIES	13.7	0.32	90,8	-163,3	-1.15:
5812.692	FIES	11.8	0.78	-208,3	113.0	-13.6:
5814.677	FIES	9.2	0.01	-28,1	-28,1	-13.6:
5816.755	FIES	8.3	0.25	106,3	-200,4	-13.6:
6285.436	FIES	15	0.95	-128,1	43,0	9.1:
6895.965	HEROS	60	0.20	126,2	-160,5	-37.6
6897.853	HEROS	60	0.42	36,3:	-88,5:	-37.6
6907.940	HEROS	60	0.60	-36,1	-4,1:	-37.6
6910.888	HEROS	40	0.94	-136,1	80,5	-37.6
6911.915	HEROS	60	0.06	-38,2	-38,2	-37.6
6918.869	HEROS	60	0.88	-168,5	126,3	-37.6
6925.891	HEROS	60	0.69	-127,1:	94,7	-37.6
6939.829	HEROS	60	0.32	139,1	-152,3	-37.6
6941.814	HEROS	60	0.55	-28,2	-28,2	-37.6
6943.801	HEROS	60	0.79	-171,4	136,1	-37.6
6945.770	HEROS	60	0.01	-26,4	-26,4	-37.6
6947.861	HEROS	60	0.26	144,8	-166,1	-37.6
6949.855	HEROS	20	0.49	-21,8	-21,8	-37.6
6953.787	HEROS	20	0.95	-126,8	85,6	-37.6
6955.785	HEROS	60	0.18	128,8	-142,9	-37.6

The phases (ϕ) are computed according to the ephemerides listed in Table 3.4. The radial velocities are presented in Sect. 3.4.3. The typical uncertainties on the RVs are $5 - 15$ km s^{-1}. The colons indicate uncertainties larger than 20 km s^{-1}. For the third component, we calculated the mean value of the RVs over each run of observations, given its large orbital period ($<$ 61 years) around the inner binary system.

3.4.3 New orbital solution

From our set of observations, we determined a revised orbital solution of the inner binary system of HD 17505. To do so, we have concentrated our efforts on the strongest absorption lines that are essentially free from blends with other features. In this way, we have measured the RVs of the Hγ, He I $\lambda\lambda$ 4026, 4471, 5876, and 7065 and He II $\lambda\lambda$ 4542, and 5412 lines by a multi-Gaussian fit in the observed spectra. We adopted the effective wavelengths of Underhill (1995). For each observation, the RVs of the primary and secondary stars were determined as the mean of the corresponding RVs measured for each of the above-listed lines in that given observation.

These resulting RVs are listed in Table 3.3. For most data points, the uncertainties on these RVs are about 5-15 km s^{-1}. In some cases however (indicated by the colons in Table 3.3), the uncertainties are larger than 20 km s^{-1}. We adopted the same notations as Hillwig et al. (2006) to refer to the primary and secondary stars. We note that both stars seem to have the same spectral types, thereby leading to some difficulties to distinguish the two stars.

We then performed a Fourier analysis of the RV_1 and RV_2 data, that yielded a highest peak around $\nu = 0.1167$ d^{-1}, i.e. $P_{\rm orb} = 8.5690$ days, which is very close to the orbital period determined in the previous study of Hillwig et al. (2006; $P_{\rm orb} = 8.5710 \pm 0.0008$ days). For completeness, we also performed the same Fourier analysis with our RVs combined to those measured by Hillwig et al. (2006) and obtained a highest peak around $\nu = 0.1167$ d^{-1} as well, suggesting that our period determination is consistent with their work.

Adopting an orbital period of 8.5690 days, we thus computed an orbital solution with the LOSP code (Sana et al. 2009, and references therein) assuming an eccentric orbit, since the previous orbital solution of Hillwig et al. (2006) indicated an eccentricity of 0.095 ± 0.011. The RVs were weighted according to their estimated uncertainties. The result is shown in Fig. 3.6 (upper panel) and the corresponding orbital elements are provided in Table 3.4. We also computed an orbital solution based on both our measured RVs with those measured by Hillwig et al. (2006). The result is shown in Fig. 3.6 (lower panel) and the corresponding orbital elements are also given in Table 3.4.

The RV amplitudes of both our single and combined solutions are lower than values from previous works ($K_1 = 166.5$ and $K_2 = 170.8$ km s^{-1}, Hillwig et al. 2006), and our determined eccentricities are slightly higher than the one they found: 0.128 and 0.118 vs 0.095. The minimum masses that we determined are also significantly lower than what Hillwig et al. found: 11.7 and 12.5 $M_\odot$ for the primary and secondary stars respectively in our solution based on our measurements, 14.6 and 14.8 $M_\odot$ for the primary and secondary stars respectively in our combined solution, and 17.1 and 16.6 $M_\odot$ in Hillwig et al. 2006). These significant differences in the minimum masses come from the differences in RV amplitude in the different orbital solutions.

Table 3.4: Orbital solution of the inner binary computed from our RV data of HD 17505, assuming an eccentric orbit and a period of 8.5690 days, compared to the orbital solution proposed by Hillwig et al. (2006) and an orbital solution obtained by combining our RVs with those measured by these authors.

	This study		Combined solution	
	Primary	Secondary	Primary	Secondary
T_0 (HJD - 2 450 000)	3329.656 ± 0.313		3328.910 ± 0.173	
e	0.128± 0.037		0.118± 0.018	
γ ($\mathrm{km\,s^{-1}}$)	-27.8 ± 4.7	-27.6 ± 4.5	-27.7 ± 2.3	-25.9 ± 2.3
K ($\mathrm{km\,s^{-1}}$)	156.7 ± 6.3	146.7 ± 5.9	162.8 ± 3.2	160.8 ± 3.1
$a \sin i$ ($\mathrm{R}_\odot$)	26.3 ± 1.0	24.6 ± 1.0	27.4 ± 0.5	27.0 ± 0.5
$q = m_1/m_2$	0.94 ± 0.05		0.99 ± 0.02	
ω (°)	257.4 ± 14.0		271.5 ± 7.5	
$m \sin^3 i$ ($\mathrm{M}_\odot$)	11.7 ± 1.2	12.5 ± 1.3	14.6 ± 0.7	14.8 ± 0.8
$R_{\mathrm{RL}}/(a_1 + a_2)$	0.37 ± 0.01	0.38 ± 0.01	0.38 ± 0.01	0.38 ± 0.01
$R_{\mathrm{RL}} \sin i$	19.0 ± 0.6	19.6 ± 0.6	20.6 ± 0.3	20.7 ± 0.3
σ_{fit}	3.18		1.86	

	Hillwig et al. (2006)	
	Primary	Secondary
T_0 (HJD - 2 450 000)	1862.696 ± 0.016	
e	0.095± 0.011	
γ ($\mathrm{km\,s^{-1}}$)	-25.8 ± 1.8	-26.3 ± 1.2
K ($\mathrm{km\,s^{-1}}$)	166.5 ± 1.8	170.8 ± 1.8
$a \sin i$ ($\mathrm{R}_\odot$)	56.8 ± 0.4	
$q = m_1/m_2$	1.03 ± 0.02	
ω (°)	252 ± 6	
$m \sin^3 i$ ($\mathrm{M}_\odot$)	17.1 ± 0.6	16.6 ± 0.6

T_0 refers to the time of conjunction with the primary being in front. γ, K and a sin$i$ denote respectively the apparent systemic velocity, the semi-amplitude of the radial velocity curve and the projected separation between the centre of the star and the centre of mass of the binary system. R_{RL} stands for the radius of a sphere with a volume equal to that of the Roche lobe computed according to the formula of Eggleton (1983). All error bars indicate 1σ uncertainties.

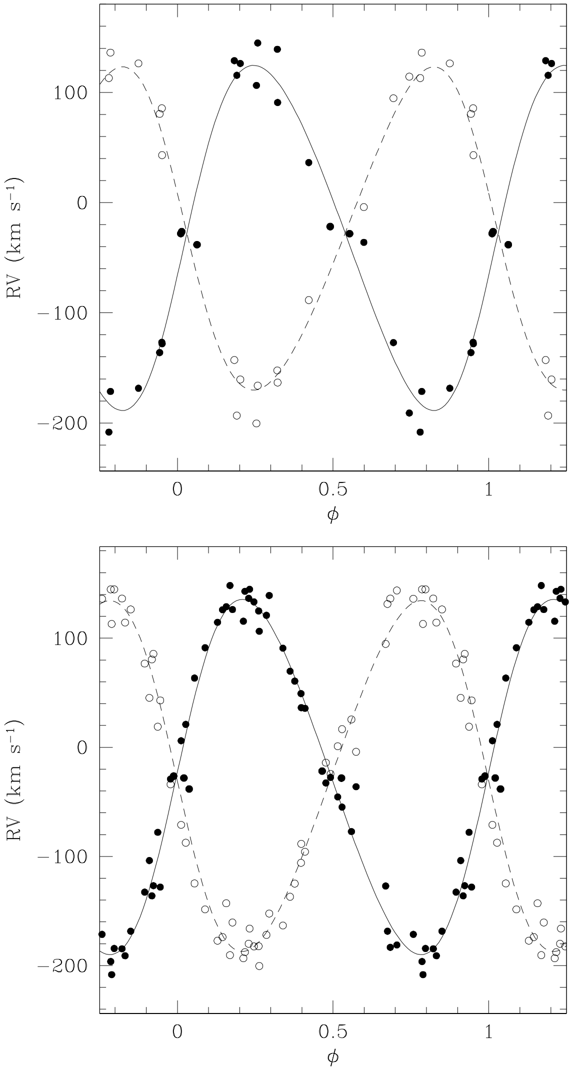

Figure 3.6: Radial velocities of the components of the inner binary of HD 17505, assuming a period of 8.5690 days. The upper panel shows the RVs corresponding to the measurements taken for this study, while the lower panel displays the solution obtained by combining our measurements with those taken by Hillwig et al. (2006). The RVs of the primary and secondary stars are shown with the filled and empty circles, respectively. The solid and dashed lines indicate the orbital solutions from Table 3.4.

3.4.4 Preparatory analysis

3.4.4.1 Adjustment of the ternary spectra and spectral disentangling

Once the orbital solution of the inner binary had been determined, the natural step to follow would have been to disentangle the spectra of the three components of the central object of HD 17505, the triple system HD 17505A, considering a non-moving tertiary object, which is a rather good approximation since the orbital period of the third star around the inner binary is very large ($<$ 61 years) compared to the time span of the observations. However, when we applied our disentangling routine adapted to triple systems (see the end of Sect. 2.1.1), we observed the appearance of artefacts in the resulting reconstructed primary, secondary and tertiary spectra. Indeed, as we can see on Fig. 3.7, the wings of broad features in the resulting tertiary spectrum appear in emission, with a general profile very similar to a mirrored profile of the wings of the corresponding lines in the primary and secondary spectra.

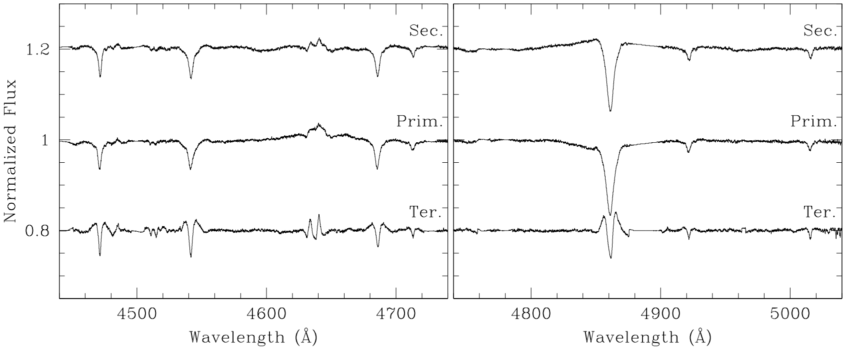

Figure 3.7: Parts of the reconstructed spectra of the primary (middle), secondary (top, shifted upwards by 0.2 continuum units) and tertiary (bottom, shifted downwards by 0.2 continuum units) stars after an attempt of spectral disentangling of the triple system.

The appearance of such artefacts may be due to the method used in the disentangling code itself. Indeed, this method is based on the Doppler shift of the lines associated to the different components of a system due to their motion along their orbit. In this particular triple system, it causes some problems because the lines of the third object are located between the lines of the other two stars at every observed phase. This peculiarity, combined with the RV amplitudes of the primary and secondary stars and the broadening of the respective lines of the three objects due to rotational velocities and macroturbulence, implies that the wings of the lines of the tertiary star are always partially blended with the neighbouring wings of the corresponding lines of the primary and secondary stars. The disentangling code thus encounters problems to interpret the behaviour of these wings, and produces artefacts during its calculation.

To circumvent this problem, we used the same method as for the IUE spectra of HD 149404, in Sect. 4.4 of Raucq et al. (2016). We recombined synthetic spectra of each component of HD 17505A, shifted by the appropriate RVs for every observations, and compared the obtained synthetic ternary spectrum to the observations of the system.

To constrain the fundamental physical parameters of each component of the inner triple system of HD 17505, we used the non-LTE model atmosphere code CMFGEN, described in Sect. 2.2. A β law was used to describe the velocity law in the stellar winds, and a super-level approach was adopted for the resolution of the equations of statistical equilibrium. The following chemical elements and their ions were included in the calculations: H, He, C, N, O, Ne, Mg, Al, Si, S, Ca, Fe, and Ni. A new photospheric structure was computed from the solution of the equations of statistical equilibrium, and was then connected to the same β wind velocity law. We assumed a microturbulent velocity in the atmosphere varying linearly with wind velocity from 10 $\mathrm{km\,s^{-1}}$ in the photosphere to $0.1 \times \mathrm{v}_\infty$ at the outer boundary. The generated synthetic spectra were then recombined and compared to the spectra of the triple system to constrain iteratively the fundamental properties of the three stars, with the following method.

As a starting point, we assumed that these fundamental properties were close to typical values of stars of the same spectral type. We thus took the surface gravities, stellar masses, radii, luminosities and effective temperatures from Martins et al. (2005), the mass-loss rates and β of the velocity law from Muijres et al. (2012) and the terminal velocities from Prinja et al. (1990).

In order to have a first approximation of the rotational velocities, we used a multi-Gaussian fitting technique within MIDAS on the lines He I $\lambda\lambda$ 4471 and 4922, O III λ 5592 and C III λ 5812 for the most deblended observed spectra, and we applied a Fourier transform method (Simón-Díaz & Herrero 2007, Gray 2008) to the best fitting Gaussians. We estimated the macroturbulence velocities with the auxiliary program MACTURB of the stellar spectral synthesis program SPECTRUM v2.76 developed by Gray (2010), applying this technique to the wings of He I λ 4026, 4471, 4713 and 5016, and He II λ 4542 for several phases.

We estimated the respective contribution of the three components to the spectra of the triple system through the following formula on selected lines:

$$\frac{l_i}{l_i+l_j+l_k} = \frac{l_i}{l_j\left(\frac{l_i}{l_j}+1+\frac{l_k}{l_j}\right)}$$

with

$$\frac{l_i}{l_j} = \left(\frac{EW_i}{EW_j}\right)_{\text{obs}} \left(\frac{EW_{STj}}{EW_{STi}}\right)_{\text{mean}}$$

where i, j and k are representing either the primary, secondary or tertiary stars, depending on the contribution we were calculating. The EW_i represent the equivalent widths of the studied lines of star i referring to the combined continuum of the three stars and EW_{STi} the same measurement in the synthetic spectrum of a typical star of the same spectral type as star i, computed with CMFGEN. We considered the spectral types previously determined by Hillwig et al. (2006; O7.5V((f)) + O7.5V((f)) + O6.5III((f))). This way, we obtained that the primary, secondary and tertiary contributions to the total flux are 29%, 34% and 37%, respectively, which is close to what Hillwig et al. (2006) found in their study of HD 17505 (30%, 30% and 40%, respectively).

We then constrained the physical properties of each star by an iterative process, because each adjustment of a given parameter leads to some modifications in the value of others, and each modification in the spectrum of one of the three stars may require some modifications in the spectrum of one of the other two. For each star, the following process is used to adjust the fit of the spectra.

The first step is to adjust the effective temperature in the models. This parameter is mainly determined through the relative strengths of He I λ 4471 and He II λ 4542 lines (Martins 2011).

Then comes a first approximation of the surface gravities through the width of the Balmer lines, which were approximatively reconstructed with a multi-Gaussian fit on a number of observations at different phases.

Subsequently, the multiplicity of the object may cause some problems. Indeed, the next step is to adjust the wind parameters, but the He II λ 4686 and the Balmer lines may be polluted by some emission from a wind-wind interaction zone within the inner binary of HD 17505. Therefore, considering the possible existence of such additional emission polluting the diagnostic lines, the adjustment of the models onto the observed spectra may lead to an underestimate of the terminal velocities, and an overestimate of the β of the velocity law, the clumping factors, the clumping velocity factors, and the mass-loss rates of the primary and secondary stars. The values obtained with such a fit should thus only be considered as lower and upper limits of the real properties of the corresponding stellar winds. However, we nevertheless adjusted them as well as possible. The spectrum of the third component, however, should not be affected by such pollution, since it is too distant from the inner binary to induce such wind-wind interactions. The diagnostic lines of the terminal velocities, β and the mass-loss rates are the strength of Hα, the width of He II λ4686 and Hα, and the strengths of Hγ and Hδ, respectively, while the clumping filling factors and the clumping velocity factors are based on the shape of the Hα and Hβ lines.

Once the fundamental stellar parameters were established, we investigated the CNO abundances through the strengths of associated lines. We performed a normalized χ^2 analysis to determine the best fit to selected lines, as done by Martins et al. (2015; see also Raucq et al. 2016; 2017) and explained in Sect. 2.2.2. We used the C III $\lambda\lambda$ 4068-70, 4156, 4163, and 4187; N II λ 4379, and N III $\lambda\lambda$ 4511, 4515, and 4525; and O III $\lambda\lambda$ 5508 and 5592 lines to adjust the C, N and O abundances, respectively, for both stars.

In Fig. 3.8 we show parts of the observed spectra at different phases with the corresponding recombined synthetic spectra of the triple system.

Once we obtained a good fit of the triple system for all the observations, we substracted the synthetic tertiary spectrum from each observation, to recover the spectra of the inner binary. After removal of the third object, we then treated the spectra with the disentangling code, in the same way as for the other binary systems, HD 149404 (see Sect. 3.1 of Raucq et al. 2016) and LSS 3074 (see Sect. 6.1 of Raucq et al. 2017).

3.4.4.2 Spectral types

Once we obtained the individual reconstructed spectra of the primary and secondary components of HD 17505, we determined their respective spectral types. To do so, we applied Conti's quantitative classification criterion for O-type stars (Conti & Alschuler 1971, Conti & Frost 1977, see also van der Hucht 1996) for the spectral types, based on the equivalent width ratio of the spectral lines He I λ4471 and He II λ4542. This way, we obtained that both primary and secondary stars are O7 stars. However, it was not possible to use Conti's criterion for the luminosity classes, based on the equivalent width ratio of the spectral lines Si IV λ4088 and He I λ4143, since the latter line is very weak or even non existent in the reconstructed spectra. We thus used the Walborn criterion (Walborn & Fitzpatrick 1990 and references therein) to determine that both stars are V stars, since they display a strong He II λ4686 absorption. In addition to the strong absorption of He II λ4686, the spectra of both stars also display

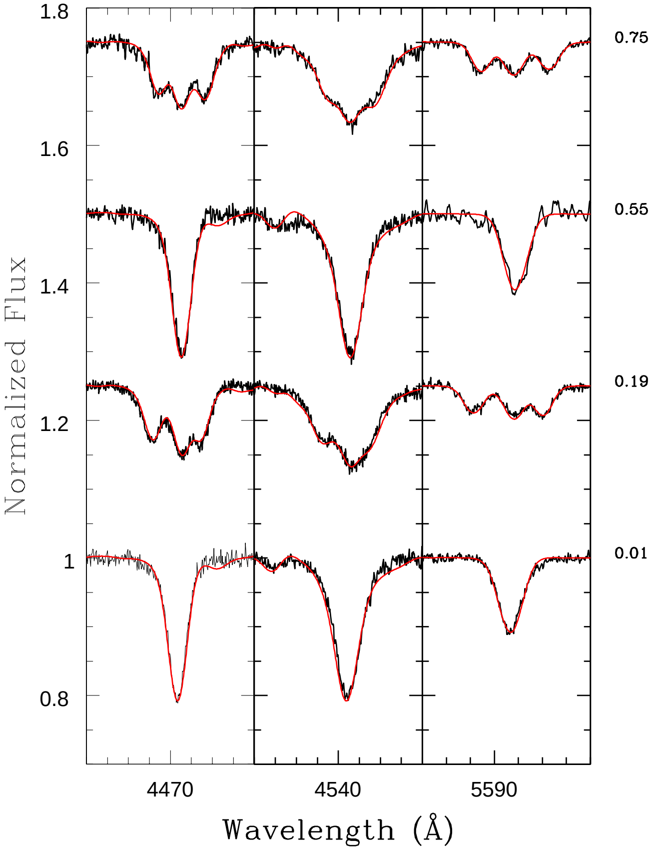

Figure 3.8: He I λ 4471 (left panel), He II λ 4542 (middle panel) and O III λ 5592 lines (right panel) of the recombined synthetic spectrum (red) of the triple system HD 17505 for different observations (black). The phases of the different observations, according to the ephemerides of Table 3.4, are presented at the left side of the figure.

N III $\lambda\lambda$ 4634-40-42 emission, leading to the addition of a ((f)) qualifier to their spectral types. We thus found that both primary and secondary stars are O7V((f)) stars. Our classification being based on the separated spectra, it is less sensitive to a possible phase-dependence of some specific spectral features, and should thus be more robust than a classification based only on spectra taken near quadrature phases. But we can note than we find an excellent agreement with the spectral types proposed by

Hillwig et al. (2006, O7.5V((f)) + O7.5V((f))), which they determined via tomographic reconstruction of the individual spectra.

3.4.4.3 Brightness ratio

Whilst the spectral disentangling yields the strength of the lines in both primary and secondary spectra compared to the combined continuum, it does not permit to establish the relative strengths of the individual continua. To further analyse the reconstructed spectra, we therefore need to establish the brightness ratio of the stars in an independant way.

To determine the brightness ratio of the primary and secondary components of HD 17505, we used a similar technique as done in Sect. 3.4.4.1 to estimate the contribution of the three components of the triple system to the observations. Here, instead of measuring the equivalent widths on a multi-Gaussian fit, we measured the equivalent widths of a number of selected spectral lines on the separated spectra of the primary and secondary stars, but referring to the combined continuum of the two stars.

The results are listed in Table 3.5. From these equivalent widths, the brightness ratio of two stars can be calculated from

$$\frac{l_1}{l_2} = \left(\frac{EW_1}{EW_2}\right)_{\mathrm{obs}} \left(\frac{EW_{ST2}}{EW_{ST1}}\right)_{\mathrm{mean}}$$

with the same conventions as in the previous section. In the particular case of HD 17505, since the spectral types of the primary and secondary stars are identical, the second term of the equation is equal to 1, and the brightness ratio of the two stars can be simply evaluated as the ratio of their respective equivalent widths, averaged over the selected lines.

This way, we derived a primary over secondary brightness ratio of 0.88 ± 0.09. This value is very close to what we inferred from our preliminary study of the contributions of the different components to the observed spectra of the triple system, based on the multi-Gaussian fit, i.e. $l_1/l_2 = 29/34 = 0.85$, and is slightly lower than the brightness ratio of 1.00 proposed by Hillwig et al. (2006).

Høg et al. (2000) give a mean V magnitude of 7.356 ± 0.010 and $B-V$ color of 0.308 ± 0.019 for the inner triple system, HD 17505A. The intrinsic $(B-V)_0$ of O7 stars being -0.27 (Martins & Plez 2006), we determined an extinction A_V of 1.792 ± 0.059, assuming $R_V = 3.1$. Assuming the ~ 1.9 kpc distance (Hillwig et al. 2006), we inferred an absolute magnitude $M_V = -5.830 \pm 0.059$ for the system. With the previously determined brightness ratio, we then calculated individual absolute magnitudes of $M_V^P = -5.005 \pm 0.079$ and $M_V^S = -5.145 \pm 0.079$.

The reconstructed normalized primary and secondary optical spectra are shown and discussed in Sect. 3.4.5.2.

Table 3.5: Determination of the brightness ratio of the inner binary system of HD 17505 from the dilution of prominent lines.

Line	Equivalent width (Å)		l_1/l_2
	Primary	Secondary	
He I λ 4026	0.11	0.15	0.73
He II λ 4200	0.09	0.10	0.94
Hγ	0.51	0.52	0.98
He I λ 4471	0.12	0.14	0.88
He II λ 4542	0.14	0.17	0.87

Table 3.6: Projected rotational velocities ($v \sin i$ in km s^{-1}) of the primary and secondary components of HD 17505.

Line	Primary	Secondary
He I λ 4026	77	87
He II λ 4200	72	88
He II λ 4471	53	59
He II λ 4542	66	71
He I λ 4922	49	55
He I λ 5016	53	57
O III λ 5592	62	62
Mean value	61.6 ± 9.6	68.4 ± 13.1

3.4.5 Spectral analysis

3.4.5.1 Rotational velocities and macroturbulence

The reconstructed individual spectra also allowed us to confirm the values of the projected rotational velocities and macroturbulence of the primary and secondary stars. We used the same Fourier transform analysis (Simón-Díaz & Herrero 2007) as in Sect. 3.4.4.1, applied on the profiles of isolated lines in the disentangled spectra. The elimination of the third component and the reconstruction of the individual spectra permitted us to use more lines at this stage than what was possible with the multi-Gaussian fit. This way, we determined the projected rotational velocities $v \sin i$ of the primary and secondary stars based on the He I $\lambda\lambda$ 4026, 4471, 4922 and 5016, He II $\lambda\lambda$ 4200 and 4542, and O III λ 5592 lines.

The results are presented in Table 3.6. The mean $v \sin i$ of the primary star is (61.6 ± 9.6) km s^{-1}, and that of the secondary star is (68.4 ± 13.1) km s^{-1}.

After determining the projected rotational velocities, we adjusted our determination of the macroturbulence velocities for the primary and secondary stars. To do so, we used the auxiliary program MACTURB developed by Gray (2010), based on the radial-tangential anisotropic macroturbulent broadening formulation of Gray (2008), on the lines He I $\lambda\lambda$ 4026, 4471, 4713 and 5016, and He II λ 4542 in the individual spectra, after including the rotational velocity broadening. This way, we obtained macroturbulence velocities of 60 and 65 km s^{-1} for the primary and secondary stars respectively.

Both rotational and macroturbulence broadening effects were applied on the synthetic spectra before comparing the latter with the individual reconstructed spectra of the primary and secondary stars of HD 17505.

3.4.5.2 Fit of the separated spectra with the CMFGEN code

Once we obtained the separated spectra of the primary and secondary stars of HD 17505, their brightness ratio, rotational velocities and macroturbulence velocities, we then improved our determination of the fundamental properties of both stars with the CMFGEN code. We followed the same procedure as exposed in Sect. 3.4.4.1 to constrain the different stellar parameters.

However, as explained in Sect. 2.1.2, the Balmer lines are too broad to be well recovered by the disentangling process, and their wings are thus not perfectly reliable to adjust the surface gravities. We thus used an iterative process to contrain the luminosities together with these gravities. From the first estimate of $\log g$ given by the fit of the triple system, performed in Sect. 3.4.4.1, and our determination of the effective temperatures, we inferred the bolometric corrections (Lanz & Hubeny 2003), then the individual bolometric luminosities, using the absolute V magnitudes of the components derived in Sect. 3.4.4.3. These bolometric luminosities and the effective temperatures then permitted us to compute the ratio of the stellar radii $\frac{R_P}{R_S}$. Together with the assumed surface gravities, this ratio yielded the spectroscopic mass ratio $\frac{M_P}{M_S}$, which we compared to the dynamical mass ratio inferred from the orbital solution (Sect. 3.4.3). The difference between these mass ratios then permitted us to produce a new estimate of the surface gravities. This iterative process was repeated until the spectroscopic and dynamical mass ratios agreed with each other, and the CMFGEN synthetic spectra produced for the new surface gravities matched the observations as well as possible.

Figure 3.9 shows the best fit of the optical spectra of the primary and secondary stars of HD 17505 obtained with CMFGEN, and Table 3.7 lists the corresponding stellar parameters. Table 3.8 compares the chemical abundances of these best-fit models with the solar abundances taken from

Asplund et al. (2009).

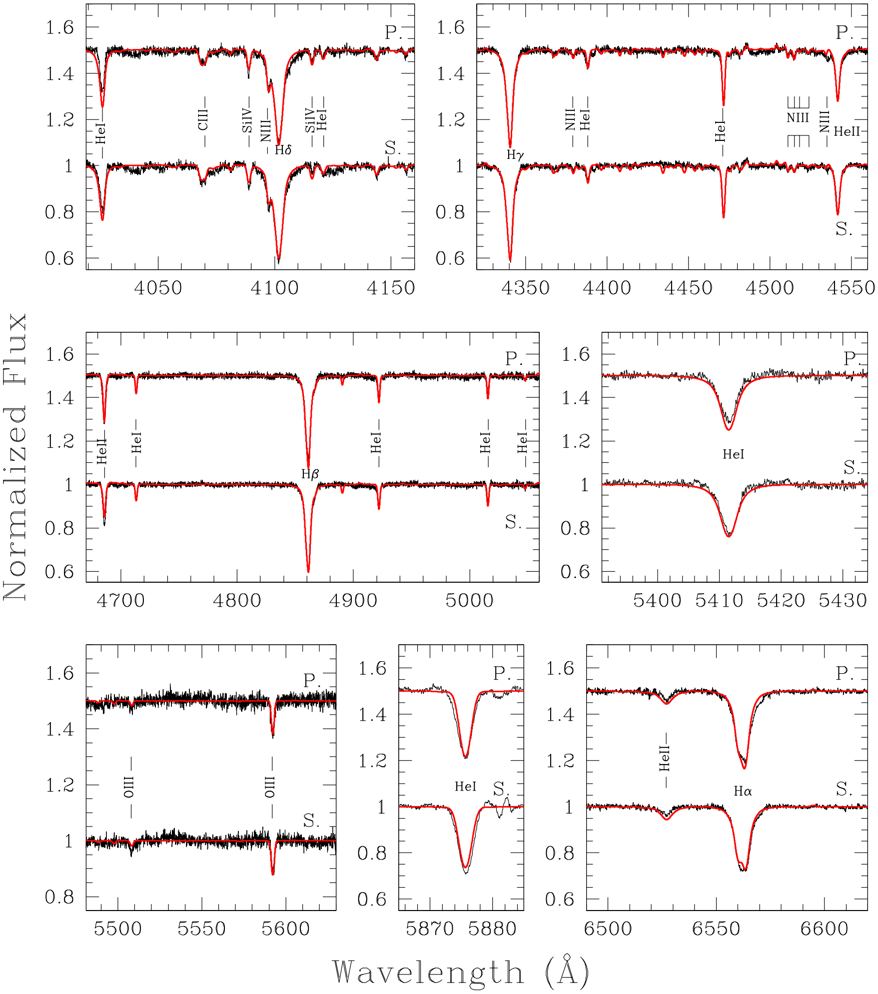

Figure 3.9: Part of the normalized disentangled spectra of the primary (top, shifted by 0.5 continuum units) and secondary (bottom) stars of HD 17505, along with the best-fit CMFGEN model spectra (red).

Figure 3.9 shows that the Balmer, He, C and N lines are very well reproduced by the models for both stars. The case of oxygen raises more questions. Indeed, while the O III $\lambda\lambda$ 5508 and 5592 lines are well adjusted, several other O III lines (e.g. OIII $\lambda\lambda$ 4448, 4454, and 4458 lines) are present

Table 3.7: Best-fit CMFGEN model parameters of the primary and secondary stars of HD 17505.

	Prim.	Sec.
R (R$_\odot$)	13.4 ± 1.0	13.6 ± 1.0
M (M$_\odot$)	22.7 ± 8.6	24.2 ± 9.0
$T_{\rm eff}$ (10^4 K)	3.70 ± 0.15	3.67 ± 0.15
$\log\,(\frac{L}{L_\odot})$	5.26 ± 0.03	5.31 ± 0.03
$\log g$ (cgs)	3.80 ± 0.15	3.73 ± 0.15
β	≤ 1.07	≤ 1.07
v_∞ (km s^{-1})	≥ 2200	≥ 2200
$\dot{M}/\sqrt{f_1}$ (M$_\odot$ yr^{-1})	$\leq 2.30 \times 10^{-7}$	$\leq 3.70 \times 10^{-7}$
f_1	≤ 0.1	≤ 0.2
f_2 (km s^{-1})	≤ 250	≤ 180
BC	-3.40	-3.38

f_1 and f_2 represent the clumping filling factor and the clumping velocity factor, presented in Sect. 2.2.2. The quoted errors correspond to 1σ uncertainties. The bolometric corrections are taken from Lanz & Hubeny (2003), based on our best-fit $T_{\rm eff}$ and $\log g$.

Table 3.8: Chemical surface abundances of the primary and secondary stars of HD 17505.

	Primary	Secondary	Sun
He/H	0.1	0.1	0.089
C/H	$1.91^{+0.37}_{-0.40} \times 10^{-4}$	$1.97^{+0.39}_{-0.42} \times 10^{-4}$	2.69×10^{-4}
N/H	$1.37^{+0.25}_{-0.21} \times 10^{-4}$	$9.70^{+1.1}_{-0.84} \times 10^{-5}$	6.76×10^{-5}
O/H	$3.87^{+1.2}_{-0.92} \times 10^{-4}$	$4.73^{+2.2}_{-1.5} \times 10^{-4}$	4.90×10^{-4}

Abundances are given by number as obtained with CMFGEN. The solar abundances (Asplund et al. 2009) are quoted in the last column. The 1σ uncertainty on the abundances was set to abundances corresponding to a normalized χ^2 of 2.0 (see Sect. 2.2.2 of this work, Sect. 4.3 of Raucq et al. 2016 and Sect. 8.3 of Raucq et al. 2017; see also Martins et al. 2015). The values of the He abundances have been fixed in the models.

in the synthetic CMFGEN spectra of both stars, but are not visible in the separated spectra, nor in the observed spectra of the system before the disentangling procedure. We encountered similar problems with the same lines in the case of HD 149404 (see Raucq et al. 2016).

We can stress here three important results. First of all, by coupling the stellar masses obtained with CMFGEN (Table 3.7) with the minimum masses obtained with the orbital solution (Table 3.4), we obtain an inclination of the system $i \sim 53.3°$. With this inclination, we can see from our determination of the stellar radii with CMFGEN compared to the radii of the Roche lobes obtained in the orbital solution (Table 3.4) that both stars are well into their Roche lobes: they display a Roche lobe filling factor of 0.57 ± 0.08 and 0.56 ± 0.08, respectively. Second, we note that there is a slight enhancement of the N abundance, coupled with an even slighter C and O depletion at the surface of both stars. However, these modifications of the surface abundances are low enough to be explained by rotational mixing in the star (see Sect. 3.4.6.1), with no need to include mass-exchange episode in the history of the system. The third result is also pointing in the same direction. Indeed, from the inclination determined earlier, we can derive the absolute rotational velocities and we obtain 76.8 and 85.3 $\mathrm{km\,s^{-1}}$ for the primary and secondary stars respectively. Finally, by combining these rotational velocities with the stellar radii determined with CMFGEN (Table 3.7), we find that the primary and secondary stars of HD 17505 are in perfectly synchronous rotation: $P_P = 8.83$, $P_S = 8.07$ and $P_{\rm orb} = 8.569$ days. Moreover, if we calculate the critical velocities of the stars, $v_{\rm crit} = \left(\frac{2GM}{3R_P}\right)^{1/2}$, based on our results from the CMFGEN fit, we find that the current rotational velocities of the primary and secondary stars correspond to $0.16 \times v_{\rm crit}$ and $0.18 \times v_{\rm crit}$ respectively, which correspond to the median value of birth rotational velocities for stars of similar masses, according to the study of Wolff et al. (2006). This suggests that there has not been any kinetic momentum exchange between the two components in the past history of the inner binary system. These three results suggest that this system has not yet experienced a RLOF episode during its evolution. We will come back to these results in Sect. 3.4.6.1.

3.4.6 Discussion and conclusion

3.4.6.1 Evolutionary status

As we have shown in the previous section, the spectra of the primary and secondary components of HD 17505 display the signatures of a slight modification of the CNO surface abundances. Figure 3.10 compares our inferred N/C and N/O ratios with the predictions for the evolution of single massive stars (Ekström et al. 2012). The left panel shows the case of non-rotating stars, whilst the right panel shows the case of stars rotating at $0.4 \times v_{crit}$. This figure shows that the current surface abundances of both stars are difficult to explain in the non-rotating case: the only possibility for the secondary would be an initial mass of $60\,M_\odot$, while its spectroscopic mass is a factor 2.4 lower, and none of the theoretical predictions can explain the surface abundances of the primary star. However,

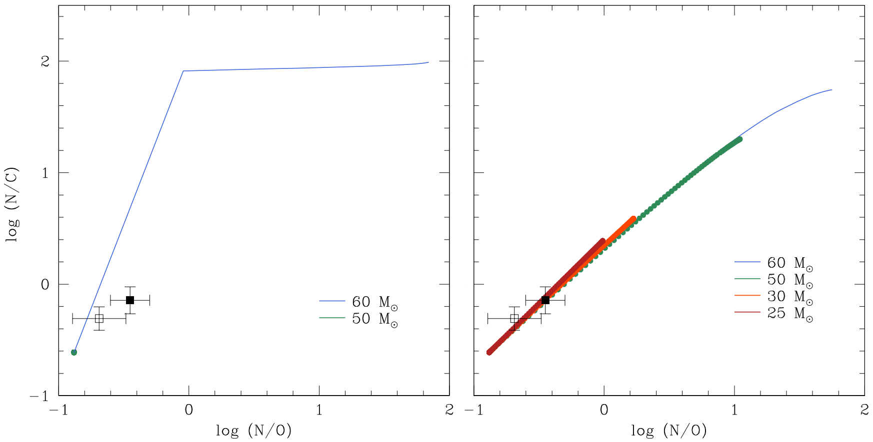

Figure 3.10: Comparison of the N/C and N/O ratios obtained from our spectral analysis with predictions from single star evolutionary models of different masses (Ekström et al. 2012). The filled (resp. empty) squares display the characteristics of the primary (resp. secondary) star. The left panel illustrates the results for core hydrogen burning phase tracks without stellar rotation, and the right panel corresponds to the same tracks for stars with a rotation of $0.4 \times v_{crit}$.

both primary and secondary abundances can be explained by the rotating models, with single stars of initial masses close to 25-30 $M_{\odot}$, which is close to the masses we inferred from our spectroscopic analysis for both stars (Table 3.7).

In Figure 3.11 we present the positions of the primary and secondary stars in the Hertzsprung-Russell diagram (HRD; upper panels) and in the $\log g$-$\log T_{\rm eff}$ diagram (lower panels), with the evolutionary tracks from Ekström et al. (2012) for the core-hydrogen burning phase of single stars at solar metallicity. Once again, the left panels display the non-rotating stars case and the right panels show the tracks for stars rotating at $0.4 \times v_{crit}$.

If we consider the case without any rotational mixing, we can see that the positions of the primary and secondary stars in the HRD are relatively close to the tracks corresponding to stars with an initial mass of 30 $M_{\odot}$, which is close to their current spectroscopic masses of 24-25 $M_{\odot}$, and may be located on a common isochrone between 3.2 and 4.0 million years. In the $\log g$-$\log T_{\rm eff}$ diagram, however, while they are located again on the same isochrone at 3.2 million years, they are closer to the 40 $M_{\odot}$ evolutionary track, which is significantly higher than their observed masses.

Considering now the case of stars rotating at 40% of their critical velocity, we see that both stars would have initial masses of 30-32 $M_\odot$, which is again close to their spectroscopic masses, and they would both be $\sim$4.0 million years old.

Both our results in Sect. 3.4.5.2 and the Figures 3.10 and 3.11 show that both primary and secondary stars current properties can be explained by single star evolutionary models with a rotational velocity of $0.4 \times v_{crit}$, which suggests that the inner binary system of HD 17505 did not experience strong binary interactions at this stage of its life.

3.4.6.2 Summary and conclusion

We have studied the fundamental properties of the inner binary system of HD 17505 by means of several techniques. To do so, our first step was to fit the inner triple system with a combination of synthetic CMFGEN spectra of the three components shifted by their associated RVs for each observation, in order to substract the third component from the observed spectra and recover the spectra of the inner binary. We then used our disentangling code to recover the individual spectra of the primary and secondary stars. From these reconstructed spectra, we determined accurately a number of stellar parameters, partly with the CMFGEN model atmosphere code, and used them to constrain the evolutionary status of the system.

We established the existence of a slight overabundance in N and slight C and O depletions in both primary and secondary spectra and we found no evidence of asynchronous rotation between the primary and secondary stars. We showed that these properties can be explained by single star evolutionary models of initial mass of 30-32 $M_\odot$, with a rotational velocity of 40% of their critical velocity. We thus concluded that this system has not experienced binary interactions at this stage of its evolution.

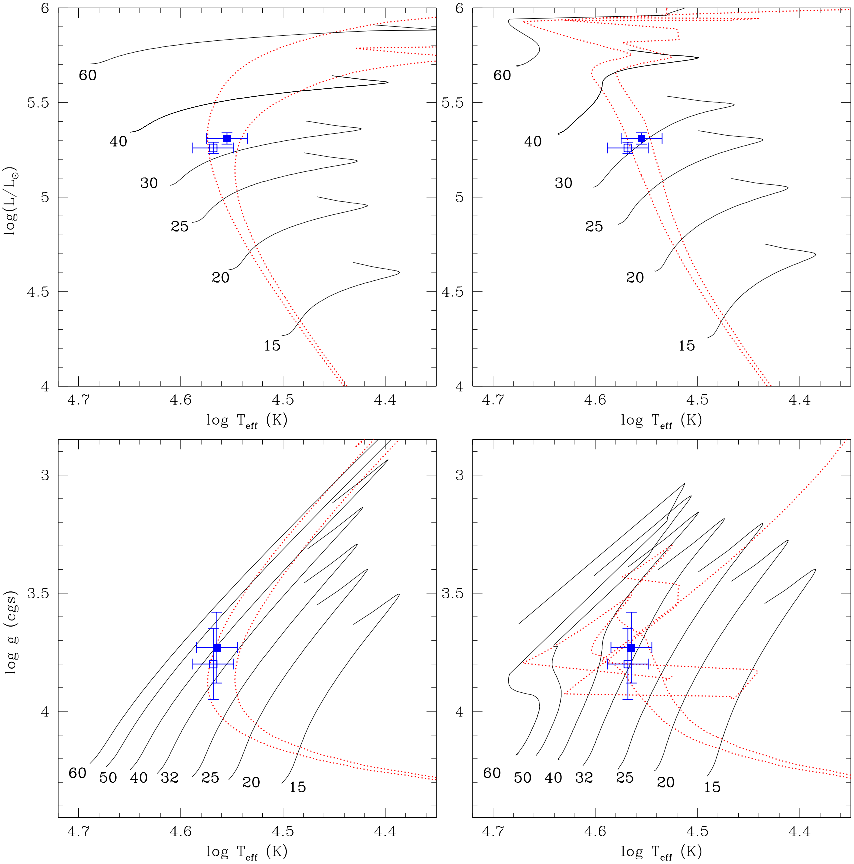

Figure 3.11: The upper panels show the positions of the primary (empty square) and secondary (filled square) stars of HD 17505 in the Hertzsprung-Russell diagram, while the lower panels show their positions in the log g-log $T_{\rm eff}$ diagram, along with evolutionary tracks for single massive stars at solar metallicity during the core-hydrogen burning phase (Ekström et al. 2012). In the left panels, the evolutionary tracks correspond to non-rotating stars, whilst the right panels yield the results for stars rotating at $0.4 \times v_{crit}$. The dotted red lines correspond to isochrones of 3.2 and 4.0 million years for the left panels and of 4.0 and 5.0 million years for the right panels.

3.5 HD 206267

3.5.1 Introduction

HD 206267 is a multiple system dominating the young open cluster Trumpler 37 and the H II region IC 1396, embeded in the Cep OB2 association. This system was first studied by Plaskett in 1923, and directly presented problems for the observers, since its spectrum displays rather diffuse lines, some of them being double and showing variable strength and profile. Stickland (1995) suspected the system to be triple, with a third constant-velocity component, and presented a new orbital solution of the inner binary based on high-resolution, short-wavelength (SWP) *IUE* spectra. He found a short orbital period of 3.71 days for the inner binary system. In addition to the short period, the massive character of both primary and secondary stars (O6.5 V + O9.5 V) determined by Burkholder et al. in 1997 makes this system a good candidate for our search of past mass-exchange episodes in massive binaries.

In this study, we constrained the fundamental parameters of the stars of the inner binary of HD 206267 with a set of several techniques of analysis. We present the data used in our study in Sect. 3.5.2 and our revised orbital solution of the inner system in Sect. 3.5.3. The preparatory analysis of our data, including the reconstruction of the individual spectra of the primary and secondary components with our spectral disentangling code, are presented in Sect. 3.5.4 and the spectral analysis performed with the non-LTE atmosphere code CMFGEN in Sect. 3.5.5. Finally, we discuss the results of our study of HD 206267 in Sect. 3.5.6.

3.5.2 Observations and data reduction

For our study of HD 206267, we collected twenty-two high-resolution optical spectra with the HEROS spectrograph, mounted on the 1.2 m TIGRE telescope at La Luz Observatory (Mexico; Schmitt et al. 2014). The spectra were collected during two observing runs: the first half between the 26th of August 2014 and 27th of October 2014, and the second half between the 2nd of August 2015 and the 28th of October 2015. The HEROS spectrograph covers two spectral domains: from 3500 to 5600 Å (the blue chanel) and from 5800 to 8800 Å (red channel), with a resolution of $\sim$ 20 000. The spectra were automatically reduced with an Interactive Data Language (IDL) pipeline based on the reduction package REDUCE written by Piskunov & Valenti (2002).

We also retrieved a series of reduced spectra from different archives. One spectrum from the ELODIE archives, taken in September 1997, one spectrum from the ESPaDOnS archives, taken in August 2011, and nine spectra from the Sophie archives, taken in August 2013. The ELODIE échelle spectrograph was mounted on the 1.93 m telescope at the Observatoire de Haute Provence (OHP, France) from 1993 to 2006, and covered the spectral range from 3850 to 6800 Å with a resolution of ~42 000. The ESPaDOnS échelle spectrograph is mounted on the Canada-France-Hawaii Telescope (CFHT) on Mauna Kea. The SOPHIE spectrograph is mounted on the 1.93 m telescope at the Observatoire de Haute Provence (OHP, France), and covers the wavelength range from 3872 to 6943 Å with a resolution of ~40 000 (high-efficiency mode).

We are also grateful to Sergio Simón-Díaz for giving us access to a series of five reduced spectra of HD 206267 taken in October 2010, Septembre 2011 and December 2012 with the FIES échelle spectrograph (Simón-Díaz et al. 2011a; 2011b; 2015). The FIES échelle spectrograph is mounted on the 2.5 m Nordic Optical Telescope (NOT) located at the Observatorio del Roque de los Muchachos (La Palma, Spain). It covers the spectral range from 3700 to 7300 Å with a resolution of ~46 000 in medium-resolution mode.

The journal of the observations is presented in Table 3.9.

3.5.3 New orbital solution

From our set of observations, we calculated a new orbital solution of the inner binary system of HD 206267, based on the strongest absorption lines that are essentially free from blends with other features. We thus measured the RVs of He I $\lambda\lambda$4026, 4471, 5876, and 7065 lines by a multi-Gaussian fit on the observed spectra. We adopted the effective wavelengths of Underhill (1995). For each observation, the RVs of the primary and secondary stars were determined as the mean of the corresponding RVs measured for each of the above-listed lines in that given observation. Given the strong broadening effect of the large rotational velocities and macroturbulence velocities on the spectra, broader features such as He II and Hγ lines of the primary, secondary and tertiary stars were too heavily blended with each others to allow us to determine the individual RVs of each component.

The resulting RVs are listed in Table 3.9. The uncertainties on these RVs are about $10 - 20$ km s^{-1} for most observations, but can however reach values larger than 30 km s^{-1} for some observations, indicated by the colons in Table 3.9. We obtain a mean RV of -7.03 km s^{-1} for the third component of the system.

Based on these measurements, we performed a Fourier analysis of the RV$_1$ and RV$_2$ data, that yielded a highest peak around $\nu = 0.269502$ d^{-1}, i.e. $P_{\rm orb} = 3.710534$ days, which is very close to the orbital period of

Table 3.9: Journal of the spectra of HD 206267.

HJD-2 450 000	Instrument	Exp. time (min)	ϕ	RV$_1$ (km s^{-1})	RV$_2$ (km s^{-1})
0710.4441	ELODIE	22.3	0.42	-166.64:	279.78
5494.3031	FIES	3.3	0.95	163.71	-298.86
5729.1077	ESPaDOnS	7.5	0.24	-144.38	95.92
5812.5828	FIES	2.1	0.74	107.95	-113.76:
5816.4969	FIES	2.1	0.80	116.34:	-141.13:
5817.5170	FIES	2.6	0.07	70.20:	-233.19
6285.3231	FIES	3.4	0.17	-7.10	-7.10
6527.4539	SOPHIE	5	0.44	-160.71	294.96
6527.5577	SOPHIE	5	0.47	-160.47	291.80
6528.4396	SOPHIE	5	0.71	-13.17	-13.17
6528.5550	SOPHIE	5	0.74	-13.17	-13.17
6529.4943	SOPHIE	5	0.99	180.19	-301.36
6530.3561	SOPHIE	5	0.22	-137.16	80.18
6530.5523	SOPHIE	5	0.28	-149.83	164.45
6531.4081	SOPHIE	5	0.51	-170.80	251.79
6531.5479	SOPHIE	5	0.54	-140.55	221.30
6895.7500	HEROS	30	0.72	-4.52	-4.52
6897.7738	HEROS	30	0.26	-133.61	128.00
6907.7219	HEROS	30	0.95	123.25:	-312.95:
6909.7156	HEROS	30	0.48	-147.36	291.91
6911.7011	HEROS	30	0.02	149.51	-279.74
6920.6768	HEROS	30	0.44	-162.35	276.12:
6926.6468	HEROS	30	0.05	159.82	-252.97
6939.6036	HEROS	30	0.54	-145.36	223.14
6941.6020	HEROS	30	0.08	167.72	-227.50
6944.6560	HEROS	30	0.90	160.05	-278.83
6957.5806	HEROS	30	0.38	-146.99	273.99:
7236.7624	HEROS	15	0.64	-142.53	164.15
7236.7729	HEROS	15	0.64	-117.50	165.15
7238.7444	HEROS	30	0.17	-3.96	-3.96
7264.8159	HEROS	30	0.20	-3.96	-3.96
7271.7659	HEROS	30	0.08	161.57	-229.72
7286.6714	HEROS	30	0.09	162.89	-180.75
7288.6617	HEROS	30	0.63	-145.56	131.03:
7290.7237	HEROS	30	0.19	-3.96	-3.96
7292.6865	HEROS	30	0.72	-92.04:	158.66
7308.6686	HEROS	30	0.02	170.45	-278.45
7323.5769	HEROS	30	0.04	178.21	-257.39

The phases (ϕ) are computed according to the ephemerides of the combined orbital solution listed in Table 3.10. The radial velocities are presented in Sect. 3.5.3. The typical uncertainties on the RVs are $10 - 20$ km s^{-1}. The colons indicate uncertainties larger than 30 km s^{-1}. The mean value of the RVs of the third component is -7.03 km s^{-1}.

$P_{\rm orb} = 3.709838$ days proposed by Stickland (1995). We also performed the same Fourier analysis with our RVs combined to those measured by Stickland (1995) and Burkholder et al. (1997) and obtained a highest peak around $\nu = 0.269558$ d^{-1}, which corresponds to $P_{\rm orb} = 3.709777$ days, which is consistent with the determinations based on our data and those of Stickland (1995) separately.

Adopting orbital periods of 3.710534 and 3.709777 days, we then computed two orbital solutions with the LOSP code (Sana et al. 2009, and references therein) assuming an eccentric orbit, since the previous orbital solution of Stickland (1995) predicted an eccentricity of 0.119 ± 0.012. The RVs were weighted according to their estimated uncertainties. The results of our determination of a new orbital solution based on our sole measurements and on our RVs combined with those of Stickland (1995) and Burkholder et al. (1997) are shown in Fig. 3.12 in the upper and lower panels respectively. The corresponding orbital elements are provided in Table 3.10, together with those found in the previous studies of Stickland (1995) and Burkholder et al. (1997).

We can highlight that the RV amplitudes, minimum masses, mass ratios and eccentricities of both our single and combined solutions are in good agreement with those of previous works. However, we can note that in our orbital solution based only on our dataset, there is one observation (taken with the ELODIE instrument on the HJD 2 450 710.4441) that seems to be at odds with the computed RVs curves, while it is well integrated in the curves for our combined orbital solution. Moreover, the sigma of the fit of the combined orbital solution is significantly better than the one of our orbital solution based on our RVs only. We thus chose to base our subsequent analysis of the inner binary system of HD 206267 on the orbital solution based on our RVs combined to those measured by Stickland (1995) and Burkholder et al. (1997).

Table 3.10: Orbital solution of the inner binary computed from our RV data of HD 206267, assuming an eccentric orbit and a period of 3.710534 days, compared to the orbital solutions proposed by Stickland (1995) and Burkholder et al. (1997), and a solution obtained by combining our RVs with those measured by these authors.

	This study		Combined solution	
	Primary	Secondary	Primary	Secondary
P_{orb} (days)	3.710534		3.709777	
T_0 (HJD - 2 450 000)	5494.385 ± 0.128		5494.503 ± 0.069	
e	0.1303 ± 0.0231		0.1306 ± 0.0149	
γ ($\mathrm{km\,s^{-1}}$)	-19.4 ± 5.0	9.9 ± 6.3	-14.9 ± 3.1	0.1 ± 4.0
K ($\mathrm{km\,s^{-1}}$)	184.0 ± 6.2	275.4 ± 9.2	186.1 ± 3.6	295.5 ± 5.7
$a \sin i$ ($\mathrm{R_\odot}$)	13.4 ± 0.4	20.0 ± 0.7	13.5 ± 0.3	21.5 ± 0.4
$q = m_1/m_2$	1.50 ± 0.07		1.59 ± 0.04	
ω (°)	31.2 ± 12.7		21.3 ± 6.9	
$m \sin^3 i$ ($\mathrm{M_\odot}$)	21.8 ± 1.8	14.5 ± 1.1	25.7 ± 1.2	16.2 ± 0.7
$R_{\mathrm{RL}}/(a_1 + a_2)$	0.41 ± 0.01	0.34 ± 0.01	0.42 ± 0.01	0.34 ± 0.01
$R_{\mathrm{RL}} \sin i$	13.8 ± 0.4	11.6 ± 0.3	14.7 ± 0.2	11.9 ± 0.2
σ_{fit}	6.08		2.28	

	Stickland (1995)		Burkholder et al. (1997)	
	Primary	Secondary	Primary	Secondary
P_{orb} (days)	3.709838 ± 0.000010		3.709838 ± 0.000010 (f)	
T_0 (HJD - 2 440 000)	9239.720 ± 0.067		9239.720 ± 0.067 (f)	
e	0.119 ± 0.012		0.119 ± 0.012 (f)	
γ ($\mathrm{km\,s^{-1}}$)	-24.8 ± 1.4		-10.7 ± 9.4	-6.8 ± 8.3
K ($\mathrm{km\,s^{-1}}$)	161.1 ± 2.5	288.0 ± 11.5	187.5 ± 5.7	307.6 ± 3.8
$a \sin i$ ($\mathrm{R_\odot}$)	11.7 ± 0.18		13.6 ± 0.4	22.4 ± 0.3
$q = m_1/m_2$	1.79		1.64	
ω (°)	13.1 ± 6.7		13.1 ± 6.7 (f)	
$m \sin^3 i$ ($\mathrm{M_\odot}$)	22.1 ± 2.5	12.3 ± 0.8	28.4 ± 1.5	17.3 ± 1.5

γ, K and a sin$i$ denote respectively the apparent systemic velocity, the semi-amplitude of the radial velocity curve and the projected separation between the centre of the star and the centre of mass of the binary system. R_{RL} stands for the radius of a sphere with a volume equal to that of the Roche lobe computed according to the formula of Eggleton (1983). All error bars indicate 1σ uncertainties. The "(f)" symbol in the orbital solution derived by Burkholder et al. (1997) correspond to values fixed by these authors to the previous determination of Stickland (1995).

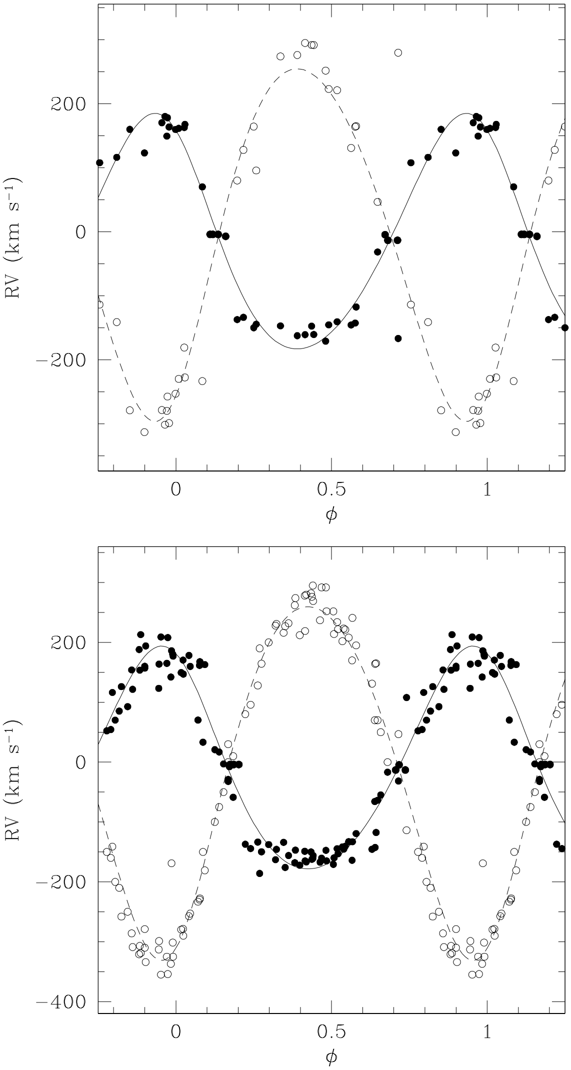

Figure 3.12: Radial velocities of the components of the inner binary of HD 206267. The upper panel shows the RVs corresponding to the measurements taken for this study, assuming a period of 3.710534 days, while the lower panel displays both our measurements with those taken by Stickland (1995) and Burkholder et al. (1997), assuming a period of 3.709777 days. The RVs of the primary and secondary stars are shown with the filled and empty circles, respectively. The solid and dashed lines indicate the orbital solution from Table 3.10.

3.5.4 Preparatory analysis

3.5.4.1 Adjustment of the ternary spectra and spectral disentangling

After the determination of the orbital solution, we usually perform the spectral disentangling of the observed spectra (see Sect. 2.1) to recover the individual contributions of the three components of HD 206267. However, as we have seen in Sect. 3.4.4.1, there may be great complications in our disentangling techniques when we apply them to spectra of a triple system with the third almost non-moving component (over the range of our set of observations) whose lines are always partly blended with the lines of the other two components, leading to the apperance of artefacts in the separated spectra (see Fig. 3.7). This is also the case for HD 206267, with, in addition, rather high projected rotational velocities and macroturbulence velocities (see Sect. 3.5.5.1). We thus applied the same method as we have done for HD 17505, recombining synthetic spectra of all three components, shifted by the corresponding RVs, and comparing the obtained ternary spectra directly to the observations.

We then constrained the fundamental properties of each component with the non-LTE model atmosphere code CMFGEN (Sect. 2.2), with a β law to describe the velocity law in the stellar winds, and a super-level approach for the resolution of the equations of statistical equilibrium. The following chemical elements and their ions were included in the calculations: H, He, C, N, O, Ne, Mg, Al, Si, S, Ca, Fe, and Ni. A new photospheric structure was computed from the solution of the equations of statistical equilibrium, and then connected to the same β wind velocity law. We assumed a microturbulent velocity in the atmosphere varying linearly with velocity from 10 $\mathrm{km\,s^{-1}}$ in the photosphere to $0.1 \times \mathrm{v}_\infty$ at the outer boundary. The generated synthetic spectra of the three components were then shifted by their associated RVs, recombined and compared to the observed spectra of HD 206267. We then constrained iteratively the physical properties of each one of the three stars, as we have done in Sect. 3.4.4.1 for HD 17505:

- Starting point from the literature (Martins et al. 2005; Muijres et al. 2012; Prinja et al. 1990), assuming that the fundamental properties of each star were close to typical values of stars of the same spectral types;

- First approximation of the rotational velocities from a multi-Gaussian fitting technique within MIDAS on the lines He I $\lambda\lambda$ 4026 and 4471, and O III λ 5592 for the most deblended spectra and a Fourier transform method (Simón-Díaz & Herrero 2007, Gray 2008) to the obtained Gaussians;

- Estimation of the macroturbulence velocities with the auxiliary program MACTURB of the stellar spectral synthesis program SPECTRUM v2.76 developed by Gray (2010), applying this technique to the wings of He I λ 4026, 4471, 4713 and 5016, and He II λ 4542 for several phases;

- Estimation of the respective contribution of the three components to the spectra of the triple system through the following formula on selected lines:

  $$\frac{l_i}{l_i+l_j+l_k} = \frac{l_i}{l_j\left(\frac{l_i}{l_j}+1+\frac{l_k}{l_j}\right)}$$

  with

  $$\frac{l_i}{l_j} = \left(\frac{EW_i}{EW_j}\right)_{\rm obs}\left(\frac{EW_{STj}}{EW_{STi}}\right)_{\rm mean}$$

  where i, j and k are representing either the primary, secondary or tertiary stars, depending on the contribution we were calculating. The EW_i represent the equivalent widths of the studied lines of the i star referring to the combined continuum of the three stars and EW_{STi} indicates the same measurement in a synthetic spectrum of a typical star of the same spectral type as the i star, computed with CMFGEN. We considered the spectral types previously determined by Burkholder et al. (1997; O 6.5 V((f)) + O 9.5: V) for the inner binary system, and the one determined by Harvin et al. (2003; O 8 V) for the third component. This way, we obtained that the primary, secondary and tertiary contributions to the total flux are 60%, 15% and 25%, respectively.

- First determination of the effective temperature in the models, through the relative strengths of He I λ 4471 and He II λ 4542 lines (Martins 2011);

- First approximation of the surface gravities through the width of the Balmer lines, which were approximatively reconstructed with a multi-Gaussian fit on a number of observations at different phases;

- Estimation of the terminal velocities, the β of the velocity law, and the mass-loss rates, through the strength of Hα, the width of He II λ 4686 and Hα, and the strengths of Hγ and Hδ, respectively, and estimation of the clumping factors, and the clumping velocity factors, based on the shape of Hα and Hβ lines. Note that these estimates of the terminal velocities of the primary and secondary stars can only be considered as lower limits, while the estimates of the other wind parameters of the same stars can only be considered as upper limits. This is due to the possible existence of a wind-wind interaction zone, which may lead to an excess emission in the Balmer lines, and thus to an underestimate of the terminal velocities, and an overestimate of the β of the velocity law, the clumping factors, the clumping velocity factors, and the mass-loss rates of the primary and secondary stars. The third object should be free from such a pollution, since it is too distant from the inner binary to induce such wind-wind interactions;
- Adjustment of the CNO abundances through the strengths of associated lines, with a normalized χ^2 analysis to determine the best fit to selected lines, as done by Martins et al. (2015; see also Raucq et al. 2016; 2017) and explained in Sect. 2.2.2. We used the C III $\lambda\lambda$ 4068-70; N II λ 4379, N III $\lambda\lambda$ 4511, 4515, and 4525; O III $\lambda\lambda$ 5508 and 5592 lines to adjust the C, N and O abundances, respectively, for the primary star, and the C III $\lambda\lambda$ 4163 and 4187 and N III $\lambda\lambda$ 4530 and 4535 lines in addition to the previous lines for the secondary star.

In Fig. 3.13 we show parts of the observed spectra at different phases with the corresponding recombined synthetic spectra of the triple system.

Once we obtained a good fit of the triple system for all of the observations, we substracted the synthetic tertiary spectrum from each observation, to recover the spectra of the inner binary system. We were then able to treat the obtained binary spectra with the disentangling code, as we did for the other binary systems, HD 149404 (see Sect. 3.1 of Raucq et al. 2016) and LSS 3074 (see Sect. 6.1 of Raucq et al. 2017).

3.5.4.2 Spectral types

Based on the reconstructed individual primary and secondary spectra, we then determined the respective spectral types of the components of the inner binary of HD 206267. To do so, we applied Conti's quantitative classification criterion for O-type stars (Conti & Alschuler 1971, Conti & Frost 1977, see also van der Hucht 1996) for the spectral types, based

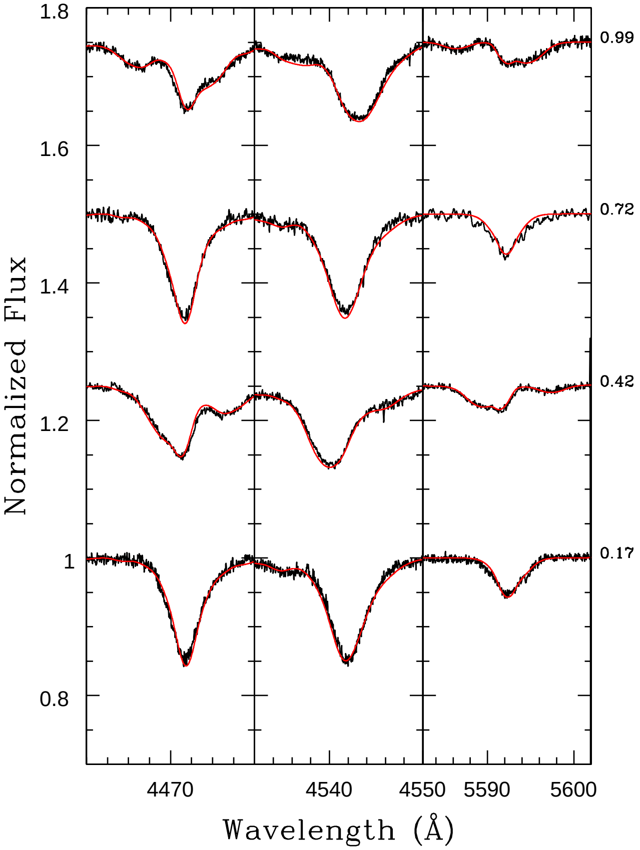

Figure 3.13: He I λ 4471 (left panel), He II λ 4542 (middle panel) and O III λ 5592 lines (right panel) of the recombined synthetic spectrum (red) of the triple system HD 206267 for different observations (black). The phases of the different observations, according to the ephemerides of Table 3.10, are presented on the left side of the figure.

on the equivalent width ratio of the spectral lines He I λ4471 and He II λ4542, and found that the primary is an O5.5 star and the secondary an O9.5 star. We then used Conti's quantitative criterion for the luminosity classes, based on the equivalent width ratio of the spectral lines Si IV λ4088 and He I λ4143, and obtained that the secondary is a V star. However, since this criterion is designed for stars from O7 to O9.5, we could not use it to determine the luminosity class of the primary star.

We thus used the Walborn criterion (Walborn & Fitzpatrick 1990 and references therein) to determine that the primary is a V star, since its spectrum displays a strong He II $\lambda\,4686$ absorption. In addition to the strong absorption of He II $\lambda\,4686$, the spectrum of the primary star also displays N III $\lambda\lambda\,4634$-40-42 emission, leading to the addition of a ((f)) qualifier to its spectral types. We thus found that the primary is an O5.5V((f)) star and the secondary an O9.5V star. We can see that our determination of the spectral type of the secondary is exactly the same as determined by Burkholder et al. (1997), but we obtain a slightly earlier spectral type for the primary component: O5.5 vs. O6.5 in the study of these authors. Since our spectral classification of the primary and secondary stars of HD 206267 is based on the reconstructed spectra after removal of the "polluting" third component, it should be less sensitive to a possible phase-dependence of some specific spectral features, and should thus be more robust than a classification based only on spectra of the triple system taken near the quadrature phases of the inner binary system.

3.5.4.3 Brightness ratio

As we have seen in Sect. 2.1, the spectral disentangling yields the strength of the lines in both primary and secondary spectra compared to the combined continuum, but it does not permit to establish the relative strengths of the individual continua. We therefore need to establish the brightness ratio of the stars in an independant way in order to further analyse the reconstructed spectra of the primary and secondary components of HD 206267.

To do so, we used a similar technique as done in Sect. 3.5.4.1 with multi-Gaussian fits of selected lines to estimate the contribution of the three components of the triple system to the observations. Here, we directly measured the equivalent widths of a number of selected spectral lines on the separated spectra of the primary and secondary stars, but referring to the combined continuum of the two stars, and calculated the brightness ratio of the two stars with the following formula:

$$\frac{l_1}{l_2} = \left(\frac{EW_1}{EW_2}\right)_{\mathrm{obs}} \left(\frac{EW_{ST2}}{EW_{ST1}}\right)_{\mathrm{mean}}$$

with the same conventions as in the previous section. The results of our measurements are listed in Table 3.11.

This way, we derived a mean primary over secondary brightness ratio of 4.75 ± 1.79. This value is coherent, within the error bars, with what we inferred from our preliminary study of the contributions of the different

Table 3.11: Determination of the brightness ratio of the inner binary system of HD 206267 from the dilution of prominent lines.

Line	Equivalent Width (Å)				l_1/l_2
	Observations		Synthetic spectra		
	Primary	Secondary	O5.5	O9.5	
He I λ 4026	0.27	0.09	0.74	1.02	4.22
He II λ 4200	0.32	0.02	0.76	0.16	4.18
Hγ	1.27	0.19	2.11	2.52	8.16
He I λ 4471	0.18	0.11	0.41	1.04	4.29
He II λ 4542	0.48	0.02	0.92	0.13	2.87

components to the observed spectra of the triple system, based on the multi-Gaussian fit, i.e. $l_1/l_2 = 60/15 = 4.00$.

The mean V magnitude of the system is found in the VizieR Online Data Catalog (2002) as being 5.738 ± 0.033, and the $(B-V)$ color is 0.210 ± 0.010. The intrinsic $(B-V)_0$ of O5.5V stars is -0.28 and that of O9.5V stars -0.26, with a mean value of -0.27 for the system (Martins & Plez 2006). We determined an extinction A_V of 1.457 ± 0.031, assuming $R_V = 3.1$. Assuming a distance modulus of 9.9 ± 0.5 (Burkholder et al. 1997), we inferred an absolute magnitude $M_V = -5.619 \pm 0.502$ for the system. With the previously determined brightness ratio, we then calculated individual absolute magnitudes of $M_V^P = -5.412 \pm 0.605$ and $M_V^S = -3.720 \pm 0.605$.

The reconstructed normalized primary and secondary optical spectra are shown and discussed in Sect. 3.5.5.2.

3.5.5 Spectral analysis

3.5.5.1 Rotational velocities and macroturbulence

The reconstructed individual spectra of the primary and secondary stars of HD 206267 also permitted us to refine the values of the projected rotational velocities and macroturbulence of both stars. We used the same Fourier transform analysis (Simón-Díaz & Herrero 2007) as in Sect. 3.4.4.1, applied on the profiles of isolated lines in the disentangled spectra. The elimination of the third component and the reconstruction of the individual spectra permitted us to use more lines at this stage than what was possible with the multi-Gaussian fit. We determined the projected rotational velocities $v \sin i$ of the primary star based on the He I $\lambda\lambda$ 4026, 4471, 4922 and 5016, He II $\lambda\lambda$ 4200 and 4542, and O III λ 5592 lines, and

Table 3.12: Projected rotational velocities ($v \sin i$ in $\mathrm{km\,s^{-1}}$) of the primary and secondary components of HD 206267.

Line	Primary	Secondary
He I λ 4026	170	104
He II λ 4200	133	110
He II λ 4471	175	96
He II λ 4542	125	113
He I λ 4922	166	99
He I λ 5016	195	96
O III λ 5592	171	-
Mean value	162.1 ± 22.8	103.0 ± 6.6

that of the secondary star based on the same lines except the O III λ 5592 line.

The results are presented in Table 3.12. The mean $v \sin i$ of the primary star is (162.1 ± 22.8) $\mathrm{km\,s^{-1}}$, and that of the secondary star is (103.0 ± 6.6) $\mathrm{km\,s^{-1}}$.

Once we have determined the mean projected rotational velocities, we adjusted our determination of the macroturbulence velocities of both primary and secondary stars, with the auxiliary program MACTURB developed by Gray (2010), based on the radial-tangential anisotropic macroturbulent broadening formulation of Gray (2008). We worked on the lines He I $\lambda\lambda$ 4026, 4471, 4713 and 5016, and He II λ 4542 in the individual spectra, after including the rotational velocity broadening, and we obtained macroturbulence velocities of 80 and 120 $\mathrm{km\,s^{-1}}$ for the primary and secondary stars respectively.

Both rotational and macroturbulence broadening effects were applied on the synthetic spectra before comparing the latter with the individual reconstructed spectra of the primary and secondary stars of HD 206267.

3.5.5.2 Fit of the separated spectra with the CMFGEN code

Once we obtained the reconstructed spectra of the primary and secondary stars of HD 206267, and determined their brightness ratio, rotational velocities and macroturbulence velocities, we improved our determination of the fundamental parameters of both stars with the CMFGEN code. We followed the same procedure as in Sect. 3.5.4.1 to constrain the different stellar properties.

As mentionned in Sect. 2.1.2, however, the Balmer lines are too broad to be perfectly recovered by the disentangling procedure, and their wings may thus not be entirely reliable to adjust de surface gravities. To circumvent this problem, we used the following iterative process to constrain the surface gravities together with the stellar luminosities. Based on our first estimate of the $\log g$ with the fit of the triple system (see Sect. 3.5.4.1) and our determination of the effective temperatures of the stars, we inferred the associated bolometric corrections (Lanz & Hubeny 2003) and the individual bolometric luminosities, using the absolute V magnitudes of the components derived in Sect. 3.5.4.3. From these bolometric luminosities and the effective temperatures, we computed the ratio of the stellar radii $\frac{R_P}{R_S}$, which, together with the assumed surface gravities, yielded the spectroscopic mass ratio $\frac{M_P}{M_S}$. By comparing this spectroscopic mass ratio with the dynamical one inferred from the orbital solution we obtained a new estimate of the surface gravities. We repeated this iterative process until the spectroscopic and dynamical mass ratios agreed with each other, and the CMFGEN synthetic spectra produced for the new surface gravities of both stars matched the reconstructed individual spectra as well as possible.

Figure 3.14 displays the best fit of the optical spectra of the primary and secondary stars of HD 206267 obtained with CMFGEN. The corresponding stellar parameters are listed in Table 3.13, and Table 3.14 compares the chemical abundances of these best-fit models with the solar abundances taken from Asplund et al. (2009).

Table 3.13: Best-fit CMFGEN model parameters of the primary and secondary stars of HD 206267.

	Prim.	Sec.
R ($R_\odot$)	11.2 ± 1.8	5.8 ± 1.0
M ($M_\odot$)	27.7 ± 12.3	17.6 ± 5.9
$T_{\rm eff}$ (10^4 K)	4.10 ± 0.15	3.55 ± 0.15
$\log (\frac{L}{L_\odot})$	5.54 ± 0.12	4.70 ± 0.12
$\log g$ (cgs)	3.75 ± 0.15	4.14 ± 0.15
β	≤ 0.85	≤ 0.50
v_∞ (km s^{-1})	≥ 2300	≥ 3500
$\dot{M}/\sqrt{f_1}$ ($M_\odot$ yr^{-1})	$\leq 8.98 \times 10^{-8}$	$\leq 9.16 \times 10^{-7}$
f_1	≤ 0.2	≤ 0.3
f_2 (km s^{-1})	≤ 100	≤ 300
BC	-3.68	-3.28

f_1 and f_2 represent the clumping filling factor and the clumping velocity factor, presented in Sect. 2.2.2. The quoted errors correspond to 1σ uncertainties. The bolometric corrections are taken from Lanz & Hubeny (2003), based on our best-fit $T_{\rm eff}$ and $\log g$.

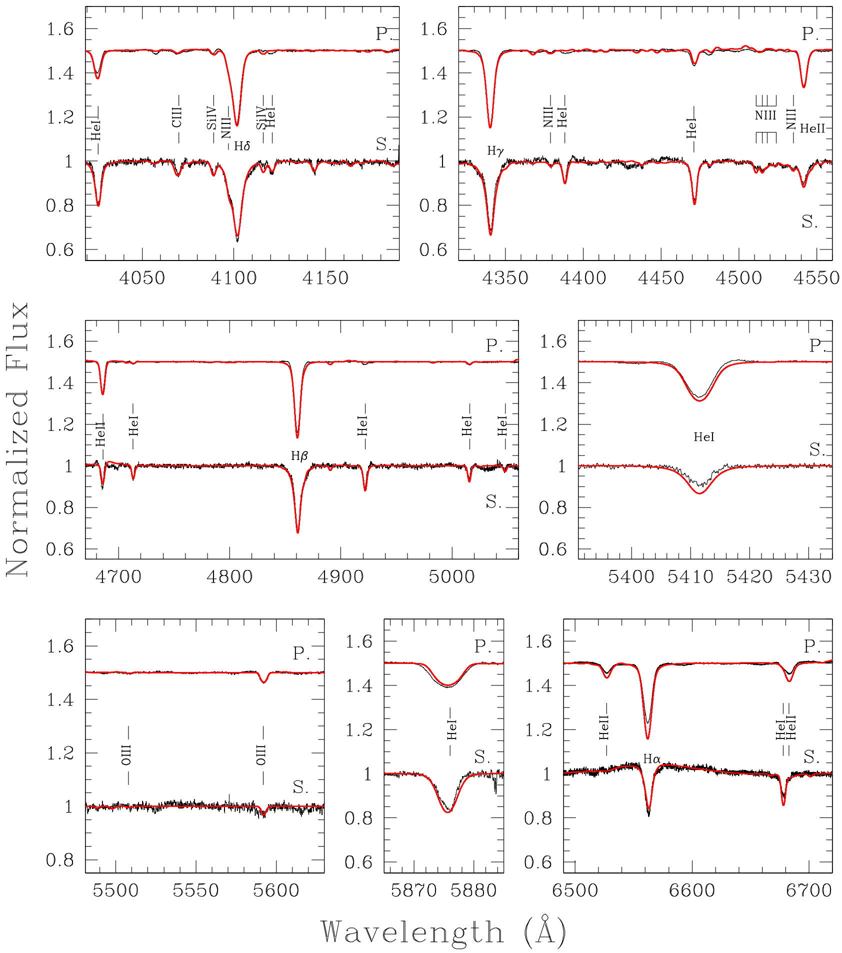

Figure 3.14: Part of the normalized disentangled spectra of the primary (top, shifted by 0.5 continuum units) and secondary (bottom) stars of HD 206267, along with the best-fit CMFGEN model spectra (red).

Figure 3.14 shows that the Balmer, He, C, N and O lines are well reproduced by the models for both stars.

By coupling the stellar masses obtained with CMFGEN (Table 3.13) with the minimum masses obtained with the combined orbital solution (Table 3.10), we then obtained an inclination of the system $i \sim 76.7°$. This inclination then permitted us, together with the stellar radii determined

Table 3.14: Chemical surface abundances of the primary and secondary stars of HD 206267.

	Primary	Secondary	Sun
He/H	0.1	0.1	0.089
C/H	$1.21^{+0.06}_{-0.06} \times 10^{-4}$	$1.53^{+0.17}_{-0.18} \times 10^{-4}$	2.69×10^{-4}
N/H	$4.15^{+0.32}_{-0.30} \times 10^{-4}$	$2.32^{+0.75}_{-0.82} \times 10^{-4}$	6.76×10^{-5}
O/H	$4.52^{+0.80}_{-0.57} \times 10^{-4}$	$2.00^{+0.64}_{-0.49} \times 10^{-4}$	4.90×10^{-4}

Abundances are given by number as obtained with CMFGEN. The solar abundances (Asplund et al. 2009) are quoted in the last column. The 1σ uncertainty on the abundances was set to abundances corresponding to a normalized χ^2 of 2.0 (see Sect. 2.2.2 of this work, Sect. 4.3 of Raucq et al. 2016 and Sect. 8.3 of Raucq et al. 2017; see also Martins et al. 2015). The values of the He abundances have been fixed in the models.

with CMFGEN (Table 3.13) and the radii of the Roche lobes obtained in the orbital solution (Table 3.10), to estimate the mean Roche lobe filling factors of both stars, and we obtained 0.74 ± 0.27 and 0.48 ± 0.17 respectively for the primary and secondary stars of HD 206267. Given the eccentricity of 0.1306 of the orbit of HD 206267, these Roche lobe filling factors become 0.85 ± 0.29 and 0.55 ± 0.19 respectively for the primary and secondary stars at the periastron. We can see that, whilst the secondary star is well inside its Roche lobe, the primary star, within the rather large error bars, may either be well within its Roche lobe or fill it. A second interesting result is that we found a slight enhancement of N and a slight depletion of C and O at the surface of both primary and secondary stars. We discuss this abundance pattern in Sect. 3.5.6.1. Finally, from the inclination determined earlier, we derived the absolute rotational velocities and obtained 166.6 and 105.8 km s^{-1} for the primary and secondary stars respectively. By combining these rotational velocities with the stellar radii obtained with CMFGEN (Table 3.13), we the found that the rotational period of the primary and secondary stars of HD 206267 are 3.40 and 2.77 days. We can see that the primary star is likely in synchronous rotation with the orbital period of the system, which is 3.709777 days, whilst the secondary star appears to rotate at a slightly higher rate. However, if we calculate the critical velocities of the stars, $v_{\text{crit}} = \left(\frac{2GM}{3R_P}\right)^{1/2}$, based on our results from the CMFGEN fit, we find that the current rotational velocities of the primary and secondary stars correspond to $0.24 \times v_{\text{crit}}$ and $0.14 \times v_{\text{crit}}$ respectively, which is very close to the median value of birth rotational velocities for stars of similar masses, according to the study of Wolff et al. (2006). We will come back to these results in Sect. 3.5.6.1.

3.5.6 Discussion and conclusion

3.5.6.1 Evolutionary status

We have shown in the previous section that the spectra of the primary and secondary components of HD 206267 show the signatures of a slight modification of the CNO surface abundances. In Fig. 3.15, we compare our inferred N/C and N/O ratios with the predictions from the Geneva evolutionary models of single massive stars (Ekström et al. 2012). In the left panel, we show the case of non-rotating stars, whilst the right panel shows the case of stars rotating at $0.4 \times v_{crit}$. We can note on this figure that the observed abundances of both stars are difficult to explain in the non-rotating case, but are close to what is predicted by single star evolutionary models for stars of initial masses close to 20-25 and 30 $M_{\odot}$, for the primary and secondary stars respectively, which is close to the masses we inferred from our spectroscopic analysis of the system (Table 3.13).

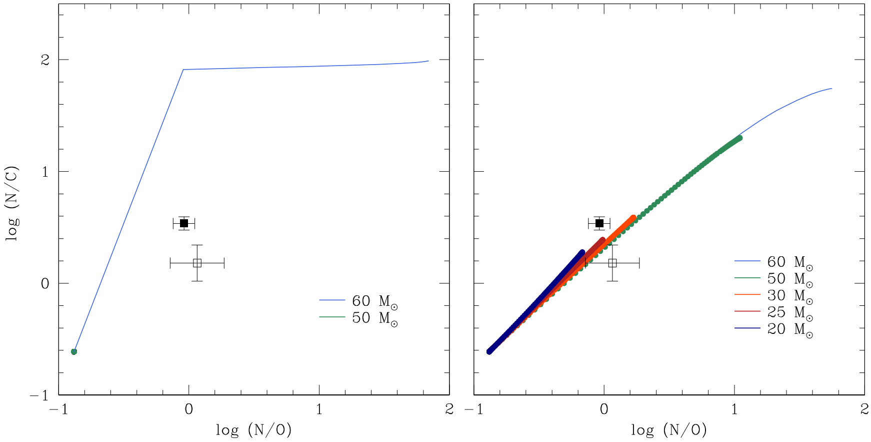

Figure 3.15: Comparison of the N/C and N/O ratios obtained from our spectral analysis with predictions from single star evolutionary models of different masses (Ekström et al. 2012). The filled (resp. empty) squares display the characteristics of the primary (resp. secondary) star. The left panel illustrates the results for core hydrogen burning phase tracks without stellar rotation, and the right panel corresponds to the same tracks for stars with a rotation of $0.4 \times v_{crit}$.

In Figure 3.16, we show the positions of the primary and secondary stars in the Hertzsprung-Russell diagram (HRD; upper panels) and in the

$\log g$-$\log T_{\text{eff}}$ diagram (lower panels), with the evolutionary tracks from Ekström et al. (2012) for the core-hydrogen burning phase of single stars at solar metallicity. The left panels display the non-rotating stars case and the right panels show the tracks for stars rotating at $0.4 \times v_{crit}$.

If we consider the case without any rotational mixing, we see that the position of the secondary star in the HRD and in the $\log g$-$\log T_{\text{eff}}$ diagram is close to the tracks corresponding to stars with initial masses of $20\,M_{\odot}$, which is close to its current spectroscopic mass of 17.6 $M_{\odot}$. However, the position of the primary star in the HRD suggests an initial mass close to $40\,M_{\odot}$, and its position in the $\log g$-$\log T_{\text{eff}}$ diagram is in favour of an initial mass of $60\,M_{\odot}$, while its spectroscopic mass is a factor two to three times smaller. Moreover, both stars do not seem to be located on the same isochrone in either of the diagrams.

Considering the case of single stars rotating at $0.4 \times v_{crit}$, we see in the figure that both stars may be located on the 3.2 million years isochrone and that the postion of the secondary star is once again close to the 20-25 tracks in both HRD and $\log g$-$\log T_{\text{eff}}$ diagram. However, the position of the primary star in both diagrams suggests an initial mass of $40\,M_{\odot}$, which is a factor two larger than the observed mass.

Considering the slightly higher rotation rate of the secondary star of HD 206267 found in Sect. 3.5.5.2 and our analysis of Figure 3.16, the system may have encountered some kind of binary interactions during its evolution and its current status is thus hardly explainable by single star evolutionary models. However, the abundance patterns can be explained by these single star models, which suggests that the system probably did not go through a full RLOF process, which should have affected the surface abundances of the donor star in a much stronger way (see the cases of HD 149404 and LSS 3074) and should also have led to orbital circularization, which is currently not the case. One way to explain the current status of HD 206267 would be an intermittent RLOF process around periastron, where case A mass transfer occurs temporarily, and is then interrupted until the next periastron passage. At this stage, we stress however that our spectra of the system do not reveal any obvious signature of such an interaction, such Hα emission, that would appear at phases near periastron. Therefore, if such intermittent RLOF has taken place, it should have ceased now.

One possible reason for such an interruption could be the dynamical influence of the third component in a hierarchical triple system. Indeed, the presence of a third component in the system can produce the appearance of Lidov-Kozai cycles, for example (Toonen et al. 2016, and references therein). In such cases, angular momentum exchange between the inner and outer orbits can occur, due to a mutual torque between these orbits. Since the orbital energy, and therefore the semi-major axes, are conserved, the orbital eccentricity of the inner binary system and the mutual inclination between the two orbits can vary periodically. This Lidov-Kozai mechanism could therefore lead to a periodic modulation of the binary interaction at periastron passage. Given the angular separation of 0.1 arcsec at an assumed distance of 950 pc, we find a separation of at least 95 AU between the inner binary system and the third component. The orbital period of the third component would thus be at least 115 years. Since the timescale of the Lidov-Kozai cycle scales with the square of the ratio between the outer and inner orbital periods (Toonen et al. 2016), we estimate a minimum timescale of the order 1.3 Myr. Although this timescale is quite long, it might be sufficiently short to modulate a slow episodic (i.e. occurring only around periastron) case-A mass transfer. HD206267 appears thus as an interesting candidate of such triple-system evolution.

In future studies, it would be highly interesting to collect photometric data of this system. Indeed, with a period of 3.7 days and an estimated inclination of 77°, it appears likely that the system displays at least ellipsoidal variations that might help to further constrain its parameters.

3.5.6.2 Summary and conclusion

We have studied the fundamental properties of the inner binary system of HD 206267. The first step has been to fit the triple system spectra with a combination of synthetic CMFGEN spectra of the three components shifted by their associated RVs for each observation, then to substract the third component from the observed spectra and recover the spectra of the inner binary. We then used our disentangling code to recover the individual spectra of the primary and secondary stars. Once we obtained these reconstructed spectra, we determined the fundamental properties of the primary and secondary components with the CMFGEN code and used them to constrain the evolutionary status of the system.

We established the existence of a slight overabundance in N and slight C and O depletions in both primary and secondary atmospheres, that may be explained by single star evolutionary models. We found that the primary star is in synchronous rotation with the orbital period, but the secondary star displays a slightly higher rotation rate. We also found that the single star evolutionary models cannot explain the position of the primary star in the HRD and $\log g$-$\log T_{\mathrm{eff}}$ diagram. We concluded that the system may have experienced binary interactions in the past, but may not have experienced a complete RLOF episode at this stage of its evolution.

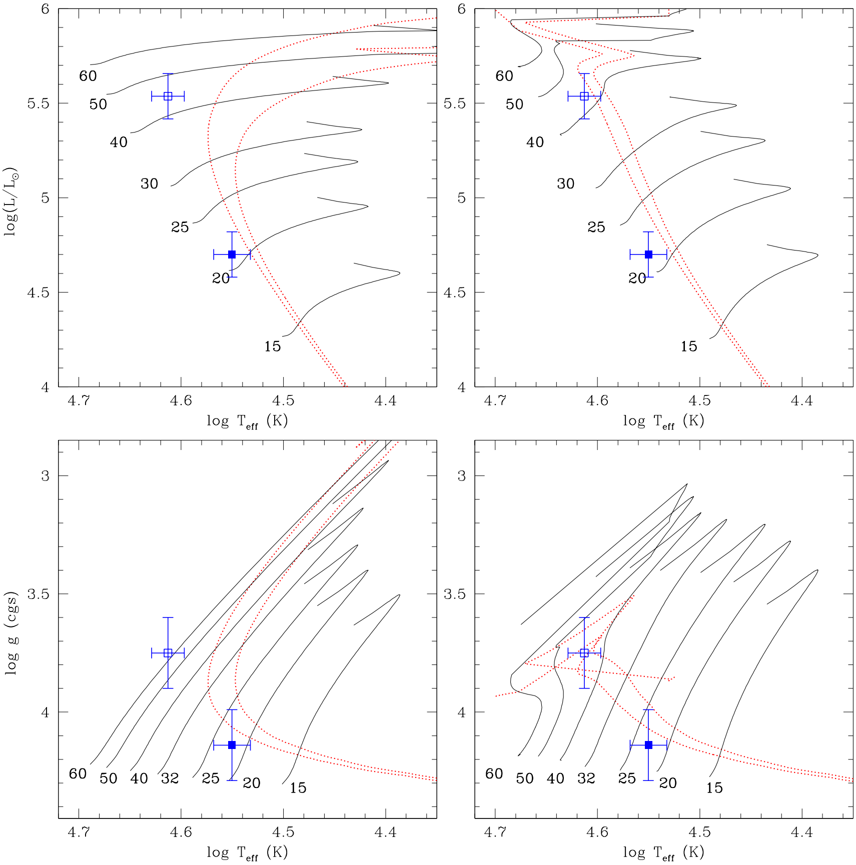

Figure 3.16: The upper panels show the positions of the primary (empty square) and secondary (filled square) stars of HD 206267 in the Hertzsprung-Russell diagram, while the lower panels show their positions in the log g-log $T_{\rm eff}$ diagram, along with evolutionary tracks for single massive stars at solar metallicity during the core-hydrogen burning phase (Ekström et al. 2012). In the left panels, the evolutionary tracks correspond to non-rotating stars, whilst the right panels yield the results for stars rotating at $0.4 \times v_{crit}$. The dotted red lines correspond to isochrones of 3.2 and 4.0 million years.

Chapter 4

Conclusions

4.1 Our sample of binary systems

In this thesis, we have studied the fundamental properties of four short-period massive binary systems, in order to confirm or to search for the presence of clues of past-RLOF episodes in their previous evolution. We have mainly worked on high quality optical spectra of the systems, and also investigated a sample of IUE spectra for the first system, HD 149404. For the second system, LSS 3074, we also investigated photometric data. For LSS 3074, HD 17505 and HD 206267, we determined new orbital solutions for the systems. We have used a disentangling procedure to separate the contributions of each component to the observed spectra of the systems, to be able to investigate independently the fundamental properties of these components as if they were single stars. This way, we have investigated the spectral types of each star and the brightness ratio for each binary system. We then used the non-LTE model atmosphere code CMFGEN to study the fundamental properties of each star. For each system, we discussed the evolutionary status of the components compared to single star evolutionary models. The results concerning HD 149404 and LSS 3074 are presented in Raucq et al. (2016) and Raucq et al. (2017), respectively. A summary of our main results for each object is presented here below.

4.1.1 HD 149404

This system is a detached, non-eclipsing O7.5I(f) + ON9.7I system, with a circular orbit and an orbital period of 9.81 days. We worked on five FEROS spectra, 12 Coralie spectra and 25 *IUE* spectra.

We have quantified the strong overbundance in nitrogen in the secondary atmosphere, together with a C and O depletion. We also found a slight N overabundance in the primary atmosphere. These abundance patterns cannot be explained by single star evolutionary models, but are close to what can be found in the literature for post-case B RLOF systems: $[N/C] = 100\ [N/C]_{\odot}$ and $[N/O] \geq 5\ [N/O]_{\odot}$ (Vanbeveren 1982) for the donor star, and $[N/C] \sim 2 - 3\ [N/C]_{\odot}$ for the gainer star (Vanbeveren & de Loore 1994). However, there are still some caveats since, given its present status as an O+O binary, HD 149 404 is more likely to have undergone a case A RLOF episode. A second important result is that we found evidence for asynchronous rotation, with a rotational period ratio of 0.5 ± 0.11. We have also shown that, given their spectroscopic masses, single star evolutionary models cannot account for the fundamental properties of both components of the system. Moreover, in our analysis, the two components of HD 149404 were not located on the same isochrone in the Hertzsprung-Russel and $\log g$-$\log T_{\rm eff}$ diagrams, although they would be expected to have the same age.

The hypothesis of past RLOF interaction in this system, with a mass and kinetic momentum transfer from the current secondary to the current primary star, is most plausible to explain its chemical abundances and rotational asynchronicity, and the impossibility to explain the current fundamental properties of both components with single star evolutionary models.

4.1.2 LSS 3074

LSS 3074 is a circular short-period O5.5If + O6.5-7If binary system, with an orbital period of 2.1852 days. We studied three EMMI spectra and twelve FEROS spectra. We also worked on photometric data taken with the Yale 1 m telescope at the CTIO.

From these photometric lightcurves, we found that the system is in an overcontact configuration, with a filling factor of 1.008 for both stars and an orbital inclination of 54.5°. Based on our spectroscopic analysis, we confirmed the very low masses and radii found in previous studies, which is unusual for stars with such spectral types. In addition, we found a strong overabundance in N and a strong depletion in C and O in both primary and secondary stars, and a strong He enrichment in the primary atmosphere. We have shown that these abundance patterns cannot be explained by single star evolutionary models, neither can be the fundamental properties of both components. Moreover, we found an apparent age discrepancy between the primary and secondary stars of LSS 3074.

However, there are still some caveats in the analysis of the lightcurves, since the hottest star appears to be in front during the deepest minimum and there is a discrepancy between the spectroscopic and the photometric brightness ratios. We suggested that some of the discrepancies between the spectroscopic and photometric properties of the system may come from a strong radiation pressure of the primary.

We proposed several evolutionary pathways through a RLOF process to explain both the low masses and the chemical abundances of both components of LSS 3074, and concluded that the system has been, and may still be, significantly affected by binary interaction, and that both stars have probably lost a significant fraction of their mass to the surroundings.

4.1.3 HD 17505

HD 17505 is a multiple system composed of at least seven visual companions, with an O-star central triple system, composed of an eccentric O7V((f)) + O7V((f)) inner binary system, with an orbital period of 8.5690 days, and a more distant O6.5III star ($P_{\rm orb} < 61$ years). We studied a sample of fifteen HEROS spectra, one ELODIE spectrum and six FIES spectra. We modelled the spectra of the triple system for all of the observations and substracted the synthetic spectrum of the third component from each observation to recover the spectra of the inner binary and study independently the primary and secondary components through our disentangling procedure.

We established the existence of a slight N overabundance and a slight C and O depletion in both stars, and showed that these properties and the fundamental properties of both stars can be explained by single star evolutionary models with the inclusion of rotational velocity.

We thus suggested that the inner binary system of HD 17505 has not experienced binary interactions at this stage of its evolution.

4.1.4 HD 206267

HD 206267 is a triple system composed of an eccentric O5.5V((f)) + O9.5V inner binary system, with an orbital period of 3.709777 days, and a more distant, third O component with a constant velocity. We studied a sample of twenty-two HEROS spectra, one ELODIE spectrum, one ESPaDOnS spectrum, nine SOPHIE spectra and five FIES spectra. We recombined synthetic spectra of the three components to model all the observed spectra of the triple system and substracted the synthetic spectrum of the third component from each observation to recover the spectra of the inner binary system. We then used our disentangling procedure to reconstruct the primary and secondary spectra and to study the fundamental properties of these two stars independently.

We established the existence of a slight overabundance in N and a slight depletion in C and O in both primary and secondary atmospheres, and showed that some of the properties of both stars cannot be explained by single star evolutionary models.

We suggested that the system did not experienced a complete RLOF episode at this stage of its evolution, but could have undergone an episode of intermittent mass-transfer around its periastron.

4.2 Future perspectives

From an observational point of view, this thesis work was based on a large number of high-quality data. It allowed us to better understand the interaction phenomena taking place in the considered systems, such as the RLOF process, and to get insight into their evolutionary status. However, the studied systems were very complex, and there are still some caveats in our analysis:

- In the case of LSS 3074, we have found discrepancies between the spectroscopic and photometric studies, that may need additional data to understand their possible origins. Very high S/N spectra would be needed to better resolve the rather faint secondary star. An additional study dedicated to the detailed modelling of the light-curve of LSS 3074, including the effect of radiation pressure, would also shed some light on the observed discrepancies. Such studies may also bring some explanation to the simultaneous presence of N III, N IV and N V lines in the primary spectra.

- The cases of the triple systems HD 17505 and HD 206267 have also highlighted the limitations of our disentangling procedure. An interesting perpective of future work would be to improve our procedure to avoid the appearance of artefacts in the reconstructed spectra of the third component of a triple system, which would permit us to study more deeply this third component along with the primary and secondary stars of a triple system.

From a theoretical point of view, we have seen, throughout this study, that some of the selected objects display strong hints of binary interactions, and that their fundamental properties cannot be explained by single star evolutionary models, and the predictions for binary evolutionary models are often lacking or do not apply to the specific cases of post-RLOF O-type binaries. Indeed, we have seen for the case of HD 149404, for example, that the determined chemical abundances correspond to a post-case B RLOF system while the current spectral types of both components would suggest that they would have gone through a case A RLOF episode. We have also shown that, whilst the abundance pattern of the components of HD 206267 can be explained by single star evolutionary models, we found some discrepancies between some of the fundamental properties of the components of this system and the predictions from the models. This system has an eccentric orbit and binary interaction might just be starting and be limited to a short phase interval around pariastron passage. For such systems, a dedicated theoretical study would be needed to understand the details of their evolution. It is also of the outmost importance to continue such studies of massive close binary systems to search for similar systems and enlarge our sample. This way, we may be able to improve the constraints on binary evolutionary models, and improve our understanding of the interaction processes taking place in massive close binaries in general.

Bibliography

Adams, F. C., Ruden, S. P., & Shu, F. H. 1989, ApJ, 347, 959

Alecian, E., Neiner, C., Wade, G. A., et al. 2015, in IAU Symposium, Vol. 307, New Windows on Massive Stars, ed. G. Meynet, C. Georgy, J. Groh, & P. Stee, 330–335

Alecian, E., Wade, G. A., Catala, C., et al. 2013, MNRAS, 429, 1001

Anderson, L. S. 1989, ApJ, 339, 558

Antokhina, E. A., Srinivasa Rao, M., & Parthasarathy, M. 2011, New Astronomy, 16, 177

Asplund, M., Grevesse, N., Sauval, A. J., & Scott, P. 2009, ARA&A, 47, 481

Bagnuolo, Jr., W. G., Gies, D. R., Hahula, M. E., Wiemker, R., & Wiggs, M. S. 1994, ApJ, 423, 446

Bethe, H. A. 1939, Phys. Rev., 55, 434

Bethe, H. A., & Critchfield, C. L. 1938, Phys. Rev., 54, 248

Bodenheimer, P. 1995, ARA&A, 33, 199

Bonnell, I. A. 2001, in IAU Symposium, Vol. 200, The Formation of Binary Stars, ed. H. Zinnecker & R. Mathieu, 23

Bonnell, I. A., Bate, M. R., & Zinnecker, H. 1998, MNRAS, 298, 93

Bonnell, I. A., Smith, R. J., Clark, P. C., & Bate, M. R. 2011, MNRAS, 410, 2339

Bonnell, I. A., & Bate, M. R. 1994, MNRAS, 271, 999

Bonnell, I. A., & Bate, M. R. 2005, MNRAS, 362, 915

Bonnell, I. A., & Smith, R. J. 2011, in IAU Symposium, Vol. 270, Computational Star Formation, ed. J. Alves, B. G. Elmegreen, J. M. Girart, & V. Trimble, 57–64

Bouret, J.-C., Lanz, T., & Hillier, D. J. 2005, A&A, 438, 301

Brott, I., de Mink, S. E., Cantiello, M., et al. 2011a, A&A

Brott, I., Evans, C. J., Hunter, I., et al. 2011b, A&A

Burkholder, V., Massey, P., & Morrell, N. 1997, ApJ, 490, 328

Busche, J. R., & Hillier, D. J. 2005, AJ, 129, 454

Caughlan, G. R. 1965, ApJ, 141, 688

Cazorla, C., Nazé, Y., & Rauw, G. 2014, A&A, 561, A92

Chen, Z., Nürnberger, D. E. A., Chini, R., et al. 2013, A&A, 557, A51

Chini, R., Hoffmeister, V. H., & Nürnberger, D. 2011, Bulletin de la Societe Royale des Sciences de Liege, 80, 217

Conti, P. S. 1976, Memoires of the Société Royale des Sciences de Liège, 9, 193

Conti, P. S., & Alschuler, W. R. 1971, ApJ, 170, 325

Conti, P. S., & Frost, S. A. 1977, ApJ, 212, 728

de Mink, S. E., Cantiello, M., Langer, N., et al. 2009, A&A, 497, 243

de Mink, S. E., Langer, N., Izzard, R. G., Sana, H., & de Koter, A. 2013, ApJ, 764, 166

de Mink, S. E., Sana, H., Langer, N., Izzard, R. G., & Schneider, F. R. N. 2014, ApJ, 782, 7

de Wit, W. J., Testi, L., Palla, F., & Zinnecker, H. 2005, A&A, 437, 247

Değirmenci, Ö. L., Sezer, C., Demircan, O., et al. 1999, A&AS, 134, 327

Donati, J.-F., & Landstreet, J. D. 2009, ARA&A, 47, 333

Drechsel, H., Lorenz, R., & Mayer, P. 1989, A&A, 221, 49

Ducati, J. R. 2002, VizieR Online Data Catalog, 2237

Eggleton, P. P. 1983, ApJ, 268, 368

Ekström, S., Georgy, C., Eggenberger, P., et al. 2012, A&A, 537, A146

Ekström, S., Meynet, G., Maeder, A., & Barblan, F. 2008, A&A, 478, 467

Eversberg, T., Lépine, S., & Moffat, A. F. J. 1998, ApJ, 494, 799

Ferrario, L., Melatos, A., & Zrake, J. 2015, SSRv, 191, 77

Ferrario, L., Pringle, J. E., Tout, C. A., & Wickramasinghe, D. T. 2009, MNRAS, 400, L71

Fossati, L., Castro, N., Schöller, M., et al. 2015, A&A, 582, A45

Friend, D. B., & Abbott, D. C. 1986, ApJ, 311, 701

Garmany, C. D., & Stencel, R. E. 1992, A&AS, 94, 211

Georgy, C., Meynet, G., Walder, R., Folini, D., & Maeder, A. 2009, A&A, 502, 611

González, J. F., & Levato, H. 2006, A&A, 448, 283

Gorda, S. Y. 2015, Astronomy Letters, 41, 276

Gray, D. F. 2008, The Observation and Analysis of Stellar Photospheres

Gray, R. O. 2010, MACTURB, http://www.appstate.edu/ grayro/spectrum /spectrum276/node38.html

Haefner, R., Simon, K. P., & Fiedler, A. 1994, Information Bulletin on Variable Stars, 3969

Harries, T. J., Hilditch, R. W., & Hill, G. 1997, MNRAS, 285, 277

Harries, T. J., Hilditch, R. W., & Hill, G. 1998, MNRAS, 295, 386

Harvin, J. A., Gies, D. R., & Penny, L. R. 2003, in Bulletin of the American Astronomical Society, Vol. 35, American Astronomical Society Meeting Abstracts, 1223

Heger, A., & Langer, N. 2000, ApJ, 544, 1016

Herbst, W., & Havlen, R. J. 1977, A&AS, 30, 279

Hillier, D. J., & Miller, D. L. 1998, ApJ, 496, 407

Hillwig, T. C., Gies, D. R., Bagnuolo, Jr., W. G., et al. 2006, ApJ, 639, 1069

Hirschi, R., Meynet, G., & Maeder, A. 2004, A&A, 425, 649

Høg, E., Fabricius, C., Makarov, V. V., et al. 2000, A&A, 355, L27

Huang, W., Gies, D. R., & McSwain, M. V. 2010, ApJ, 722, 605

Jansen, F., Lumb, D., Altieri, B., et al. 2001, A&A, 365, L1

Johnston, K. G., Robitaille, T. P., Beuther, H., et al. 2015, ApJ, 813, L19

Kippenhahn, R., & Weigert, A. 1967, Z. Astrophys., 65, 251

Kruckow, M. U., Tauris, T. M., Langer, N., et al. 2016, A&A, 596, A58

Krumholz, M. R. 2011, ApJ, 743, 110

Kuiper, R., Klahr, H., Beuther, H., & Henning, T. 2011, ApJ, 732, 20

Kumsiashvili, M. I., Kochiashvili, N. T., & Djurasevi, G. 2005, Astrophysics, 48, 44

Langer, N. 1998, A&A, 329, 551

Langer, N. 1999, in Lecture Notes in Physics, Berlin Springer Verlag, Vol. 523, IAU Colloq. 169: Variable and Non-spherical Stellar Winds in Luminous Hot Stars, ed. B. Wolf, O. Stahl, & A. W. Fullerton, 359

Langer, N. 2012, ARA&A, 50, 107

Lanz, T., & Hubeny, I. 2003, ApJS, 146, 417

Le Bouquin, J.-B., Sana, H., Gosset, E., et al. 2017, A&A, 601, A34

Li, Y.-F., & Leung, K.-C. 1985, ApJ, 298, 345

Linder, N., Rauw, G., Martins, F., et al. 2008, A&A, 489, 713

Linder, N., Rauw, G., Sana, H., De Becker, M., & Gosset, E. 2007, A&A, 474, 193

Lorenz, R., Mayer, P., & Drechsel, H. 1994, A&A, 291

Lorenz, R., Mayer, P., & Drechsel, H. 1998, A&A, 332, 909

Maeder, A., & Meynet, G. 2000, ARA&A, 38, 143

Mahy, L., Gosset, E., Sana, H., et al. 2012, A&A, 540, A97

Mahy, L., Martins, F., Machado, C., Donati, J.-F., & Bouret, J.-C. 2011, A&A, 533, A9

Marchant, P., Langer, N., Podsiadlowski, P., Tauris, T. M., & Moriya, T. J. 2016, A&A, 588, A50

Martins, F. 2011, Bulletin de la Societe Royale des Sciences de Liege, 80, 29

Martins, F., Hervé, A., Bouret, J.-C., et al. 2015, A&A, 575, A34

Martins, F., Schaerer, D., & Hillier, D. J. 2005, A&A, 436, 1049

Martins, F., & Plez, B. 2006, A&A, 457, 637

Mason, B. D., Gies, D. R., Hartkopf, W. I., et al. 1998, AJ, 115, 821

Massey, P., Johnson, K. E., & Degioia-Eastwood, K. 1995, ApJ, 454, 151

Mayer, P., Drechsel, H., Harmanec, P., Yang, S., & Šlechta, M. 2013, A&A, 559, A22

Mayer, P., Harmanec, P., Nesslinger, S., et al. 2008, A&A, 481, 183

Mayer, P., Lorenz, R., & Drechsel, H. 2002, A&A, 388, 268

McKee, C. F., & Tan, J. C. 2003, ApJ, 585, 850

Meynet, G., Ekström, S., Georgy, C., Maeder, A., & Hirschi, R. 2008, in IAU Symposium, Vol. 252, The Art of Modeling Stars in the 21st Century, ed. L. Deng & K. L. Chan, 317–327

Morrell, N. I., & Niemela, V. S. 1990, in Astronomical Society of the Pacific Conference Series, Vol. 7, Properties of Hot Luminous Stars, ed. C. D. Garmany, 57–59

Muijres, L. E., Vink, J. S., de Koter, A., Müller, P. E., & Langer, N. 2012, A&A, 537, A37

Nazé, Y., Carrier, F., & Rauw, G. 2002, in Astronomical Society of the Pacific Conference Series, Vol. 260, Interacting Winds from Massive Stars, ed. A. F. J. Moffat & N. St-Louis, 457

Nazé, Y., Neiner, C., Grunhut, J., et al. 2017, MNRAS, 467, 501

Neiner, C., & Alecian, E. 2013, in EAS Publications Series, Vol. 64, EAS Publications Series, ed. K. Pavlovski, A. Tkachenko, & G. Torres, 75–79

Niemela, V. S., Cerruti, M. A., Morrell, N. I., & Luna, H. G. 1992, in IAU Symposium, Vol. 151, Evolutionary Processes in Interacting Binary Stars, ed. Y. Kondo, R. Sistero, & R. S. Polidan, 505

Norberg, P., & Maeder, A. 2000, A&A, 359, 1025

Özdemir, S., Mayer, P., Drechsel, H., Demircan, O., & Ak, H. 2003, A&A, 403, 675

Palate, M., Rauw, G., & Mahy, L. 2013, Central European Astrophysical Bulletin, 37, 311

Penny, L. R., Gies, D. R., Wise, J. H., Stickland, D. J., & Lloyd, C. 2002, ApJ, 575, 1050

Penny, L. R., Ouzts, C., & Gies, D. R. 2008, ApJ, 681, 554

Piskunov, N. E., & Valenti, J. A. 2002, A&A, 385, 1095

Pittard, J. M., & Parkin, E. R. 2010, MNRAS, 403, 1657

Plaskett, J. 1923, Publications of the Dominion Astrophysical Observatory Victoria, 2, 269

Potter, A. T., Tout, C. A., & Eldridge, J. J. 2012, MNRAS, 419, 748

Prinja, R. K., Barlow, M. J., & Howarth, I. D. 1990, ApJ, 361, 607

Puls, J., Kudritzki, R.-P., Herrero, A., et al. 1996, A&A, 305, 171

Qian, S.-B., Yuan, J.-Z., Liu, L., et al. 2007, MNRAS, 380, 1599

Raucq, F., Gosset, E., Rauw, G., et al. 2017, A&A, 601, A133

Raucq, F., Rauw, G., Gosset, E., et al. 2016, A&A, 588, A10

Rauw, G. 2007, DSc Thesis, University of Liège

Rauw, G., Nazé, Y., Carrier, F., et al. 2001, A&A, 368, 212

Rauw, G., & Nazé, Y. 2016, AdSpR, 58, 761

Rosen, A. L., Krumholz, M. R., & Ramirez-Ruiz, E. 2012, ApJ, 748, 97

Sana, H., de Mink, S. E., de Koter, A., et al. 2012, Science, 337, 444

Sana, H., Gosset, E., & Evans, C. J. 2009, MNRAS, 400, 1479

Sana, H., Rauw, G., & Gosset, E. 2001, A&A, 370, 121

Sana, H., Rauw, G., Nazé, Y., Gosset, E., & Vreux, J.-M. 2006, MNRAS, 372, 661

Sana, H., Stevens, I. R., Gosset, E., Rauw, G., & Vreux, J.-M. 2004, MNRAS, 350, 809

Schmitt, J. H. M. M., Schröder, K.-P., Rauw, G., et al. 2014, Astronomische Nachrichten, 335, 787

Schneider, F. R. N., Podsiadlowski, P., Langer, N., Castro, N., & Fossati, L. 2016, MNRAS, 457, 2355

Simón-Díaz, S., Castro, N., Garcia, M., Herrero, A., & Markova, N. 2011a, Bulletin de la Societe Royale des Sciences de Liege

Simón-Díaz, S., Garcia, M., Herrero, A., Maíz Apellániz, J., & Negueruela, I. 2011b, in Stellar Clusters Associations: A RIA Workshop on Gaia

Simón-Díaz, S. & Herrero, A. 2007, A&A, 468, 1063

Simón-Díaz, S., Negueruela, I., Maíz Apellániz, J., et al. 2015, in Highlights of Spanish Astrophysics VIII, ed. A. J. Cenarro, F. Figueras, C. Hernández-Monteagudo, J. Trujillo Bueno, & L. Valdivielso, 576–581

Stevens, I. R., Blondin, J. M., & Pollock, A. M. T. 1992, ApJ, 386, 265

Stickland, D. J. 1995, The Observatory, 115, 180

Stickland, D. J. 1997, The Observatory, 117, 37

Stickland, D. J., Koch, R. H., Pachoulakis, I., & Pfeiffer, R. J. 1994, The Observatory, 114, 107

Stickland, D. J., & Koch, R. H. 1996, The Observatory, 116, 145

Stickland, D. J., & Lloyd, C. 2001, The Observatory, 121, 1

Tamajo, E., Munari, U., Siviero, A., Tomasella, L., & Dallaporta, S. 2012, A&A, 539, A139

Tauris, T. M., & van den Heuvel, E. P. J. 2006, Formation and evolution of compact stellar X-ray sources, ed. W. H. G. Lewin & M. van der Klis, 623–665

Thaller, M. L., Gies, D. R., Fullerton, A. W., Kaper, L., & Wiemker, R. 2001, ApJ, 554, 1070

Toonen, S., Hamers, A., & Portegies Zwart, S. 2016, Computational Astrophysics and Cosmology, 3, 6

Tout, C. A., Wickramasinghe, D. T., Liebert, J., Ferrario, L., & Pringle, J. E. 2008, MNRAS, 387, 897

Underhill, A. B. 1995, ApJS, 100, 433

van der Hucht, K. A. 1996, in Liege International Astrophysical Colloquia, Vol. 33, Liege International Astrophysical Colloquia, ed. J. M. Vreux, A. Detal, D. Fraipont-Caro, E. Gosset, & G. Rauw, 1

van Marle, A. J., Langer, N., & García-Segura, G. 2007, A&A, 469, 941

Vanbeveren, D. 1982, A&A, 105, 260

Vanbeveren, D., De Loore, C., & Van Rensbergen, W. 1998, A&ARv, 9, 63

Vanbeveren, D., & De Loore, C. 1994, A&A, 290, 129

Vink, J. S., de Koter, A., & Lamers, H. J. G. L. M. 2001, A&A, 369, 574

Wade, G. A., Bagnulo, S., Drouin, D., Landstreet, J. D., & Monin, D. 2007, MNRAS, 376, 1145

Walborn, N. R. 1972, AJ, 77, 312

Walborn, N. R. 2002, AJ, 124, 507

Walborn, N. R., & Fitzpatrick, E. L. 1990, PASP, 102, 379

Wellstein, S., Langer, N., & Braun, H. 2001, A&A, 369, 939

Wolff, S. C., Strom, S. E., Dror, D., Lanz, L., & Venn, K. 2006, AJ, 132, 749

Woosley, S. E., & Heger, A. 2006, ApJ, 637, 914

Yaşarsoy, B., & Yakut, K. 2013, AJ, 145, 9

Yoon, S.-C., Langer, N., & Norman, C. 2006, A&A, 460, 199

Yoon, S.-C., & Langer, N. 2005, A&A, 443, 643

Zhao, E., Qian, S., Li, L., et al. 2014, New Astronomy, 26, 112

Zinnecker, H., & Yorke, H. W. 2007, ARA&A, 45, 481